Delft University of Technology
Faculty of Civil Engineering and Geosciences

Investigation on the Effect of Subcooling and Temperature on the Kinetics of CO_2 Hydrates Formation and Dissociation in Porous Media

Georgios Ntentopoulos

To obtain the degree of Master of Science in
Applied Earth Sciences

Supervisors:	Dr. Rouhi Farajzadeh	TU Delft and Shell, Supervisor
	Dr. Denis V. Voskov	TU Delft, Co-Supervisor
	Dr. Peyman Taheri	TU Delft, Graduation Committee Member
	Dr. Mahnaz Aghajanloo	TU Delft, Daily-Supervisor

August 2025

Delft, Netherlands

Acknowledgements

I would like to express my sincere gratitude of Dr. Rouhi Farajzadeh for his support, supervision, and mentorship throughout the course of this thesis. His deep knowledge, consistent guidance, and constructive feedback have been crucial in shaping the scope and direction of my research. I really appreciate his availability and commitment to academic excellence, which played a significant role in the completion of this thesis.

I would also like to extent my thanks to Dr. Denis Voskov for his valuable input, thoughtful discussions, and dedication to high academic standards. His contributions have significantly enhanced the depth and quality of this research, and I am grateful for his support and insights throughout the development of this work.

Additionally, I would also like to thank Dr. Peyman Taheri for his participation as a member of the assessment committee and for the valuable comments and suggestions he provided, which contributed to the refinement of this thesis.

I am especially grateful to my daily supervisor, Dr. Mahnaz Aghajanloo, whose ongoing support and patience guided me through each phase of this research. Her technical expertise, insightful encouragement, and meticulous attention to detail were invaluable in maintaining the quality of the research rigorous and on track from start to finish.

In addition, I would also like to express my sincere appreciation to our laboratory technician, Mr. Michiel Slop, whose technical proficiency, commitment, and careful attention to detail played a crucial role in the successful execution of the experimental work for this thesis.

Even more, I would like to thank Dr. Sian Jones for her valuable assistance and support during the experimental phase of my work. I am also grateful to Mr. Diederik Boersma for sharing his knowledge and for his helpful feedback and comments during the review of my thesis report.

I am sincerely grateful to my friends for their constant encouragement, patience and support throughout this challenging journey. Their presence, thoughtful understanding, and unwavering belief in me served as a vital source of strength during moments of doubt and fatigue.

Lastly, I extend my deepest thanks to my family for their unwavering love, encouragement, and belief in my potential. Their continuous support has been a pillar of strength throughout this journey. The sacrifices they made, their endless patience, and their unconditional presence have been instrumental in enabling me to reach this important milestone. This achievement would not have been possible without their faith and devotion.

Abstract

Considering the global effort to combat climate change, a promising solution in reducing CO_2 emissions is the Carbon Capture and Storage (CCS) application. Such projects aim to store CO_2 inside subsurface geological formations. Depleted gas reservoirs are considered as one of the best options for CCS projects to take place. However, one of the main challenges that can be encountered is the impairment of CO_2 injectivity near the well caused by the formation of CO_2 hydrates which further result in porosity and permeability reduction of the reservoir rock. While the thermodynamic boundaries have been extensively studied, the kinetics of CO_2 hydrates inside porous media remain less investigated. So, this study investigates the kinetic behavior of CO_2 hydrate during both formation and dissociation within Bentheimer sandstone core samples under varying thermal conditions, aiming to get a better understanding of how thermal delivery either during hydrate formation with cooling or during hydrate dissociation with heating can affect the hydrates. On top of that, the effect of subcooling as a driving force is also investigated. During the experimental work of the study multiple core flood experiments with constant CO_2 injection (dynamic conditions) were conducted, applying different cooling and heating methods, with a specific focus on subcooling and the rates of thermal stimulation. A combination of pressure and temperature monitoring, computed tomography (CT) imaging and permeability measurements were employed to evaluate hydrate behavior in real time. The results showed that subcooling is a dominant driving force and higher degrees of subcooling resulted in shorter induction times, increased hydrate saturation, and greater permeability reductions. Very fast cooling rates led to faster hydrate formation which further resulted in greater permeability losses. Conversely, constant higher heating rates caused more hydrate dissociation and faster permeability recovery. A temperature threshold below the hydrate equilibrium temperature was consistently identified, where significant dissociation occurred, indicating that the porous medium inhibits hydrate formation and promotes hydrate dissociation. Hydrates formed under non-constant cooling dissociated more easily, while slow constant cooling resulted in hydrates that were more resistant. Despite full dissociation across all experiments a residual permeability loss of 8-10 % was observed. Additionally, hydrates formed under constant cooling methods displayed different permeability behavior compared to those formed under non-constant cooling methods, indicating a potential difference in pore-scale hydrate distribution. This thesis will delve into how temperature and subcooling can impact the kinetics of CO_2 hydrates formation and dissociation within the context of CCS in depleted gas reservoirs.

Table of Contents

Chapter 1: Introduction 1

1.1 Introduction and Background 1

1.2 Problem statement 3

1.3 Objectives 4

1.4 Relevance 4

1.5 Thesis Structure 5

Chapter 2: Literature Review 6

2.1 Introduction 6

2.2 Terminology 6

2.2.1 Induction time 6

2.2.2 Subcooling 6

2.2.3 Memory effect 7

2.3 Kinetics of CO_2 hydrate 7

2.4 Hydrate Formation 8

2.4.1 Nucleation 8

2.4.2 Growth 9

2.5 Hydrate Dissociation 10

2.6 Affecting parameters on hydrate kinetics 11

2.6.1 Impact of porous media 12

2.6.2 Subcooling 13

2.7 Identified Research Gaps 13

Chapter 3: Methodology 15

3.1 Overview of Experimental Approach 15

3.1.1 Purpose 16

3.2 Experimental Section 16

3.2.1 Experimental Material 16

3.2.2 Experimental Procedure 21

3.2.3 Challenges Encountered 22

3.3 Methodological Adjustments 23

3.3.1 Experiments 1 and 2 23

3.3.2 Experiment 3 24

3.3.3 Experiment 4 25

3.3.4 Experiment 5 26
3.3.5 Experiment 6 27
3.4 Data Processing and Calculations 28
3.4.1 Pressure and Temperature Data 28
3.4.2 Permeability Calculation 28
3.4.3 CT image analysis 29
3.4.4 Hydrate Properties Calculations 30
3.4.5 Volume Change of Brine due to CO_2 Solubility 32
Chapter 4: Discussion 36
4.1 Overview 36
4.2 Experimental Results 37
4.2.1 First Experiment 37
4.2.2 Second Experiment 39
4.2.3 Third Experiment 40
4.2.4 Fourth Experiment 43
4.2.5 Fifth Experiment 50
4.2.6 Sixth Experiment 60
4.3 Key Observations and Discussion 71
4.3.1 Thermodynamic conditions 71
4.3.2 CT Imaging Data 72
4.3.3 Permeability Data 74
4.3.4 Hydrate Saturation 78
4.3.5 Kinetic Analysis of Hydrate Formation and Dissociation 80
Chapter 5: Conclusions and Recommendations for Future Work 86
5.1 Conclusions 86
5.2 Recommendations 86
References 88

List of Figures

Figure 1: Schematic of the CCS process (Institute G. C., 2022). 1
Figure 2: Illustration of possible geological formations for storing CO_2 (Bashir et al., 2024). 3
Figure 3: Three-phase diagram of the CO_2-water mixture. The symbols I_w, L_c, L_w, H, and G represent ice water, liquid CO_2, liquid water, hydrate, and gas, respectively. HQP and LQP refer to high (L_wHL_CG) and low (I_wHL_WG) quadruple points. The smooth line represents the three-phase equilibrium line, the dotted line indicates the CO_2 condensed line, and the dashed line is ice line (Aghajanloo et al., 2024). 8
Figure 4: Gas consumption over time and identification of four different zones during the hydrate formation process as derived from a stirred tank reactor experiment (Yin et al., 2018). 10
Figure 5: Pictures of a Bentheimer core sample that was used during the experimental work of this thesis. The core sample is surrounded by a grey colored glue. 17
Figure 6: Graphical representation of the experimental apparatus of the fixed setup. The system consists of three sections: an inlet section supplying water/brine solution through the Vindum pump, and the gases (CO_2 or N_2) through the mass flow controllers (MFC); a central section that includes the core holder which is placed inside the refrigerator, equipped with four pressure transducers ($P_1 – P_4$), thermocouple (TC), and the differential pressure gauges (DP_1, DP_2) all monitored by an acquisition box; and an outlet section that contains the back pressure regulator (BPR), the vacuum pump, and the effluent. 18
Figure 7: Graphical representation of the experimental apparatus of the portable setup used under the medical CT scanner. The setup consists of the cylinders of the gases (N_2 or CO_2) that are connected to the mass flow controllers (MFC). It also includes the thermal circulator which is connected to the thermal jacket that is around the core holder. Next to the circulator the Quizix pump can be found which is responsible for the water/brine solution injection into the core. The data acquisition section follows, and consists of four pressure transducers ($P_1 – P_4$), the thermocouple (TC), and the differential pressure gauges (DP1, DP2). The outlet of the core holder is connected to the back pressure regulator (BPR) and the effluent. Lastly, the core holder is positioned within a medical CT scanner. 18
Figure 8: Picture of the portable experimental setup (CT setup). 20
Figure 9: Pictures of the some of the parts that consist the fixed setup. On the top left are the differential pressure gauges (dP). Next to them is a picture of the core placed inside of the core holder. On the bottom left is a picture of the core holder placed inside the refrigerator. Lastly, on the bottom right there is a picture of the Vindum pump. 20
Figure 10: Pressure and Temperature phase diagram of CO_2. The hydrate stability zone is defined by the CO_2 condensed line (black-dashed) and the equilibrium line that corresponds to 1wt% NaCl brine solution (blue line). The continuous arrows indicate the temperature steps of the 1st experiment whereas the dashed arrows indicate the temperature steps of the 2nd experiment. 24
Figure 11: Pressure and Temperature phase diagram of CO_2. The hydrate stability zone is defined by the CO_2 condensed line (black-dashed) and the equilibrium line that corresponds to 1wt% NaCl brine solution (blue line). The blue arrow indicates the cooling step, while the red arrows show the heating steps. 25
Figure 12: Pressure and Temperature phase diagram of CO_2. The hydrate stability zone is defined by the CO_2 condensed line (black-dashed) and the equilibrium line that corresponds to 1wt%

NaCl brine solution (blue line). The blue arrows indicate the cooling steps, while the red arrows show the heating steps. 26
Figure 13: Pressure and Temperature phase diagram of CO_2. The hydrate stability zone is defined by the CO_2 condensed line (black-dashed) and the equilibrium line that corresponds to 1wt% NaCl brine solution (blue line). The continuous arrows show the temperature steps of the first cycle, while the dashed arrows show the temperature steps of the second cycle. 27
Figure 14: Normalized permeability K/K0 [-] versus the Hydrate Saturation [%]. Symbols: Modified Kozeny Carman (orange), Capillary Tube - Grain Coating (grey), Kozeny Grain - Grain Coating (yellow), Kozeny Grain – Pore Filling (blue), and Capillary Tube – Pore Filling (green). ... 30
Figure 15: The solubility of CO2 into the water (mole/mole%) versus pressure and at different temperature curves. From this plot the solubility of CO2 was determined at 30 bar pressure and at temperatures that correspond to the temperature steps that were followed during each experiment. Because there are only curves related to -20C, -10C, 0C, 10C, and 20C, the solubility of temperatures in between these temperatures was estimated by using linear interpolation. This plot was generated from HydraFlash software. 33
Figure 16: Pressure and Temperature profile during CO_2 hydrate formation and dissociation for S_w=25% of 1 wt% NaCl brine solution. The initial conditions are: 30 bar. The light blue-colored part of the graph shows the hydrate formation stage, whereas the light red-colored part indicates the dissociation phase. 38
Figure 17: Pressure and temperature profile during CO_2 hydrate formation and dissociation for S_w=25% of 1 wt% NaCl brine solution. The initial conditions are: 30.6 bar and 3 ^oC. The light blue-colored part of the graph shows the hydrate formation stage, whereas the light red-colored part indicates the dissociation phase. 40
Figure 18: Pressure and temperature profile of the core during CO2 hydrate formation and dissociation for S_w=25% of 1 wt% NaCl brine solution. The initial conditions are: 29.8 bar and -3 ^oC. The light blue-colored part of the graph shows the hydrate formation stage, whereas the light red-colored part indicates the dissociation phase. 41
Figure 19: Dynamic CT images of water/hydrate saturation during the brine saturation process of horizontal Bentheimer core (PV = 44 ml) as well as during hydrate formation (Direct Cooling) and dissociation (Step Heating). Flow direction is from left to right. (Colors indicate water + hydrate saturation qualitatively. Red: high water/hydrate saturation; green/yellow: intermediate saturation; blue: low saturation). 42
Figure 20: The water plus hydrate saturation is plotted for different stages of the experiment as obtained from the CT images during each of these steps (columns), whereas the water plus hydrate saturation difference from the initial brine saturation at every step is represented with the black curve. 43
Figure 21: Pressure and temperature profile of the core during CO_2 hydrate formation and dissociation for S_w = 24% of 1 wt% NaCl brine solution. The initial conditions of the experiment are: 30.1 bar and 9.5 ^oC. The light blue-colored part of the graph shows the hydrate formation stage, whereas the light red-colored part indicates the dissociation phase. 45
Figure 22: Dynamic CT images of water/hydrate saturation during the brine saturation process of horizontal Bentheimer core as well as during hydrate formation (Step Cooling) and dissociation (Step Heating). Flow direction is from left to right. (Colors indicate water + hydrate saturation qualitatively. Red: high water/hydrate saturation; green/yellow: intermediate saturation; blue: low saturation). 46

Figure 23: The water plus hydrate saturation is plotted for different stages of the experiment as obtained from the CT images during each of these steps (columns), whereas the water plus hydrate saturation difference from the initial brine saturation at every step is represented with the black curve. 47
Figure 24: Permeability values of the sand stone core sample during different phases of the experiment as calculated after the implementation of gas permeability tests and Darcy's Law. . 48
Figure 25: Hydrate saturation, CO_2 solubility-related saturation increase, and water-to-hydrate conversion that were calculated at each temperature step of the fourth experiment. Bars represent the calculated hydrate saturation and the portion attributed to dissolved CO_2, while the line (secondary axis) shows the corresponding water-to-hydrate conversion percentages. .. 49
Figure 26: Water + Hydrate saturation [%] in columns, together with the amount of CO2 that was consumed [g] from the hydrate cages (black line) at every stage of the experiment. 50
Figure 27: Pressure and temperature profile of the core during CO_2 hydrate formation and dissociation for two cycles of cooling and heating, for S_w = 27.8% of 1 wt% NaCl brine solution. The initial conditions of the experiment are: 29.6 bar and 20 ^oC. The light blue-colored parts of the graph show the hydrate formation stage of each cycle, whereas the light red-colored parts indicate the dissociation phase of each cycle..... 51
Figure 28: Dynamic CT images of water/hydrate saturation during the brine saturation process of horizontal Bentheimer core as well as during hydrate formation (Step Cooling) and dissociation (Step Heating). Flow direction is from left to right. (Colors indicate water + hydrate saturation qualitatively. Red: high water/hydrate saturation; green/yellow: intermediate saturation; blue: low saturation). 52
Figure 29: Dynamic CT images of water/hydrate saturation during the brine saturation process of horizontal Bentheimer core as well as during hydrate formation (Step Cooling) and dissociation (Step Heating). Flow direction is from left to right. (Colors indicate water + hydrate saturation qualitatively. Red: high water/hydrate saturation; green/yellow: intermediate saturation; blue: low saturation). 53
Figure 30: The water plus hydrate saturation is plotted for different stages of the first cycle of the experiment as obtained from the CT images during each of these steps (columns), whereas the water plus hydrate saturation difference from the initial brine saturation at every step is represented with the black curve..... 54
Figure 31: The water plus hydrate saturation is plotted for different stages of the second cycle of the experiment as obtained from the CT images during each of these steps (columns), whereas the water plus hydrate saturation difference from the initial brine saturation at every step is represented with the black curve..... 55
Figure 32: Permeability values of the sand stone core sample during different phases of the experiment’s first cycle. 56
Figure 33: Permeability values of the sand stone core sample during different temperatures of the second cycle of the experiment. 56
Figure 34: Hydrate saturation, CO_2 solubility-related saturation increase, and water-to-hydrate conversion that were calculated at each temperature step of the fifth experiment’s first cycle. Bars represent the calculated hydrate saturation and the portion attributed to dissolved CO_2, while the line (secondary axis) shows the corresponding water-to-hydrate conversion percentages. 57

Figure 35: Water + Hydrate saturation [%] in columns, together with the amount of CO2 that was consumed [g] from the hydrate cages (black line) at every stage of the experiment's first cycle. 58
Figure 36: Hydrate saturation, CO_2 solubility-related saturation increase, and water-to-hydrate conversion that were calculated at each temperature step of the fifth experiment's second cycle. Bars represent the calculated hydrate saturation and the portion attributed to dissolved CO_2, while the line (secondary axis) shows the corresponding water-to-hydrate conversion percentages. 59
Figure 37: Water + Hydrate saturation [%] in columns, together with the amount of CO2 that was consumed [g] from the hydrate cages (black line) at every stage of the experiment's second cycle. 59
Figure 38: Pressure and temperature profile of the core during CO_2 hydrate formation and dissociation for two cycles of hydrate formation and dissociation for S_w = 28 % of 1 wt% NaCl brine solution. The initial conditions of the experiment are: 29.7 bar and 20 ^oC. The light blue-colored parts of the graph show the hydrate formation stage of each cycle, whereas the light red-colored parts indicate the dissociation phase of each cycle. 61
Figure 39: Dynamic CT images of water/hydrate saturation during the brine saturation process of horizontal Bentheimer core as well as during hydrate formation (Ramp Cooling) and dissociation (Ramp Heating). Flow direction is from left to right. (Colors indicate water + hydrate saturation qualitatively. Red: high water/hydrate saturation; green/yellow: intermediate saturation; blue: low saturation). 62
Figure 40: Dynamic CT images of water/hydrate saturation during the brine saturation process of horizontal Bentheimer core as well as during hydrate formation (Ramp Cooling) and dissociation (Ramp Heating). Flow direction is from left to right. (Colors indicate water + hydrate saturation qualitatively. Red: high water/hydrate saturation; green/yellow: intermediate saturation; blue: low saturation). 63
Figure 41: The water plus hydrate saturation is plotted for different stages of the first cycle of the experiment as obtained from the CT images during each of these steps (columns), whereas the water plus hydrate saturation difference from the initial brine saturation at every step is represented with the black curve. 64
Figure 42: The water plus hydrate saturation is plotted for different stages of the second cycle of the experiment as obtained from the CT images during each of these steps (columns), whereas the water plus hydrate saturation difference from the initial brine saturation at every step is represented with the black curve. 65
Figure 43: Permeability values of the sand stone core sample during different temperatures of the first cycle of the experiment, as calculated after the implementation of gas permeability tests and Darcy's Law. 66
Figure 44: Permeability values of the sand stone core sample during different temperatures of the second cycle of the experiment, as calculated after the implementation of gas permeability tests and Darcy's Law. 67
Figure 45: Hydrate saturation, CO_2 solubility-related saturation increase, and water-to-hydrate conversion that were calculated at each temperature step of the sixth experiment's first cycle. Bars represent the calculated hydrate saturation and the portion attributed to dissolved CO_2, while the line (secondary axis) shows the corresponding water-to-hydrate conversion percentages. 68

Figure 46: Water + Hydrate saturation [%] in columns, together with the amount of CO2 that was consumed [g] from the hydrate cages (black line) at every temperature change throughout the first cycle of the experiment. 69
Figure 47: Hydrate saturation, CO_2 solubility-related saturation increase, and water-to-hydrate conversion that were calculated at each temperature step of the sixth experiment's second cycle. Bars represent the calculated hydrate saturation and the portion attributed to dissolved CO_2, while the line (secondary axis) shows the corresponding water-to-hydrate conversion percentages. 70
Figure 48: Water + Hydrate saturation [%] in columns, together with the amount of CO_2 that was consumed [g] from the hydrate cages (black line) at every temperature change throughout the second cycle of the experiment. 70
Figure 49: Rate of hydrate dissociation presented as water + hydrate saturation over time as obtained from the analysis of the CT images for five different cycles of hydrate formation and dissociation. 74
Figure 50: Dynamic permeability recovery during hydrate dissociation. 76
Figure 51: Dynamic permeability reduction during cooling process. 77
Figure 52: Dynamic permeability recovery during heating process. 77
Figure 53: Estimation of the rate of hydrate saturation based on the dynamic permeability change. 79
Figure 54: Original data of the Normalized permeability (k/k_0) vs Hydrate saturation (S_h). 80
Figure 55: Original data of the Normalized permeability (k/k_0) vs the Corrected Hydrate saturation (S_h). 80
Figure 56: Induction time of conducted experiments versus fugacity ratio. 81
Figure 57: Determination of the parameters m and k. 81
Figure 58: Induction time versus subcooling for the conducted experiments. 82
Figure 59: Determination of the parameters m and with subcooling as the driving force. 82
Figure 60: Hydrate formation rate (hydrate saturation difference over time) versus the fugacity difference for all experimental cycles combined. 83
Figure 61: Hydrate dissociation rate (hydrate saturation difference over time) versus the fugacity difference for all experimental cycles combined. 83
Figure 62: Hydrate dissociation rate (hydrate saturation difference over time) in logarithmic scale versus the inverse of temperature. 84

List of Tables

Table 1: The following table summarizes all the experimental conditions that were employed during the experimental work of this study. More specifically, the cooling/heating method. The subcooling, and the cooling/heating step interval of every experiment are listed below. 23
Table 2: List of parameters a_1 through a_{10} for equation (15) as obtained from (D. Li et al., 2011) 34
Table 3: A list of all the data that was collected during the experimental work. Under each experiment, the green boxes indicate what type of data was obtained from it, whereas the red boxes indicate parts that were not focused on. 36
Table 4: Summary of experimental parameters and observations: degree of subcooling, formation and dissociation methods, induction time, pressure drop and temperature increase during hydrate formation, and dissociation onset. 37
Table 5: The induction time, pressure-drop, and temperature increase that were recorded in every experiment/cycle during the hydrate formation phase: 71
Table 6: Representation of the core's average saturation change at five different stages of each experiment as it was calculated from the available CT scans. Temp [°C], indicates the temperature that the core had at each of the five stages. ΔS [%], shows the saturation difference from the initial brine saturation that was achieved in every experiment. Time [h], is only shown in the four dissociation stages, and shows the number of hours from the end of the hydrate formation phase until the time when each measurement (CT scan) was taken. 72
Table 7: Representation of the core's permeability change at five different stages of each experiment as it was calculated from gas permeability tests. Temp [°C], indicates the temperature that the core had at each of the five stages. Δk [D], shows the permeability difference of the core after brine saturation phase minus the permeability after hydrate formation was achieved. But for the dissociation Δk [D] is the difference from the value after the end of hydrate formation. Time [h], is only shown in the four dissociation stages, and shows the number of hours from the end of the hydrate formation phase until the time when each measurement (gas permeability test) was performed. 74
Table 8: Representation of the core's average hydrate saturation change at five different stages of each experiment as it was calculated from the available CT scans and gas permeability tests. Temp [°C], indicates the temperature that the core had at each of the five stages. S_h [%], shows the hydrate saturation value. Time [h], is only shown in the four dissociation stages, and shows the number of hours from the end of the hydrate formation phase until the time when each measurement (CT scan and gas permeability test) was taken. 78

Chapter 1: Introduction

1.1 Introduction and Background

Climate change is one of the most pressing issues facing the world today, and the role of carbon capture and storage (CCS) in mitigating its effects cannot be overstated. In fact, carbon dioxide (CO_2) as one of the main greenhouse gasses has been released into the atmosphere for decades mainly by the process of burning fossil fuels for industrial processes, power generation, and transportation leading to excessive concentrations (Raza et al., 2019). According to the International Energy Agency, it is claimed that this technology can potentially reduce 17% of global CO_2 emissions by 2050 - and the CCS must be part of the policy in every country worldwide in an attempt to mitigate the severe effects of global warming (Metz et al., 2005). Technically speaking, CCS is the process of capturing CO_2 emissions from large point sources like power plants, industrial facilities and natural gas wells, transporting it via pipelines to a favorable storage location, and injecting it into underground geological formations, where it can be safely and permanently (thousands of years) stored, preventing it from entering the atmosphere and contributing to global warming (Bachu & Shaw, 2003).

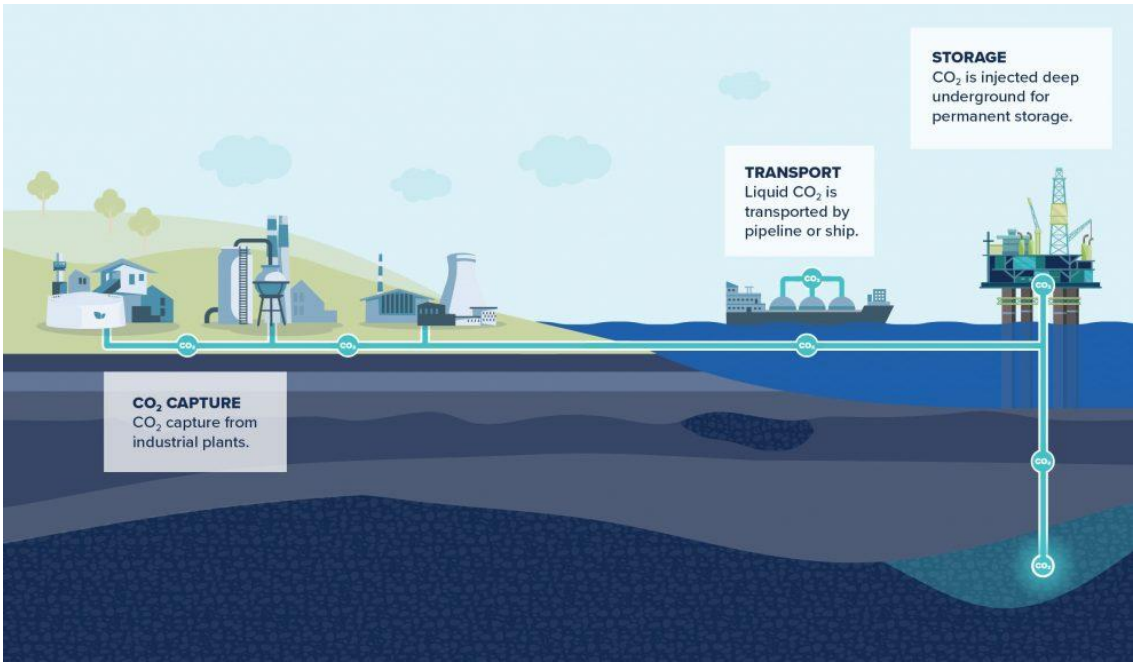

Figure 1: Schematic of the CCS process (Institute G. C., 2022).

Collectively, there are many parameters, phenomena, and processes included in the processes of storing CO_2 into the subsurface, which must be carefully measured, monitored and recorded to ensure that the injected CO_2 remains confined for thousands of years without escaping back to the surface (Vishal & Singh, 2016). One of the most important parameters that needs to be considered is the storage site, mainly-the geological formation that is going to facilitate the injected CO_2. The geological formations that are usually targeted are salt beds, coal beds, deep sandstone and carbonate aquifers, and sedimentary basins with oil and gas reservoirs. Depleted oil and gas reservoirs pose the best option for CO_2 storage when compared to alternative

reservoirs due to their unique combination of advantages. Unlike unminable coal seams, which offer large storage capacity but come with prohibitively high costs, depleted oil and gas reservoirs are more economically viable because they often utilize the already existing infrastructure such as wells and pipelines (Kocs, 2017). While mined salt domes provide perfect integrity and storage, their construction and operational costs are similarly high, making them less practical for large-scale CCS projects (Raza et al., 2019). Deep saline aquifers, though offering significant storage capacity, pose uncertainties regarding their long-term storage integrity due to limited exploration and characterization (Peysson et al., 2014). In contrast, depleted oil and gas reservoirs have already demonstrated their structural integrity and containment ability over millions of years, as they have naturally trapped hydrocarbons under high pressure without significant leakage (Boreham et al., 2011; Raza et al., 2017). Even more, their geological properties, such as cap rock seals and well-characterized subsurface conditions, ensure reliability for CO_2 storage (Saeedi & Rezaee, 2012). Overall, combined with their economic and operational benefits, depleted oil and gas reservoirs represent the most feasible and effective option for CCS projects.

Apart from all the benefits regarding CO_2 injection into depleted oil and gas reservoirs, these types of reservoirs pose some potential challenges concerning containment, injectivity, and well integrity (Aghajanloo et al., 2024). More specifically, CCS projects largely rely on the injectivity of the well, which is defined as the volume or mass of injected CO_2 for a certain pressure gradient (Hoteit et al., 2019). However, injectivity might be impaired by the potential formation of CO_2 hydrates resulting from the isenthalpic expansion of the CO_2 from the dense phase to the gas phase upon entering the low pressure depleted reservoir. The primary hydrate formation condition refers to the specific combination of low temperature and high pressure under which CO_2 molecules become encapsulated in a lattice of water molecules, resulting in solid hydrates. In depleted gas reservoirs, these conditions are particularly likely to occur near the interface between the well tubing and the reservoir.

While CO_2 is injected into the reservoir the Joule-Thomson cooling effect can take place due to the fact that the high-pressure CO_2 is injected into a low-pressure reservoir leading to isenthalpic expansion, which further causes a temperature drop. This temperature reduction together with enough water available inside the porous medium cause the formation of CO_2 hydrates, resulting in the reduction of both the porosity and permeability of the reservoir (Chesnokov et al., 2024). In addition to thermodynamic conditions (T and P), the process of hydrate formation is influenced by numerous factors related to the reservoir characteristics, such as, rock mineralogy, porosity, and permeability. In situ brine properties also play a significant role, including saturation levels, salinity, and the type of dissolved salts. Furthermore, the impurities in terms of gas composition, and fraction are critical in determining the hydrate behavior (Gauteplass et al., 2020).

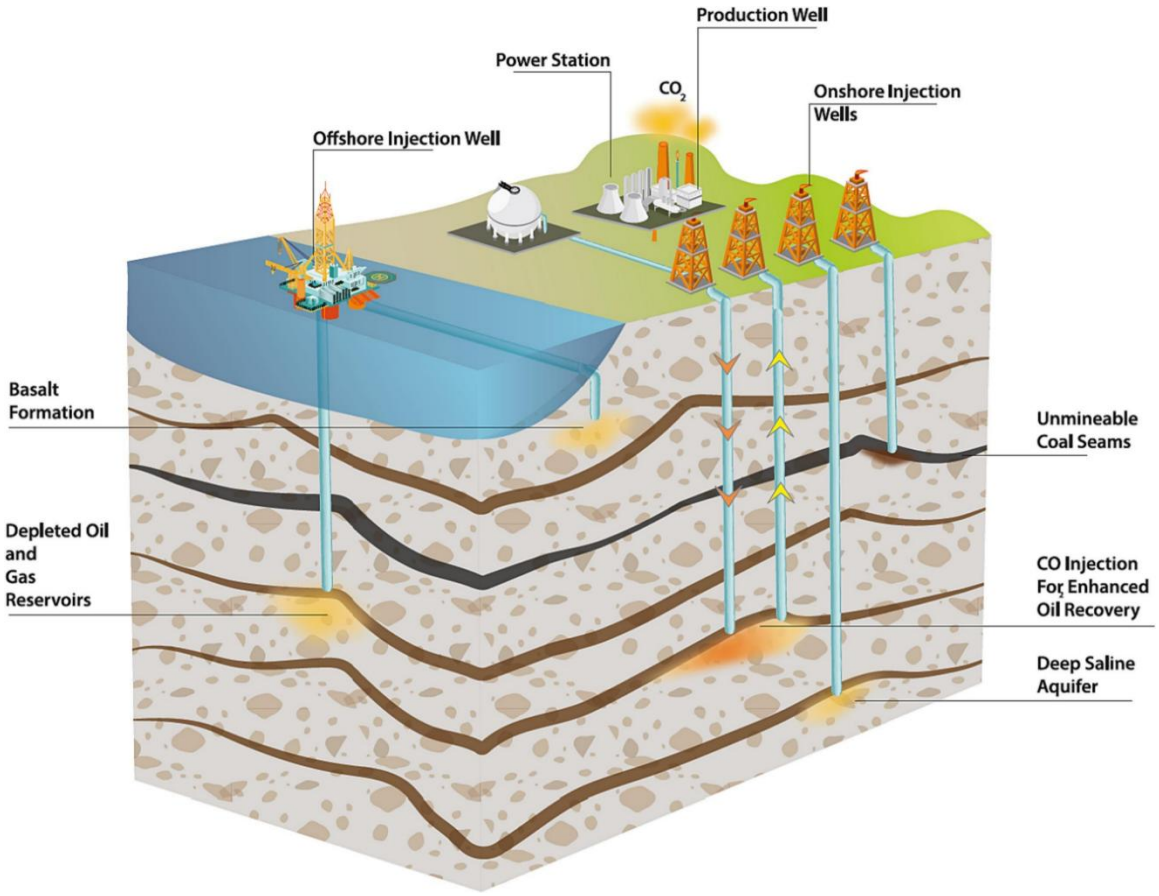

Figure 2: Illustration of possible geological formations for storing CO_2 (Bashir et al., 2024).

In the context of CO_2 sequestration in depleted gas fields, the relevance of CO_2 hydrate formation becomes particularly significant, as it can directly impact the efficiency and safety of the storage operations (Bui et al., 2018). Over the past decades, extensive research has focused on the thermodynamic behavior of CO_2 hydrates in bulk systems under various conditions and using different materials (Yang et al., 2013; Zheng et al., 2020). However, kinetic processes – including the rates of hydrate formation and dissociation - remain comparatively underexplored, especially under conditions relevant to CCS operations. The existing literature offers only a few precedent cases of CO_2 hydrate formation at the field scale or in field-related processes. These examples are scattered and not directly representative of conditions relevant to CO_2 injection in depleted gas fields (Jadhawar et al., 2006). Nonetheless, they demonstrate that CO_2 hydrates or ice can form in principle (Z. Li et al., 2023) and when they do via various processes (Sloan Jr & Fleyfel, 1991), they can significantly impair injectivity.

1.2 Problem statement

The primary problem addressed in this thesis is the insufficient understanding of the kinetics of CO_2 hydrate formation and dissociation under reservoir-like conditions, which is critical for optimizing CCS operations in depleted gas fields. Kinetic behavior, such as the rate of hydrate

nucleation, growth, and dissociation, directly impact important operational parameters, including the injectivity and long-lasting reservoir performance. For example, the rate and extent of hydrate formation determine hydrate saturation, which can significantly reduce reservoir permeability and restrict CO_2 flow, thereby impairing injectivity. Therefore, while thermodynamic boundaries are well established, important knowledge gaps persist regarding hydrate kinetics in porous media. The confined geometry of reservoir rock introduces complexities such as pore size effects, surface wettability, and heterogeneous fluid distribution, all of which influence hydrate nucleation, growth, and dissociation. Even more, there is little understanding of how varying degrees of subcooling can affect the kinetics during the hydrate formation process and how this further impacts the time needed for the formed hydrates to dissociate. Additionally, there is a lack of understanding on how dynamic conditions (e.g., excess injected CO_2) affect the dissolution of CO_2, and ultimately hydrate saturation. Finally, there is insufficient insight regarding the effect of different formation/dissociation methods in the context of how smaller or bigger temperature changes within the system can impact the kinetics of CO_2 hydrates. Addressing these gaps requires targeted research into both the formation and dissociation kinetics of CO_2 hydrates under reservoir-like conditions.

1.3 Objectives

Building on the identified knowledge gap in CO_2 hydrate kinetics under reservoir-like conditions, this study focuses on two main objectives. Firstly, it aims to investigate the impact of hydrate formation/dissociation methods on kinetic parameters of CO_2 hydrates inside porous media using the isothermal (direct cooling), step cooling/heating, and ramping (constant cooling/heating) method. Secondly, the study seeks to investigate the effect of subcooling as a key driving force for hydrate formation and dissociation on the kinetics of these processes. The aforementioned objectives are studied using core-flood experiments under the wellbore pressure conditions (range ~25-35 bar) so that a comprehensive understanding of how CO_2 hydrates form and dissociate can be achieved. Therefore, this thesis focuses exclusively on kinetic aspects of CO_2 hydrate to address this knowledge gap and provide practical insights for improving CCS efficiency and reliability.

1.4 Relevance

The research of this thesis is directly relevant to CCS operations in depleted gas reservoirs, in which CO_2 hydrate formation can cause permeability reduction, injectivity impairment, and cause flow restrictions during CO_2 injection and storage. A very important challenge in these porous settings is the ability of predicting and controlling the formation and dissociation kinetic of hydrate under varying thermal conditions. Subcooling, in particular, acts as a driving force for hydrate nucleation and growth, but its impact on formation and dissociation kinetics remains insufficiently understood. By investigating how different degrees of subcooling resulting from Joule-Thomson (JT) cooling during CO_2 expansion affect the kinetics of CO_2 hydrate formation and dissociation, this study provides insights for designing more efficient injection strategies. Furthermore, a better

understanding of these kinetic processes can assist in partial mitigation of hydrate related risks, improve reservoir management, and lastly enhance the safety and reliability of CCS technologies.

1.5 Thesis Structure

This study is structured in five chapters. Chapter 1 establishes the project's context, outlines the research objectives while providing the scope and relevance of this study, and lists an overview of the report. In Chapter 2, the theoretical foundation around CO_2 hydrates is presented briefly regarding their structure, and the processes of formation and dissociation. Though, the main focus and the biggest part of the chapter presents an overview of the information that is available in the literature about the kinetics of CO_2 hydrates. Chapter 3 focuses on the experimental setup that was used, the procedures that were followed, details about the collected data, and their processing together with all the mathematical and computational methods that were implemented. In total, the results of 6 experiments are covered. A comprehensive discussion is provided in Chapter 4, covering the experimental results and the key observations or patterns that were made out of them. Finally, Chapter 5 is dedicated to the main findings and the final remarks on how this work contributed in the understanding of CO_2 hydrates behavior.

Chapter 2: Literature Review

2.1 Introduction

Depleted gas reservoirs have been found to be a highly promising option for the geological storage of CO_2 because of their existing infrastructure, and well-identified geological properties (Raza et al., 2016). Their potential for facilitating large-scale CCS projects can significantly help on the widely increasing effort for mitigating greenhouse gas emissions (Indina et al., 2024). However, a very serious problem that is encountered in such projects is the formation of CO_2 hydrates near the wellbore area during the injection of CO_2 into the reservoir (de Kok, 2024). The presence of gas hydrates in the reservoir impacts the feasibility and efficiency of the entire CCS project, as hydrate formation blocks the pores of the porous medium, reducing porosity and permeability, and consequently restricting CO2 flow and lowering storage capacity (Heidarabad & Shin, 2024). The insufficient CO_2 storage amount can result in the failure of the CCS project because in order to meet the expected amount of CO_2 to be stored in the reservoir, some mitigation methods would be required which will increase by a lot the operational costs of the project (Perez-Perez et al., 2023). So, understanding the kinetics of CO_2 hydrates formation and dissociation under reservoir-like conditions is crucial for predicting and controlling the aforementioned risks. This chapter aims to investigate the kinetics of CO_2 hydrate formation and dissociation in porous media using different thermal methods. Even more, knowledge gaps are being addressed, especially regarding experiments that mimic depleted reservoir-like conditions.

2.2 Terminology

This section defines some important terms that are relevant to the overall topic of the study.

2.2.1 Induction time

The induction time is defined as the time elapsed until the macroscopic detection of a hydrate nucleation based on pressure and temperature measurements (Gambelli & Rossi, 2022). At this time the thermodynamic conditions of the system are either at equilibrium or within the hydrate region.

2.2.2 Subcooling

Subcooling refers to the difference between the equilibrium temperature (T_{eq} [C]) at which hydrates form, and the experimental or set temperature (T_{exp} [C]), both at the same pressure conditions (Sloan et al., 2007).

$$\Delta T = T_{eq} - T_{exp}$$

2.2.3 Memory effect

Studies have shown that the time required to form hydrates is significantly shorter when suing water that has been previously part of a hydrate structure, in comparison with water that has never formed hydrates (Rossi et al., 2021). This interesting behavior is known as the memory effect, a phenomenon where dissociated hydrates maintain a structural memory of their previous arrangement. More specifically, in cases where hydrates are dissociated thermally at moderate temperatures, water molecules mimic the original hydrate framework, even after the breakdown of hydrates into water and gas (Wen et al., 2021). However, this phenomenon is not permanent and can be completely eliminated if the condition shift sufficiently far from equilibrium and move outside the hydrate zone (Sloan et al., 2007).

2.3 Kinetics of CO_2 hydrate

The processes of hydrate formation and dissociation are governed by complex kinetics that are related to the rate and the extent of hydrate stability under different conditions, and are described as time-dependent phenomena (Liu et al., 2022). Unlike the thermodynamic phase boundaries, hydrate kinetics are more difficult to measure and predict. This complexity arises from several factors that can be related to one another. One key challenge is the stochastic nature of hydrate nucleation, that results in significant variability in induction times, even under identical experimental conditions. Additionally, the hydrate growth phase is very sensitive to system variables like water availability, gas solubility, interfacial area, temperature, pressure, and the medium's physical properties. All these dynamic interactions make the quantification of the kinetics of hydrates really uncertain. As a result, measurements of kinetic parameters typically show bigger variability and lower reproducibility, often deviating by an order of magnitude compared to thermodynamic data (Sloan et al., 2007).

Over the years numerous studies have been conducted investigating the kinetics of CO_2 hydrate formation and dissociation across several applications both in bulk and porous media conditions. These studies intent to identify the factors that influence hydrate behavior under various operational conditions. General investigations into CO_2 hydrate kinetics have explored the formation and dissociation processes under controlled laboratory conditions to identify how parameters like temperature, pressure, water saturation and additives, influence the kinetics of these processes (Feyzi & Mohebbi, 2020; Hu & Xiao, 2023; S. Sun et al., 2022). There are also studies that have examined the same parameters but they aim for different applications, namely, hydrate-based storage in marine environments (Dhamu et al., 2023; Sahu et al., 2022; Zhao & Zhang, 2024), gas recovery from CH_4 hydrates by replacing them with CO_2 hydrates, and the relevance between the two hydrates (Komai et al., 2003; Z. Li et al., 2023; Prasad & Kiran, 2020), and CCS in depleted gas reservoirs (Askarova et al., 2023; de Kok, 2024; P. Wang et al., 2019). Due to all these applications and all the different studies that are related to them, a significant amount of knowledge regarding the kinetics of CO_2 hydrates has been gathered, even though each application has its own purpose and parameters.

The hydrate nucleation takes place as soon as the thermodynamic conditions of binary water-CO_2 system is either located on equilibrium or inside the hydrate zone (Yin et al., 2018). The hydrate

can be seen in Figure 3 and is denoted by H-G (with gaseous CO_2) and H-L_C (with liquid CO_2), if the temperature is below the hydrate phase boundary inside the stability zone and enough water is available inside the porous medium, solid hydrates can form. The kinetics of hydrate formation include two different stages, hydrate nucleation and hydrate growth (Sloan, 2003). The process of hydrate formation can be explained by examining the changes of gas consumption over time inside a pressurized system. In this kind of setup, a pressurized water containing cell is brought to pressure and temperature conditions that fall inside the hydrate stability zone. Gas is constantly injected into the system to maintain the pressure constant as the reaction progresses. Over time, when the system stabilizes, hydrates formation starts to take place, reflecting the gradual consumption of CO_2 during the process. The dynamic interaction between CO_2, water and the controlled environment drives the formation of hydrates (Yin et al., 2018).

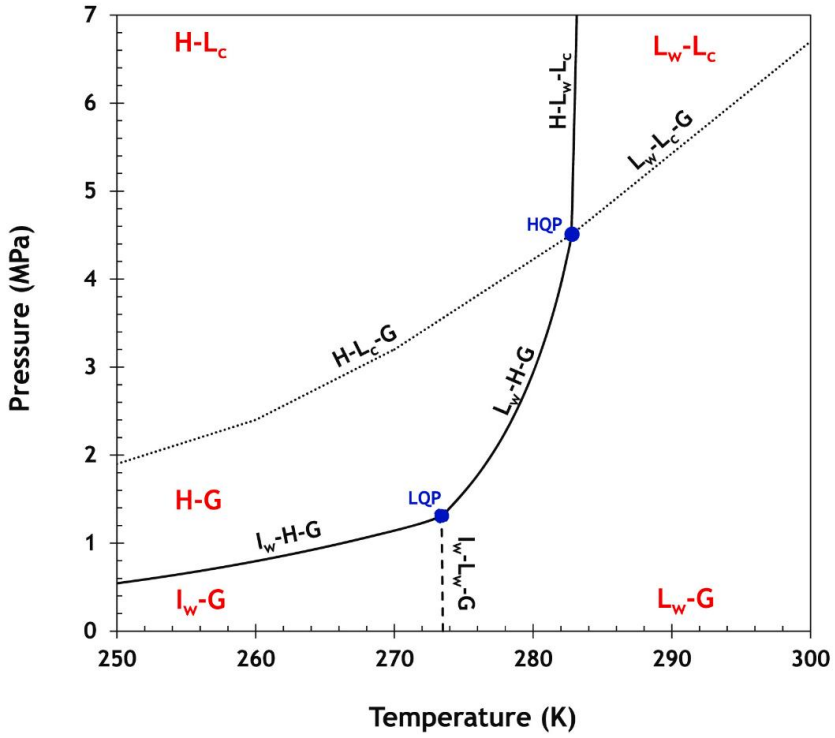

Figure 3: Three-phase diagram of the CO_2-water mixture. The symbols I_w, L_c, L_w, H, and G represent ice water, liquid CO_2, liquid water, hydrate, and gas, respectively. HQP and LQP refer to high (L_wHL_CG) and low (I_wHL_WG) quadruple points. The smooth line represents the three-phase equilibrium line, the dotted line indicates the CO_2 condensed line, and the dashed line is ice line (Aghajanloo et al., 2024).

2.4 Hydrate Formation

2.4.1 Nucleation

Varius experimental studies have investigated CO_2 hydrate nucleation inside porous media, consistently emphasizing the stochastic nature of this phase and its sensitivity to the porous medium characteristics, such as surface area and pore characteristics. Researchers such as Mekala et al., (2014) and Zatsepina & Buffett, (2002), reported significantly longer and more variable

induction times within porous media in comparison with bulk systems, attributing this to reduced gas-water contact and heterogeneous wetting consitions. Similarly Hosseini Zadeh et al., (2023), found that nucleation is more likely to initiate in larger pores where thermodynamic conditions are more favorable.

Nucleation, in the context of gas hydrates, refers to the initial phase transition from a supersaturated water–gas system into the crystalline hydrate structure. In porous media, nucleation can be promoted or inhibited by several competing mechanisms. For instance, hydrophilic materials may retain water in pore throats while hydrophobic materials enhance gas retention, leading to selective site nucleation. Pore-scale confinement effects further impact the local pressure and temperature thresholds required for nucleation, effectively shifting the phase boundary (Clennell et al., 1999).

These findings underscore the importance of pore size distribution and surface heterogeneity in governing hydrate induction behavior. Particularly in CCS contexts, unpredictable or delayed nucleation in reservoir formations poses challenges for injection control and hydrate risk modeling.

2.4.2 Growth

The available information in the literature points to substantial deviations in growth kinetics when hydrates form inside porous structures. Palodkar et al., (2016), demonstrated that hydrate growth is limited by mass and heat transfer constraints, especially in fine-grained media. Additionally, growth tends to localize near the gas entry point, where the concentration of CO_2 is higher, and diminishes due to permeability loss from accumulating hydrates.

The stage of hydrate growth takes place after the initial nucleation. It involves the expansion of the already formed hydrate crystals, and involves the transfer of water, gas, and hydrate components across various interfaces (gas-liquid, liquid-hydrate, and hydrate-solid). It is a dynamic, time-dependent process on various scales (macroscopic and microscopic). The rates of growth are controlled mainly by temperature, pressure, gas composition, impurities and mass transfer limitations (Ke et al., 2019). In the beginning of growth, the rate of CO_2 consumption is quickly increased leading to fast hydrate growth. This means that CO_2 molecules are transferred from gas to liquid phase and massively captured inside the hydrate cages. While water and CO_2 molecules are consumed during the hydrate formation phase, the rate of CO_2 consumption (hydrate formation) decreases gradually over time, leading to a plateau close to the completion of the hydrate formation process (see Figure 4).

Moreover, growth morphology inside porous media is non-uniform (Kou et al., 2021). As it depends on pore geometry and fluid saturation, hydrates may form interconnected networks or discontinuous clusters. The resultant pore-filling pattern influences reservoir-scale properties such as permeability and capillary pressure, with direct implications for CO_2 injectivity during sequestration operations.

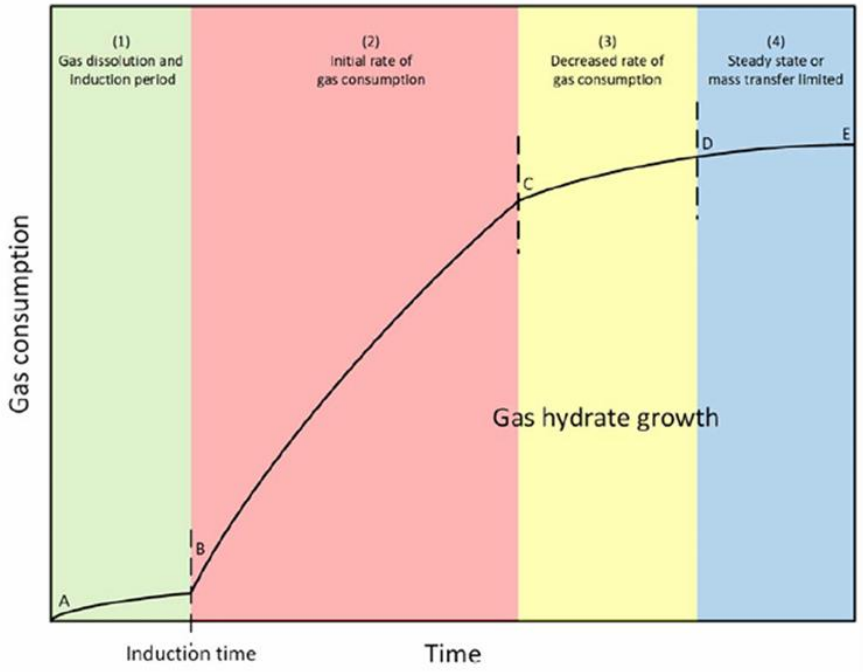

Figure 4: Gas consumption over time and identification of four different zones during the hydrate formation process as derived from a stirred tank reactor experiment (Yin et al., 2018).

For both nucleation and growth, introducing a driving force is a key component that is used for modeling these two kinetic processes. Numerous studies implement various driving forces in their models, such as: chemical potential, the mole fraction of CO_2 dissolved difference, the fugacity difference, the Gibbs free energy difference and the degree of subcooling (Q. Sun & Kang, 2016). For example, Aghajanloo et al., (2022), introduced a kinetic model that relates the induction time to the fugacity difference between the experimental conditions and the equilibrium state:

$$t_{ind} = k\left(\frac{f_g}{f_{eq}} - 1\right)^{-m} \quad (1)$$

where k is the primary apparent rate constant and m is the index parameter. Additionally, f_g and f_{eq} are the fugacity of gas molecules in the gas/vapor phase and in the three phase equilibrium conditions respectively. This equation is going to be used in the discussion chapter at an attempt to correlate the experimental results of this study.

2.5 Hydrate Dissociation

Dissociation can be considered as the reverse of hydrate formation and it involves the breakdown of hydrate crystals into water and CO_2. Some techniques that can be found on the literature that can induce hydrate dissociation are depressurization, thermal stimulation, injection of additives (chemical solutions), or even a combination of all of them (Q. Sun & Kang, 2016). Thermal stimulation is one of the most common methods, and the one used in this study, where heat is directly applied to the system. The temperature around the hydrate structures is increased,

providing the necessary energy to lead to the bond breakdown (Iwai et al., 2018) which is fundamentally governed by heat transfer (Zhao et al., 2021).

The degree of subcooling during hydrate formation has a significant impact on subsequent dissociation behavior. Hydrates formed at higher subcooling levels tend to be more thermally stable and compact, leading to slower and more resistant dissociation (Tariq et al., 2022). This behavior is evident inside porous media where capillary forces and pore confinement cause additional thermodynamic stabilization. Subcooling influences both the distribution of hydrates and their physical structure within the pores. When hydrates are formed in greater subcooling they tend to occupy smaller pores and grow into denser masses, causing a reduction in permeability of the medium and thus obstruct mass transfer during dissociation (Benmesbah et al., 2022). The confined geometries that exist inside porous media can potentially hinder the escape of released gas, which can locally suppress further dissociation due to increased partial pressure.

Several kinetic models have been proposed to capture the rate of hydrate dissociation. A very often cited approach describes both the formation (growth) and the dissociation rate to be proportional to the fugacity difference between the experimental conditions and the hydrate equilibrium state (Wang et al., 2023):

$$\frac{dS_h}{dt} = -k \cdot A_p \cdot (f_{eq} - f_g) \tag{2}$$

where k again is the rate constant, A_p is the surface area of gas hydrate, f_{eq} is the equilibrium fugacity, and f_g is the fugacity at hydrate surface. The rate constant k varies with gas molecules and it can also be expressed as an Arrhenius-type equation (Cao et al., 2021):

$$k = k_{sd} \cdot e^{-\Delta E/RT} \tag{3}$$

where k_{sd} is the equivalent intrinsic rate constant, ΔE is the activation energy of CO_2 hydrates, R is the universal gas constant, and T is the temperature inside the core. These equations are also going to be used during the discussion chapter for correlation with the experimental results of the study. However, for simplification reasons the surface area is assumed to be included within the rate constant.

2.6 Affecting parameters on hydrate kinetics

The kinetics of hydrate formation and dissociation in porous media are influenced by various thermophysical, structural, and operational factors. This section discusses three important parameters, namely porous media properties, the degree of subcooling, and different hydrate formation/dissociation methods, and how they individually affect the nucleation, growth and dissociation phases of CO_2 hydrates within porous media.

2.6.1 Impact of porous media

Hydrate kinetics cannot be assumed to be the same in bulk and in porous medium conditions. Porous media include a big number of parameters that are affecting the kinetic processes of hydrates. Characteristics such as, permeability, porosity, mineral composition, pore size distribution, wettability, roughness, and water saturation are not negligible. Porous media are characterized by big specific surface area which increases the interface between water and gas and thus nucleation sites are promoted (Yang et al., 2010). However, in cases where the sizes of the pores are too large, a similarity with the thermodynamic conditions of the bulk systems is observed (Kou et al., 2021). But, the smaller the size of the pores, the less the chance of forming hydrates caused by the impact of capillary forces in relation to the reduction of water activity (Wu et al., 2022).

The nucleation stage of hydrates is a stochastic process (Bai et al., 2015) entailing the difficulty in determining the exact duration of the nucleation and growth stages while forming hydrates, and because of that difficulty it is hard to acquire relevant statistical data (Talaghat & Khodaverdilo, 2019). It is in the nature of the porous media that the kinetics of hydrates are affected because of their physical and chemical characteristics. For example, the higher the wettability is the shorter the induction time and the faster the nucleation rate is (Natarajan et al., 1994), and the surface roughness enhances the nucleation sites (Wu et al., 2022). Various experiments were conducted investigating the relationship of the size of the pores and their distribution, with the kinetics of hydrates. Smith et al., (2002), presented that the hydrate equilibrium curve is shifted because of the change in phase conditions that is observed inside a porous medium with small-diameter pores. Uchida et al., (2002), as well, presented a similar result, where the porous medium with very small pore size (4nm) shifted the equilibrium curve -11.5C more in comparison with the porous medium that had bigger pores (100nm). The phase equilibrium of water/CO_2 systems in different porous media was investigated by Kang et al., (2008), by using three porous media with pore diameters of 6, 30, and 100 nm. Their results indicated that the smallest diameter pore size medium improved the CO_2 hydrate thermodynamic stability because capillary forces in small pores reduce the likelihood of hydrate dissociation triggered by local pressure drops or fluctuations, leading to a significant inhibition effect. On the contrary, the other two mediums were less affected by the inhibition effect. Experiments from Mekala et al., (2014), concerning the formation of CO_2 hydrate kinetics in presence of sea water and pure water in silica beds with three pore sizes, showed an overall lower CO_2 consumption and induction time while using sea water, but the smaller size silica bed showed an enhanced rate of hydrate formation in presence of pure water.

Sandstone and carbonate rocks pose as the two primary types of geological formations for storing CO_2, which are characterized by different mineral compositions that can influence the kinetics of CO_2 hydrate (Mohsin et al., 2024). Clay sediments in comparison with the sandy ones, have a vast specific surface area, small diameter particles, huge amount of trapped water, and increased capillary pressure (Nair et al., 2016). Research by Mu & Cui, (2019), on equilibrium conditions of hydrates inside bulk and clay sediment conditions indicated that varying salt concentrations had no important coupling effect with clay. Also, due to the fact that clays tend to absorb water, causing them to swell, the porosity in clay containing systems is reduced (Geng et al., 2021). This reduction in porosity leads to restricted flow of gas inside the reservoir which in turn inhibits the processes of formation and dissociation (Kumar et al., 2015).

2.6.2 Subcooling

The degree of subcooling directly impacts the kinetic rate of formation as one of the primary driving forces for hydrate nucleation and growth (Mali et al., 2018). In general, higher subcooling shortens induction time and enhances nucleation by providing greater thermodynamic force (Liu et al., 2022). However, inside porous media excessive subcooling can lead to rapid growth which can result in heterogeneous hydrate distribution and pore blockage within the medium. Conversely, low degree of subcooling may promote more uniform hydrate growth and at a slower rate (Oya et al., 2017). Additionally, the location where hydrates form inside the porous medium can depend on subcooling. Under high subcooling hydrates may form in bigger pores or at pore throats, rapidly sealing the pore structure. Under lower subcooling, growth may proceed more evenly, maintaining more open pathways longer (Mali et al., 2018).

As far as the dissociation of hydrates is concerned, subcooling prolongs the stability of the hydrates, resulting in a delay of dissociation (Rehman et al., 2022). A greater degree of subcooling corresponds to a longer period of stability before dissociation occurs. Reducing the temperature below the equilibrium temperature reduces the kinetic energy of hydrate molecules, slowing down the molecular motion and reducing the frequency of molecular collisions that are required for dissociation to take place. Consequently, the dissociation rate is slower in subcooled systems as it was reported from Tariq et al., (2022), during experiments in bulk conditions.

2.7 Identified Research Gaps

Inside the literature exist various experimental studies related to hydrates kinetics. The majority of them focuses on CH_4 hydrates, but during the recent years CO_2 hydrates have started to gain more interest mainly because of the need for developing effective CCS strategies that aim to mitigate greenhouse gas emissions. CO_2 hydrates are particularly relevant in subsurface storage applications because they can form under the high pressure and low temperature conditions that can potentially exist while CO_2 is injected inside the depleted gas reservoirs. The presence of hydrates causes pore blockages reducing the permeability of the reservoir and compromising injectivity. Despite the importance of understanding CO_2 hydrate behavior in these settings, the available experimental data remain limited and, in most cases, they do not fully represent the complex conditions that exist in actual reservoir environments since the majority of the conducted studies are under bulk conditions. This study focuses on CO_2 hydrate kinetics specifically in the context of CCS in depleted gas reservoirs, with a more focus on the process of dissociation for which the available data are even more limited.

Although a number of studies have examined CO_2 hydrate formation and dissociation, most experimental procedures rely on simplified setups or systems – such as sand packs, silica beds and clay suspensions – and emphasize mainly on the process of hydrate formation. Only a few attempts have been made to replicate actual reservoir-like environments, and even less have incorporated advanced imaging techniques to observe pore-scale phenomena. As a result, the understanding of how CO_2 hydrates form and grow within true reservoir porous structures, particularly under dynamic injection scenarios, remains incomplete, even more under different hydrate forming methods and subcooling temperatures. More critically, the CO_2 hydrate kinetic

during the process of dissociation remains underexplored. This process plays a major role in maintaining injectivity during CCS projects, yet most studies either overlook dissociation or investigate it under oversimplified conditions. There is a lack of systematic investigation into how variables like subcooling, and different thermal stimulation methods influence the rate and mechanisms of dissociation.

This literature review has provided a short overview of the kinetic processes included in CO_2 hydrate formation and dissociation, with more focus on the effect of porous media on these processes. The chapter highlighted different studies across various applications that give valuable information which are related to the topic of this Master Thesis, and outlined some knowledge about the kinetics of CO_2 hydrates with exclusive interest in CCS projects in depleted gas reservoirs and the negative impact that the presence of CO_2 hydrates induces. So, by considering all the above information this Master's Thesis aims to provide additional knowledge regarding the kinetics of CO_2 hydrates formation and dissociation by examining three different methods of forming and dissociating hydrates together with the effect of subcooling as a driving force on these two processes. The following chapter will thoroughly go through the experimental procedure that was followed for the purpose of addressing the above aim via reservoir-like experiments in combination with CT imaging data.

Chapter 3: Methodology

Building upon the findings from the literature review and the knowledge gaps that were identified previously related to CO_2 hydrates, this chapter aims to outline the experimental approach that was used for the investigation of the kinetics regarding the processes of formation and dissociation of CO_2 hydrates inside porous media. From the literature review it was highlighted the significance of understanding hydrate behavior under reservoir-like conditions, and the need for more experimental procedures that include real-time monitoring of hydrate behavior inside the porous medium. In order to address these challenges, a combination of core-flooding experiments and advanced imaging techniques, such as computed tomography (CT), were utilized. Such methodologies allow for non-invasive observations of hydrate distribution and spatial evolution within porous media. The experimental plan that was followed included the use of two setups, one fixed and one portable designed in such a way that it can be placed inside a medical CT-scanner. The experimental procedures aimed to simulate conditions that are expected inside depleted gas reservoirs, making sure as accurate as possible replications of temperature, pressure, and brine saturation conditions inside a core-shaped sandstone porous medium. Additionally, the process of data acquisition and their analysis are used for the quantification of the brine/hydrate saturation and permeability alterations, in order to investigate how the hydrate kinetics regarding both the formation and dissociation are affected by using different hydrate forming and dissociating methods, and different degrees of subcooling. At the beginning of this chapter an overview of the experimental setups is presented, followed by detailed descriptions of the apparatus design, materials, and procedures. In addition, methodological adjustments made to enhance data quality, are discussed, leading to the final section where the data processing and computational methods are thoroughly described.

3.1 Overview of Experimental Approach

Given the complexity of CO_2 hydrate behavior inside porous media and more specifically under depleted gas reservoir-like conditions, several core-flooding experiments were conducted, where CO_2 was constantly injected into the sandstone core with known porosity and permeability. For the completion of the experiments two core-flood setups were used. They are almost identical except from their cooling system which differs. The one setup used a refrigerator while the other one implemented a circulator that was connected to two cooling jackets that were placed around the core holder. Thermal stimulation is the method that was used to induce hydrate formation or dissociation by controlling the temperature of the system. Even more, the latter setup was designed accordingly in order to fit under a medical CT-scanner, which allowed for better visualization of hydrate distribution within the porous core sample, and thus the gathering of more data that are pretty useful for the quantification of many parameters that give insight on the kinetics of CO_2 hydrates during both the formation and the dissociation process. Finally, apart from the temperature, all other parameters such as porous medium, pressure, salinity and brine saturation where fixed in order to exclude their influence on the experimental results.

3.1.1 Purpose

As already mentioned in the previous chapter, the formation and dissociation of CO_2 hydrates inside porous media is a more complicated process when compared with bulk conditions, because these two processes are influenced by multiple factors that are related to the characteristics of porous media, such as mineralogy, porosity and permeability. So, it is important to try and include as many of these parameters is possible during the experimental procedure so that the results are more applicable to reality. More specifically, more accurate measurements can be obtained regarding the growth and nucleation of hydrates since these types of experiments provide a controlled environment for studying these kinetic behaviors.

The integration of computed tomography (CT) in the majority of the conducted experiments is important for monitoring CO_2 hydrate formation and dissociation process inside the porous medium. CT imaging offers a unique perspective on hydrate distribution on the pore-scale level by enabling a high-resolution, non-invasive observation throughout different stages of the experiments. A technique like this allows for tracking changes in saturation profiles, and locate areas inside the porous core sample where the hydrates have formed. By capturing three-dimensional images at different time intervals, CT gives the advantage of acquiring valuable data on hydrate formation and dissociation which would be difficult to measure with traditional experimental procedures.

Computed tomography (CT) scanning is an imaging technique which uses X-ray beams in order to create cross-sectional images of an object. CT-scanners consist of an X-ray source and a detector that rotate around the measured object, capturing numerous projections from different angles. Afterwards, all the acquired images undergo processing with the help of reconstruction algorithms in order to create detailed two-dimensional images of the internal structure of the sample (Goldman, 2007). More specifically, about CO_2 hydrates, the use of CT-scanning allows for determination of the hydrate formation through saturation difference between CT images, but the phase transition from liquid water to gas hydrates is not possible. However, the density of water and hydrate is slightly different but because the resolution of the CT scanner is too low to zoom inside the pore space of the core it is difficult to distinguish the two phases. Thus, a combination of core-flooding and CT-imaging can provide a comprehensive methodological approach for observing and analyzing CO_2 hydrate kinetics, by offering valuable data for improving reservoir management and storage efficiency.

3.2 Experimental Section

3.2.1 Experimental Material

3.2.1.1 Material

The N_2 and CO_2 cylinders that were used during this experimental work had a certified purity of 99.999% and 99.7% respectively. They were provided by the Linde Co. gas supplier. The NaCl salt used for the making of the brine solution was certified 99.5-grade and was obtained from the Fisher Scientific. Deionized distilled water was used for the preparation of saline solution in all the

conducted experiments. The porous medium used for this study was the Bentheimer Sandstone (91.6% quartz, 2.5% kaolinite, 5% K-feldspar, and 0.9% other minerals) in the form of a core plugs (Figure 5). The core plugs had dimensions of 17 cm in length, and 3.8 cm in diameter. This kind of porous medium is characterized as a high permeable one with permeability values ranging from 1.5 to 2.5 D, and porosity of 0.23 to 0.25. In general, Bentheimer sandstone are ideal for laboratory studies because of their lateral continuity and homogenous nature (Peksa et al., 2015). The preparation of the cores before they are used, requires their coating with a 5 mm thick layer of epoxy resin in order to provide protection layer.

Figure 5: Pictures of a Bentheimer core sample that was used during the experimental work of this thesis. The core sample is surrounded by a grey colored glue.

3.2.1.2 Setup description

Even though there were two setups used for the experimental work of this Master Thesis, their design is practically the same apart from their temperature regulating system. So, in both of them three different sections can be identified, namely, the inlet section, the central section, and the outlet section. The figures provided below (Figure 6 and Figure 7) provide the schematic representation of the two setups:

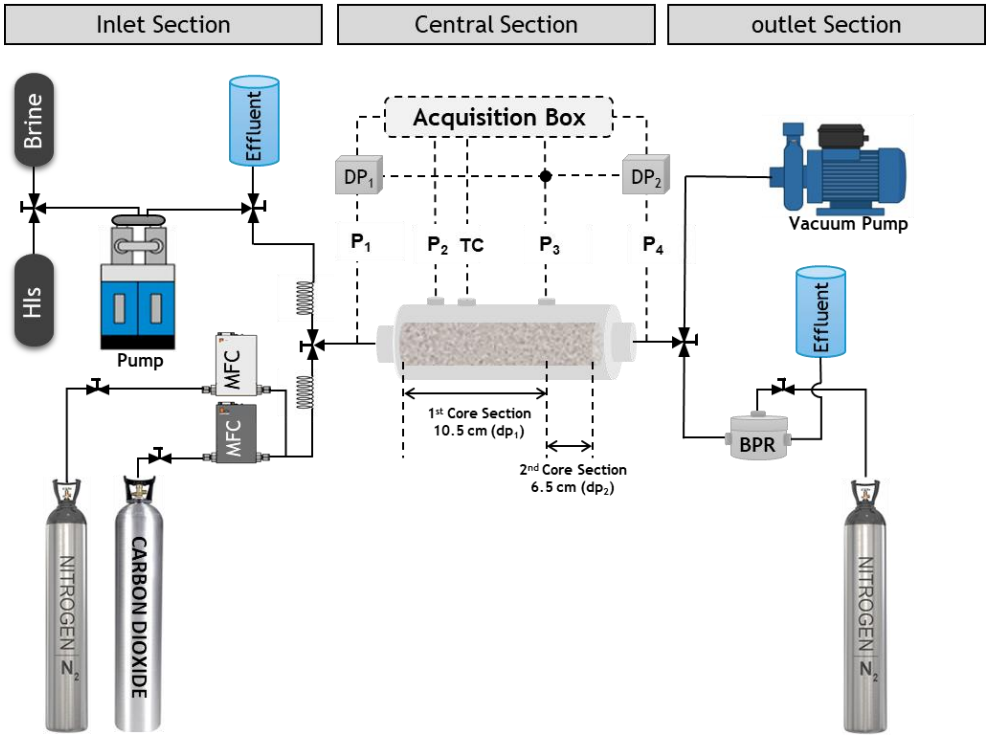

Figure 6: Graphical representation of the experimental apparatus of the fixed setup. The system consists of three sections: an inlet section supplying water/brine solution through the Vindum pump, and the gases (CO_2 or N_2) through the mass flow controllers (MFC); a central section that includes the core holder which is placed inside the refrigerator, equipped with four pressure transducers ($P_1 – P_4$), thermocouple (TC), and the differential pressure gauges (DP_1, DP_2) all monitored by an acquisition box; and an outlet section that contains the back pressure regulator (BPR), the vacuum pump, and the effluent.

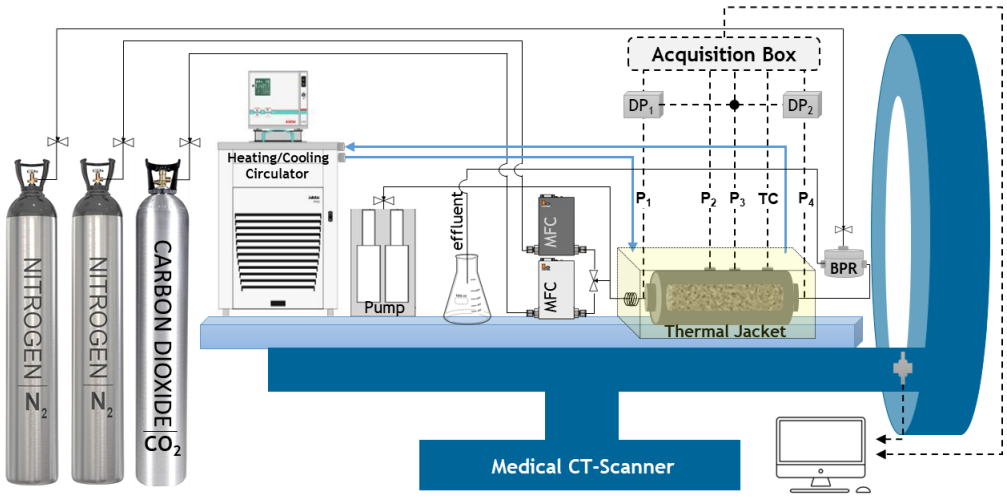

Figure 7: Graphical representation of the experimental apparatus of the portable setup used under the medical CT scanner. The setup consists of the cylinders of the gases (N_2 or CO_2) that are connected to the mass flow controllers (MFC). It also includes the thermal circulator which is connected to the thermal jacket that is around the core holder. Next to the circulator the Quizix pump can be found which is responsible for the water/brine solution injection into the core. The data acquisition section follows, and consists of four pressure transducers ($P_1 – P_4$), the thermocouple (TC), and the differential pressure gauges (DP1, DP2). The outlet of the core holder is connected to the back pressure regulator (BPR) and the effluent. Lastly, the core holder is positioned within a medical CT scanner.

The inlet section involves the fluids that are injected into the system (N_2, brine, CO_2, and water) together with the pumps that allow their injection. For the brine and water injection into the system the Vindum pump is used in the fixed setup (Figure 9), whereas the Quizix pump is used for the portable one (Figure 8). Both pumps consisted of two pistons and are characterized as pulse-free and high precision pumps. As for the N_2 and CO_2 a high-pressure gas mass flow controller for each one is employed in order to control the injection rate of gas flowrate.

The central section consists of the core holder and the data recording equipment that is attached to it (pressure sensors and thermocouples). More specifically, four pressure transducers are used to capture the pressure changes at the inlet, 2.25cm away from the inlet, 6.5cm away from the outlet, and at the outlet of the core holder. Additionally, two differential pressure sensors are used to capture more precisely any pressure differences happening in the two sections of the core that have as an imaginary boundary the location where the third pressure transducer is located. As for the temperature recordings, two thermocouples are used, which are placed inside the core and at the outlet of the core. On the fixed setup, the core holder is located inside the refrigerator (GRAM, BioCompact II 210) that is responsible for the temperature regulation (Figure 9). On the portable setup the core holder is surrounded by two aluminum cooling jackets that are attached to the circulator (LAUDA Proline RP845) which is responsible to control the temperature of the core by circulating the cooling medium of a water and MEG mixture in a 0.5:0.5 ratio.

Lastly, the outlet section includes the outlet valve, whose role is to connect the outlet of the core with the back pressure. In order to control the pressure of the system to the desired value, a high-pressure regulator is used which is referred to as the back pressure system. It is connected to the outlet of the core holder, and it is adjusted with a N_2 cylinder to sustain the experimental pressure (30 bar). The valve connecting the back pressure system with the core holder, also connects the line that ends up to the adsorbent-equipped vessel in which the effluent solution is accumulated.

For the portable experimental setup, a medical CT-scan is equipped (Figure 8) and more specifically the Siemens Somatom Volume, an instrument known for its high-resolution imaging capabilities. Its core advantages are the allowance for internal examination of the core sample without altering it or damaging it and preserving its integrity for further analysis, the rapid acquisition of data, since it can quickly capture images that enable the monitoring of dynamic processes, and the detailed cross-sectional images that allow for precise visualization of the internals of the core. In fact, it is used for the computation of fluid saturation and hydrate volume during the processes of formation and dissociation of CO_2 hydrates, which is achieved by using a slice thickness of 0.6 mm for every scan together with a resolution of 0.2 mm for the other two dimensions which results in a voxel size of 0.2 x 0.2 x 0.6 mm^3. As a final mention, a current of 250 mA and a voltage of 140 kV is used.

Figure 8: Picture of the portable experimental setup (CT setup).

Figure 9: Pictures of the some of the parts that consist the fixed setup. On the top left are the differential pressure gauges (dP). Next to them is a picture of the core placed inside of the core holder. On the bottom left is a picture of the core holder placed inside the refrigerator. Lastly, on the bottom right there is a picture of the Vindum pump.

3.2.2 Experimental Procedure

The experimental procedure that was designed to investigate the kinetics of CO_2 hydrates inside porous media under controlled conditions. Apart from the temperature all other parameters such as pressure, porous medium, brine salinity, and brine saturation inside the core were fixed, in order to observe the effect of temperature on both the formation and dissociation processes. Each experiment followed a structured sequence to ensure repeatability and consistency, though the temperature change for the formation and the dissociation differed almost every time. Below, a step-by-step outline of the experimental process is presented.

Before the beginning of each experiment a number of things needed to be checked in order to reduce the risk of encountering any possible issues while the experiment was running. Namely, the brine solution (1wt% NaCl) had to be prepared and degassed to remove any dissolved air, the differential pressure gauges (dPs) had to be checked of working correctly and bled to remove any trapped gas. In addition, the pressure and temperature sensors set to zero in the absence of flow, and the back pressure membrane is replaced.

After that, a leak test was performed in order to make sure that the system was leak-free and thus the pressure inside the core would remain stable throughout the experiment. Simultaneously with the leak test, gas permeability tests are performed in order to the permeability of the core sample at dry condition.

After confirming that the system is leak free and the pressure is stable at 30 bar, the dry core is subjected to a CT scan at room temperature while N_2 is flowing through it and while CO_2 is flowing through it in order to examine the CT intensity affection by the presence of the two different gases. Even more, the temperature effect on the intensity of the CT images while CO_2 was present was also examined by subjecting the dry core at various scans that corresponded to the temperatures of the temperature steps that would be followed in each experiment.

Then the process of the core saturation is followed. The desired bine saturation is achieved in all the experiments with the help of a modified brine/N_2 co-injection technique. The N_2 and brine solution with specific flow fraction (gas/liquid >99.98) are co-injected into the system. The solution needs to be distributed uniformly as possible throughout the core, which is why the co-injection process lasts a few days and is sometimes followed by the N_2 injection after the brine injection stopped. Finally, when the brine is distributed uniformly, the remaining brine located inside the injection line had to be retracted.

After the end of the saturation process, the cooling of the system can be initiated, according to the pressure – temperature (P-T) phase diagram in specific brine solution by setting the circulator or refrigerator to the desired temperature for hydrate formation. The desired temperature is reached with three different methods throughout the experimental procedure, namely, the isothermal where the temperature is decreased directly, the step cooling where the temperature is decreased in a number of steps with the same interval, and the ramp cooling where the temperature is decreased with a slow rate (in this case 0.1 ^{o}C/h). As soon as the temperature of the system is reached to the desired temperature and become stable based on the selected cooling method, the CO_2 injection protocol is followed, during which the CO_2 is injected into the system with a steady flowrate of 5 g/h. In isothermal and constant cooling (ramping) techniques

the cooling of the system continues until hydrates form, while in the step cooling sufficient time allocated for each step to reach steady state in terms of pressure and temperature. Once the maximum growth is achieved at the end of each cooling procedure (pressure reaches a steady state), the CO_2 injection is continued and kept constant.

After reaching steady state due to the maximum CO_2 hydrates saturation, the dissociation process begins by increasing the temperature of the system with either setting the temperature to the target value in isothermal and constant heating (ramping) techniques or use a specific interval for the step heating method while continuing the CO_2 injection until the end of the experiment. The end of a hydrate formation and dissociation cycle is reached by reaching a temperature equal to approximately 20C and maintaining this temperature for more than 24h to ensure complete hydrate dissociation. Hydrate formation and dissociation were repeated for two cycles in some cases, not only to investigate the impact of water memory on hydrate formation but also to ensure the repeatability of the tests.

After the complete last dissociation of hydrates, a brine permeability test is preformed to observe how the porous medium was affected by the experimental cycle of hydrate formation and dissociation. During this stage the core had to be completely filled with brine (100% saturation). In order to achieve complete brine saturation, the vacuum saturation technique was applied by using a vacuum pump.

Eventually, after all the aforementioned procedures the experiment is almost finished and the following steps are taken in order for it be completely finished. More specifically, the system had to be completely depressurized and the brine solution pump together with the core had to be cleaned from any remaining brine by injecting tap water into them. Then the core would be dried as much as possible by injecting N_2 into it, before the core is taken to the vacuum oven to dry completely and be ready to be reused.

3.2.3 Challenges Encountered

Even though the experimental procedure was completed successfully, some challenges arose that impacted the accuracy and consistency of the study. For instance, an issue that was encountered several times was the freezing or blocking of the tubes from which the brine solution was running through. This issue was observed mainly in the fixed setup because many tubes were located inside the refrigerator and the low temperatures that occurred caused any remaining solution, which may have not been retracted successfully, to freeze or cause blockage because of hydrate formation. These blockages inside the lines did not allow accurate and reliable pressure and/or temperature recordings and in such cases the experiments had to be terminated and repeated.

Another significant problem was the ability to maintain a stable and reliable pressure throughout the entire span of each experiment mainly because of the fact that the system was under dynamic conditions with CO_2 flowing constantly and also because of the influence of the back pressure which caused a few times some small temperature increases or drops because of false regulation or because of a membrane swelling located inside the back pressure cell. Such fluctuations can affect both the pressure transducer and differential pressure measurements.

3.3 Methodological Adjustments

Throughout the course of the experimental work of this study, several methodological adjustments were made to improve data accuracy, and ensure that the results accurately reflect the kinetics of CO_2 hydrate formation under reservoir-like conditions. The adjustments mainly focused on modifications made regarding the experimental procedure, and more precisely changes in the method of forming and dissociating the hydrates. In the previous section, the isothermal method of cooling is described for forming hydrates, where the temperature is directly reduced to the target temperature according to the degree of subcooling that needs to be examined. In the first three experiments this method was employed to examine three different degrees of subcooling (4 °C, 6 °C, and 10 °C). But, the method of forming hydrates changed for the rest of the experiments in order to examine how cooling/heating technique could affect the kinetics of CO_2 hydrates.

Table 1: The following table summarizes all the experimental conditions that were employed during the experimental work of this study. More specifically, the cooling/heating method. The subcooling, and the cooling/heating step interval of every experiment are listed below.

Experiment	Cooling Method	Cooling Steps Interval	Heating Method	Heating Steps Interval	Subcooling [°C]
First Experiment	Direct Cooling	-	Step Heating	1.5 °C	6
Second Experiment	Direct Cooling	-	Step Heating	1.5 °C	4
Third Experiment	Direct Cooling	-	Step Heating	1.5 °C	10
Fourth Experiment	Step Cooling	3.5 °C	Step Heating	1.5 °C	4.5
Fifth Experiment - First Cycle	Step Cooling	2 °C	Step Heating	2 °C	4.5
Fifth Experiment - Second Cycle	Direct Cooling	-	Step Heating	2 °C	4.5
Sixth Experiment - First Cycle	Ramp Cooling	0.1 °C/h	Ramp Heating	0.1 °C/h	4.5
Sixth Experiment - Second Cycle	Direct Cooling	-	Ramp Heating	0.1 °C/h	4.5

3.3.1 Experiments 1 and 2

In fact, during the first experiment the hydrate forming temperature was 1 °C (6 °C subcooling), and the method was the direct cooling of the core to this temperature. For the dissociation afterwards the step heating method was followed, by increasing the temperature to 11.5 °C in steps with an interval of 1.5 °C, and then going directly to 20 °C to ensure complete hydrate dissociation. For the second experiment the plan was to form hydrates with the same method but a 3 °C (4 °C subcooling), in order to see the effect of lower degree of subcooling. Again, for the dissociation method exactly the same procedure was followed as in the first experiment (step

heating with 1.5 °C interval until 11.5 °C before going directly to 20 °C). Both of these experiments were conducted under the fixed setup, and the duration of each step during the dissociation process was aimed to be around 24 hours, but there was one step in each experiment that lasted more than that because of the weekend that was in-between. All the cooling and heating steps of both experiments, that are described, are presented in Figure 10.

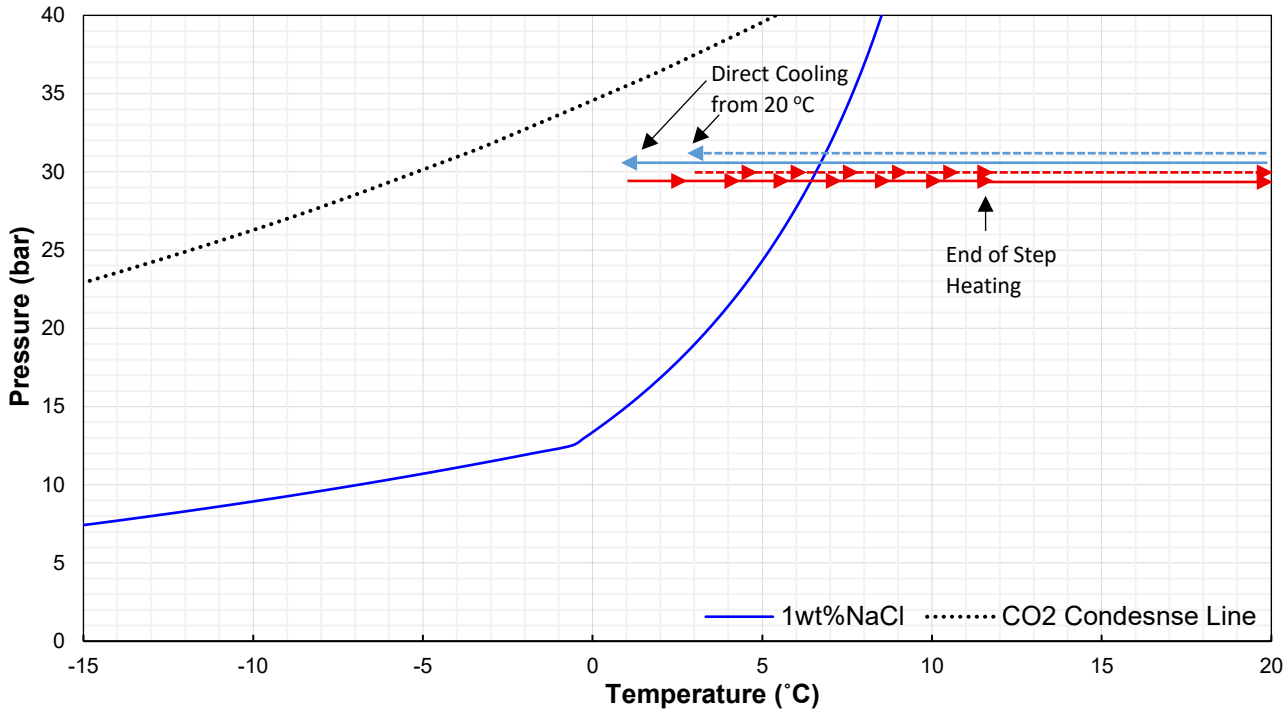

Figure 10: Pressure and Temperature phase diagram of CO_2. The hydrate stability zone is defined by the CO_2 condensed line (black-dashed) and the equilibrium line that corresponds to 1wt% NaCl brine solution (blue line). The continuous arrows indicate the temperature steps of the 1st experiment whereas the dashed arrows indicate the temperature steps of the 2nd experiment.

3.3.2 Experiment 3

For the third experiment the direct cooling method for forming hydrates was used but the cooling temperature this time was -3 °C (10 °C subcooling), a higher degree of subcooling. This test was performed under the medical CT scanner. Step heating with the same interval of 1.5 °C between each step was used for hydrate dissociation was used for hydrate dissociation (Figure 11), but the duration of the steps was different. More specifically, the plan was to change the temperature 3 times within a day. Basically, once the temperature became stable, the temperature was increased to the next step. The final step of each day lasted longer because the working hours of the day were over and thus the next temperature change had to be done at the morning of the next day. About the CT scans that were taken during this experiment, the first was after the process of brine saturation ended. Five more were taken during the process of hydrate formation, and then one scan was taken at the end of each dissociation step.

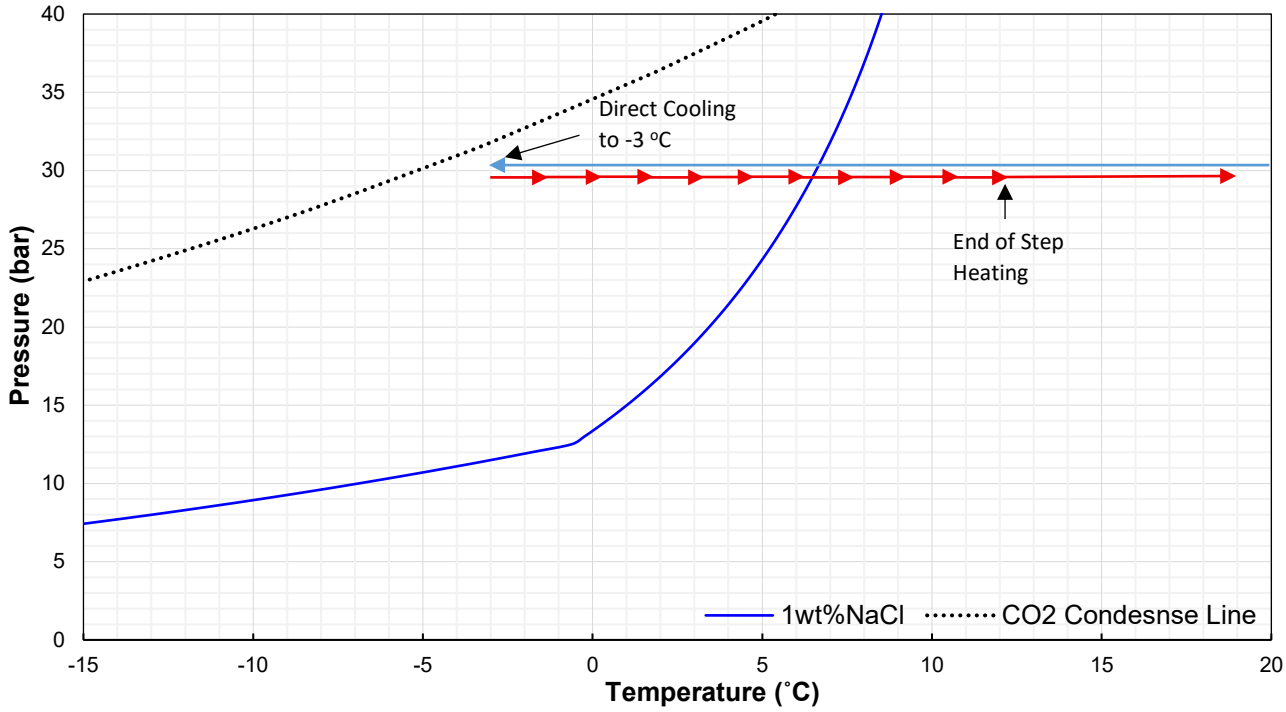

Figure 11: Pressure and Temperature phase diagram of CO_2. The hydrate stability zone is defined by the CO_2 condensed line (black-dashed) and the equilibrium line that corresponds to 1wt% NaCl brine solution (blue line). The blue arrow indicates the cooling step, while the red arrows show the heating steps.

3.3.3 Experiment 4

The fourth experiment was conducted under the medical CT scanner. The plan for this experiment was to investigate the impact of a different hydrate formation/dissociation method on the kinetics of hydrates. In this experiment the method of forming hydrates is not the isothermal one which was applied in all previous experiments, but the method of step cooling during which the temperature of the system is reduced in steps. More specifically, the temperature interval was 3.5 ºC. The initial goal was to reach a lowest temperature of -1 ºC in order to reach 8 ºC of subcooling since the 4 ºC, 6 ºC, and 10 ºC of subcooling temperatures were reached in the previous experiments. The system was to stay at each temperature step for 24h, and considering the available time of the CT-scan setup, the initial temperature was 9.5 ºC, a temperature quite far from the hydrate formation zone temperature (7 ºC). But, at the end of the third cooling step (2.5 ºC) hydrates formed and thus there was no reason for reducing the temperature further downwards to reach -1 ºC, since the pressure drop and the temperature increase were observed at that temperature. Even more, the CT images that were taken afterwards did not show any significant increase of the core's saturation after remaining at that temperature for 24h. For the dissociation process the method used was the same as all previous experiments, namely the step heating method. The temperature interval used again was 1.5 ºC, so dissociation started at 2.5 ºC and implemented 5 steps until the temperature of 10 ºC before going directly to 20 ºC. The interval had to be the same in order for easier comparison with the other experiments, as illustrated in Figure 12. A scan was taken at the end of each step at both the formation and the dissociation

processes, but this time a permeability test was carried out just before each scan in order to obtain more data which can be used for the calculation of hydrate saturation changes at each step of the experiment.

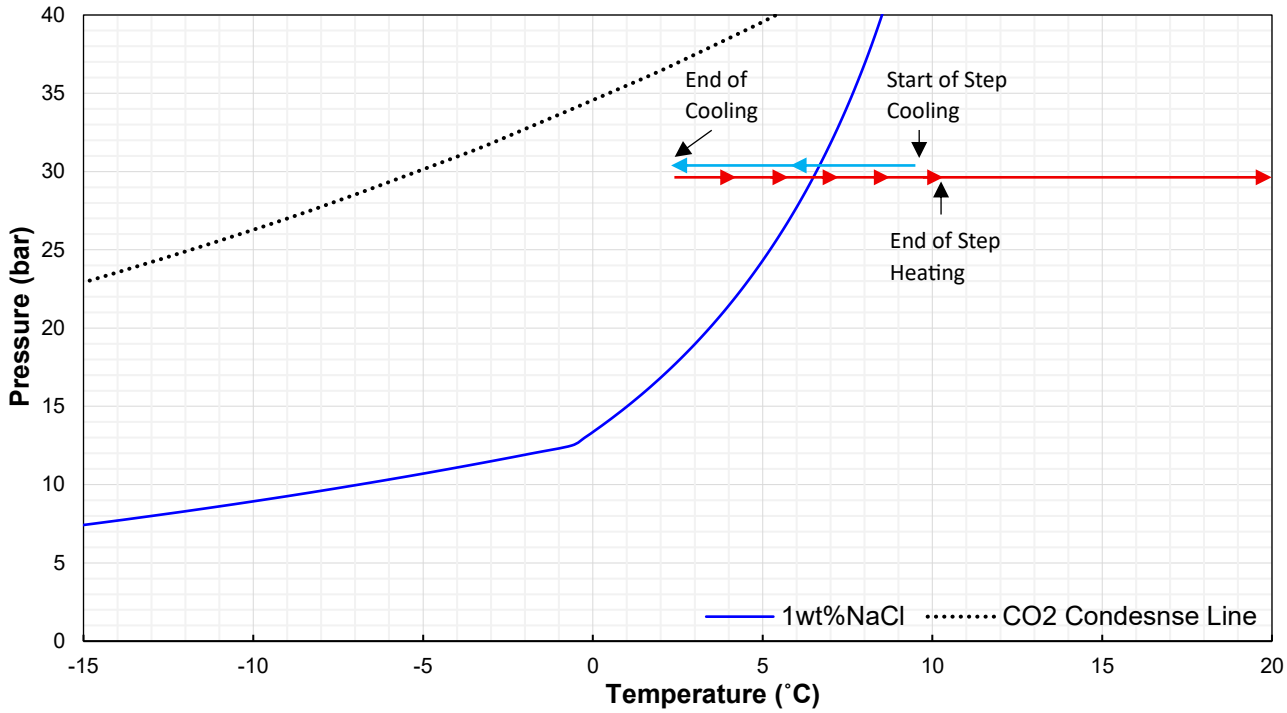

Figure 12: Pressure and Temperature phase diagram of CO_2. The hydrate stability zone is defined by the CO_2 condensed line (black-dashed) and the equilibrium line that corresponds to 1wt% NaCl brine solution (blue line). The blue arrows indicate the cooling steps, while the red arrows show the heating steps.

3.3.4 Experiment 5

The fifth core-flood experiment was conducted under the CT-scan. The plan for this experiment was to reach the same lowest temperature as the first step cooling experiment, namely 2.5 °C, with the method of reducing the temperature in steps again, but with a different interval. This time the interval was smaller and it was 2 °C, starting from 12.5 °C and reaching to 2.5 °C. This time the initial temperature was higher because there was a need to assess whether the sudden jump in brine saturation along with drop in permeability during the experiments at temperatures above the corresponding equilibrium temperature was due to hydrate formation or CO_2 dissolution. More specifically, we wanted to examine if the porous medium promotes hydrate formation. Also, there was a need of evaluate the effect of smaller step in temperature (smaller driving force) in hydrates formation/dissociation. Even more, the dissociation/heating steps were changed this time also with an interval of 2 °C, in order to see the effect of a higher driving force than before in dissociation. For easier comparison a second cycle was performed, by cooling the system directly to 2.5 °C and then using the 2 °C interval heating steps for the dissociation of hydrates. The duration of the first two steps during the formation process of the first cycle were different. In fact, the first cooling step lasted for 4 days and the second one lasted for three days,

in order to make sure that there is no possibility that hydrate formation could occur at temperature higher than the equilibrium temperature. This time scans together with permeability tests were performed at the beginning and at the end of each formation or dissociation step, to acquire more information on the hydrate formation and dissociation processes. During this experiment a second cycle was also performed, during which the isothermal method was used in order to reduce the temperature to 2.5 °C directly in order to form hydrates. Then the same dissociation method was performed as in the first cycle (i.e. step heating with 1.5 °C interval). Both cycles are included in Figure 13.

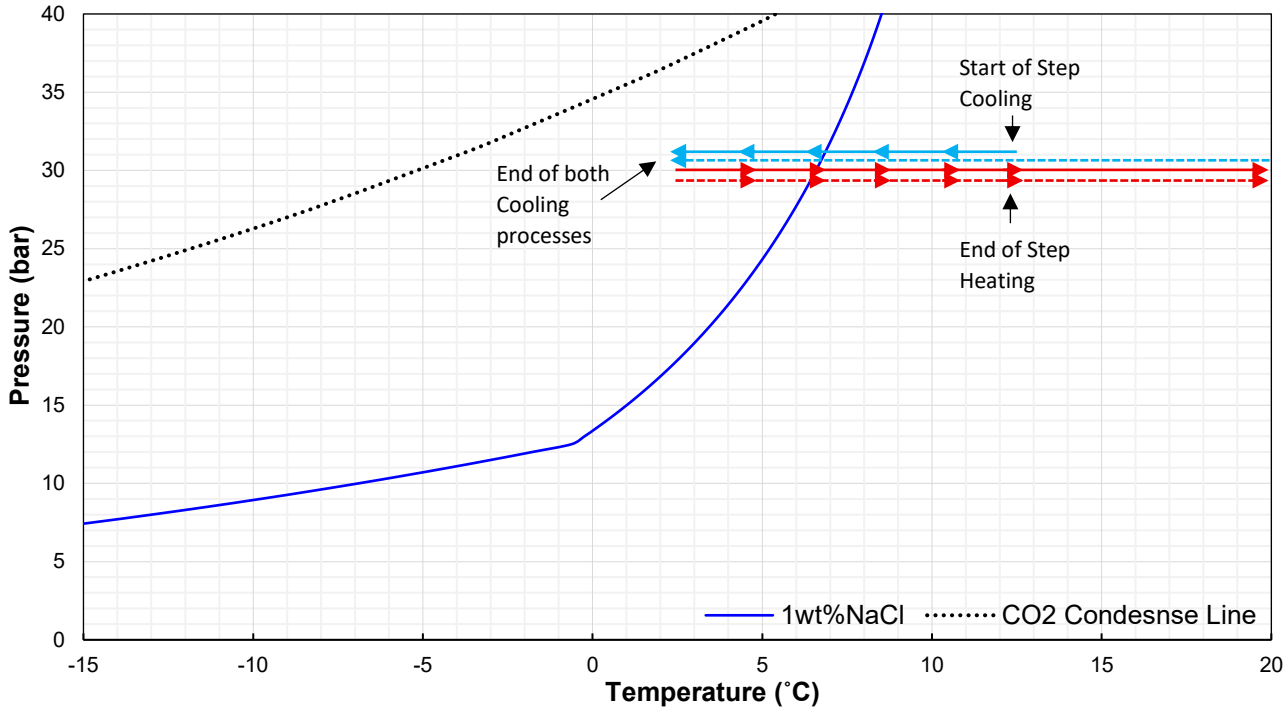

Figure 13: Pressure and Temperature phase diagram of CO_2. The hydrate stability zone is defined by the CO_2 condensed line (black-dashed) and the equilibrium line that corresponds to 1wt% NaCl brine solution (blue line). The continuous arrows show the temperature steps of the first cycle, while the dashed arrows show the temperature steps of the second cycle.

3.3.5 Experiment 6

Finally, the last and sixth experiment was also performed under the medical CT scanner. The plan for this experiment was to reach again the same lowest temperature of 2.5 °C, with a different method this time. The method was the ramp cooling method, by reducing the temperature of the system with a rate of 0.1 °C/h having as a starting point the temperature of 12.5 °C. This different method is examined because with this very small rate of cooling, the driving force that is induced is even smaller than that of the step cooling process. Thus, the goal was to examine how an even smaller driving force or subcooling can affect both the formation and dissociation of hydrates. About the dissociation process the same rate of temperature change (0.1 °C/h) is applied in order to see how the process of dissociation is affected and also be able to see more clearly when the

massive dissociation of hydrates occur. For comparison reasons, a second cycle follows the ramp cooling cycle, during which the isothermal method of forming hydrates is followed (direct cooling) to the same temperature of 2.5 °C. Then the method of dissociation is the same as in the first cycle of this experiment (0.1 °C/h heating) in order to observe any possible differences during the dissociation process while having formed hydrates with two different methods (effect of 2 different driving forces). Even more, during the second cycle, after the formation of hydrates the temperature remained the same for 4 days in order to observe the kinetics of the hydrate formation and growth process before starting dissociating. Since there were no steps during this experiment, the scans and the permeability tests took place twice a day during the first cycle. For the second cycle, multiple scans a day starting from a scan every 2 hours during the first 3 days and then reducing this number to 3 scans per day and eventually 2 scans at the day before starting the dissociation process, in order to observe better the growth process of the hydrates. As for the dissociation process twice a day a scan together with a permeability test were taken.

3.4 Data Processing and Calculations

3.4.1 Pressure and Temperature Data

The pressure and temperature were monitored continuously throughout the experiments with the help of the four pressure transducers, the differential pressure gauges and the thermocouple, positioned along the core holder. The differential pressure gauges had an accuracy of ± 300 mbar, allowing for reliable detection of small changes. The identification of these small changes was very useful particularly during the gas permeability tests, because they allowed for calculating any permeability changes during different stages of the experiments as will be explained in the next subsection. Additionally, via the pressure and temperature recordings, plots of pressure and temperature versus time and dimensionless time (expressed as injected pore volumes) were generated to visualize the dynamics of hydrate formation and dissociation, and enabled the identification of hydrate-related pressure buildups, pressure drops, and temperature spikes.

3.4.2 Permeability Calculation

The permeability of the core samples was measured through permeability tests, either in presence of gas (N_2 or CO_2) or brine, depending on the stage of the experiment that the permeability test was performed. All permeability tests involved the systematic altering of the gas or brine injection rate, and the recording of the corresponding pressure difference that was recorded from the differential pressure gauges (dP). More specifically, the dP1 captures the pressure difference occurring in the first section of the core with 10.5 cm length, whereas the dP2 records the pressure difference at the second section of the core with 6.5 cm length. The determination of permeability (K) while brine is present is achieved via the use of Darcy's Law (Lage, 1998), in a rearranged form according to Equation 1:

$$\frac{q}{A} = -K\frac{\Delta P}{\mu L} \tag{4}$$

where, q [m3/s] is the flow rate, A [m2] is the cross-sectional area of the core, ΔP [Pa] is the pressure difference along the core length section L [m], and μ [Pa·s] is the viscosity of the fluid that runs through the core. By plotting the $\frac{q}{A}$ on the y axis vs the $\frac{\Delta P}{\mu L}$ on the x axis the permeability is determined as the slope of the linear trend line of the plotted data points. Though, when the permeability tests were performed in presence of a gas (N_2 or CO_2), the Klinkenberg correction had to be used for the determination of permeability as can be seen in equation 2:

$$K_{app} = K\left(1 + \frac{b}{P_{mean}}\right) \tag{5}$$

where, K_{app} [D] is the apparent or effective permeability, K [D] is the Klinkenberg-corrected permeability, b [-] is the Klinkenberg coefficient and P_{mean} [bar] is the mean pore pressure (Sander et al., 2017). By combining equations 1 and 2 the Klinkenberg correction is incorporated into the Darcy Law providing the following equation:

$$\frac{q}{A} = -\frac{K}{\mu}\left(1 + \frac{b}{P_{mean}}\right)\frac{\Delta P}{L} \tag{6}$$

The Klinkenberg coefficient (b) is determined with the help of a graph in which the apparent permeability is plotted against the inverse of the average pressure after various gas permeability tests at different pressure conditions ($1/P_{mean}$), and a linear regression is applied. The slope of the resulting line corresponds to k · b, and the intercept gives K. From the aforementioned values the slip factor b is extracted.

3.4.3 CT image analysis

The data acquired from the medical CT scanner include CT images that were taken at various stages of each experiment and their use was the determination of water or water + hydrate saturation, namely saturation changes and profiles inside the core samples. The software that was used for the analysis of the CT images was ImageJ, through which the images were cropped and their color balance was adjusted in order for more accurate and precise analysis. The analysis was done initially qualitatively by comparing the processed images visually and observing any differences between them, and subsequently quantitatively by exporting the z axis profile of the mean Hounsfield units of each image along the core length at an excel sheet and calculating the amount of saturation inside the core.

The saturation inside the core is estimated by obtaining CT images of the core under fully brine-saturated (CT_{wet}) and dry (CT_{dry}) conditions, together with the scan of the experimental stage of interest (CT_{exp}), whether it is during the brine saturation process, the hydrate formation process, or the hydrate dissociation process. In fact, the mean value of the Hounsfield units obtained from the z axis profile of each scan is used for this calculation with the help of Equation 2:

$$S_{w+H} = \frac{CT_{exp} - CT_{dry}}{CT_{wet} - CT_{dry}} \tag{7}$$

3.4.4 Hydrate Properties Calculations

The acquisition of the saturation ($S_{w/H}$) and permeability (K) change at every step of each experiment are crucial for the calculation of various hydrate properties including hydrate saturation. Hydrate volume, hydrate density, CO_2 consumption or release, and water to hydrate conversion.

At first, the permeability difference (ΔK) of each step is calculated by subtracting the permeability of the previous step from the permeability value of the step of interest:

$$\Delta K = K_i - K_{i-1} \tag{8}$$

The way the permeability is calculated assumes a linear relationship of the permeability change during each step of formation and dissociation in every experiment, and because of that the normalized permeability at each step is plotted versus the percentage of hydrate saturation. The data points are then compared with empirical permeability models which are provided in Figure 14, and they are fitted to the model that they are closer to. By fitting the data points into an empirical model, new hydrate saturation values obtained, which are the corrected values. These corrected values are then used to back-calculate all other properties, in order to be corrected as well.

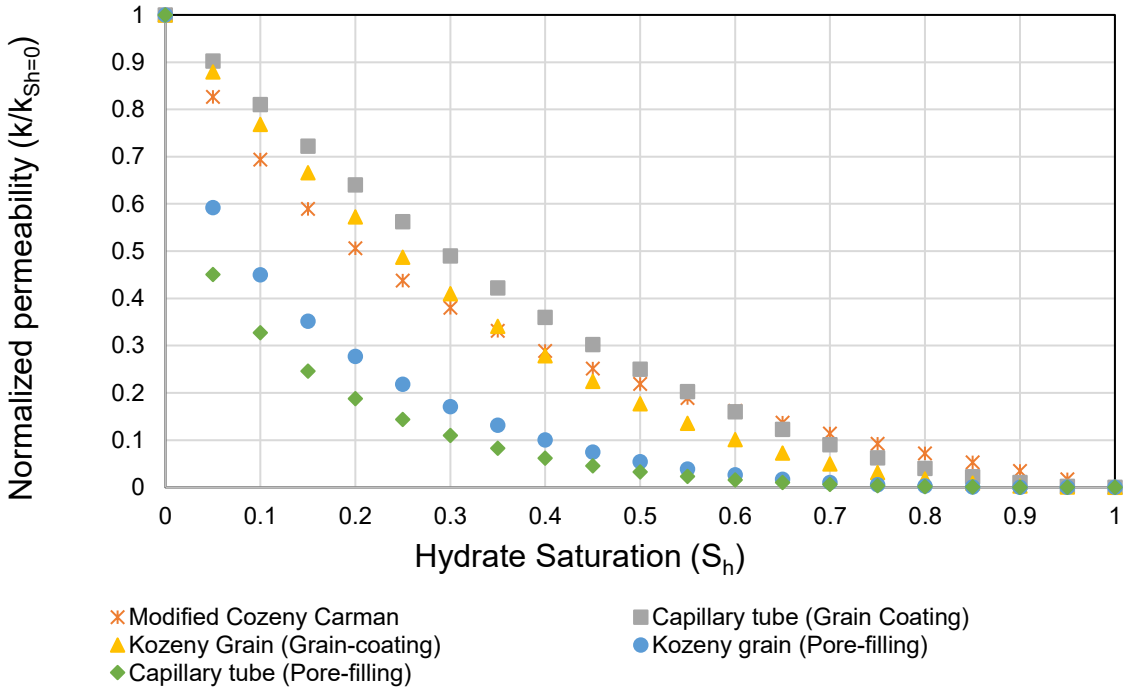

Figure 14: Normalized permeability K/K0 [-] versus the Hydrate Saturation [%]. Symbols: Modified Kozeny Carman (orange), Capillary Tube - Grain Coating (grey), Kozeny Grain - Grain Coating (yellow), Kozeny Grain – Pore Filling (blue), and Capillary Tube – Pore Filling (green).

Then the saturation difference (ΔS_{w+H}) at every step is determined by calculating the difference of the Saturation of the step of interest (i) minus the saturation of the previous step (i-1) which are determined from the CT images calculations as shown in the previous section:

$$\Delta S_{w+H} = S_{(w+H)_i} - S_{(w+H)_{i-1}} \tag{9}$$

Afterwards, the corrected permeability change is used for the calculation of the conversion of water to hydrates, by assuming that the change in permeability inside the core is caused due to hydrate formation or dissociation:

$$C = \frac{V_{brine} \cdot \Delta K_c}{K_{ic}} \tag{10}$$

where, V_{brine} [ml] is the content of brine inside the core, ΔK_c [D] is the corrected permeability difference between the step of interest and its previous step, and K_{1c} [D] is the corrected permeability of the previous step. Also, by dividing the calculated conversion in ml with the initial brine content inside the core, the percentage of the water that was converted into hydrates can be obtained. Even more, the remaining brine content that was not converted into hydrates is calculated by subtracting the conversion (C [ml]) from the initial brine content (V_{brine} [ml]).

The hydrate saturation (S_H [%]) is then calculated from the following equation:

$$S_H = C \cdot S_{w0} + \Delta S_{w+H} \tag{11}$$

where, C [%] is the conversion of water to hydrates, S_{w0} [%] is the initial saturation value inside the core, before starting the hydrate formation process, and ΔS_{w+H} [%] is the saturation difference calculated from the CT images.

Through the following equation, the volume of hydrates (V_H [ml]) is calculated by multiplying the calculated hydrate saturation (S_H [%]) with the pore volume of the porous medium:

$$V_H = PV \cdot S_H = PV \cdot (C \cdot S_{w0} + \Delta S_{w+H}) \tag{12}$$

Additionally, the moles of the water that contribute in the hydrate cages (n_H^w [mol]) is calculated by dividing the grams of water that were converted to hydrates (m_H^w [g]) with the molecular wight of water $M_w^{H_2O}$ which is equal to 18 g/mol:

$$n_H^w = \frac{m_H^w}{M_w^{H_2O}} \tag{13}$$

which is then used for the calculation of mol of CO_2 (n_{CO2} [mol]) that is consumed due to the hydrate formation or released form hydrate cages during dissociation:

$$n_{CO_2} = \frac{n_H^w}{N_H} \tag{14}$$

where, N_H [-] is the hydration number, which is the molar ratio of water molecules to gas molecules in a single hydrate structure. The theoretical value is 5.75 and it is based on the ideal structure of hydrates, where every unit cell consists of 46 water molecules and can host up to 8 CO_2 molecules (46/8 = 5.75) (Q. Sun & Kang, 2016). However, this number can vary in real experimental conditions due to factors like temperature and pressure changes. In this experimental study the hydration number is assumed to be equal to 6.4, since the degree of subcooling while forming the hydrates is low and thus, we assume that not all cages are occupied (lower occupancy) (Uchida, 1998). It has to be mentioned though that the accurate determination of the hydration number is extremely difficult because of the missing knowledge and the limited available information on the literature regarding this matter. There are a few values mentioned on the literature, but the experimental conditions (setup, pressure, temperature etc.) in each case vary and no clear pattern

can be identified in order to determine the hydration number accurately (Anderson, 2003). Based on the available information, the lower the temperature when forming hydrates, the closer the hydration number gets to the ideal one. Based on that and the fact the forming temperature is not very low, the hydration number is assumed to be higher than the ideal one. Also, the hydration number is assumed to remain the same throughout all the experiments.

By having determined the amount of CO_2 moles that are consumed or released from the hydrate cages, the mass of CO_2 (m_{CO2} [g]) is calculated with the help of the molecular weight of CO_2 ($M_w^{CO_2}$ = 44 [g/mol]):

$$m_{CO_2} = n_{CO_2} \cdot M_w^{CO_2} \tag{15}$$

Finally, the density of the hydrates (ρ_H [g/ml]) at each step of the experiments is calculated by the following equation:

$$\rho_H = \frac{m_{CO_2} + m_H^w}{V_H} \tag{16}$$

where, m_{CO2} [g] is the mass of CO_2 that was consumed or released from the hydrate cages, m_H^w [g] is the mass of the water that contributed to the hydrate cages and V_H [ml] is the volume of hydrates.

3.4.5 Volume Change of Brine due to CO_2 Solubility

Because of some small increase in saturation values even at temperatures outside of the hydrate formation zone, that were observed from the CT image saturation calculations and that will be discussed in the upcoming chapter, the effect of the dissolution of CO_2 into the brine and its effect on the brines volume was decided to be calculated.

At first, the solubility of CO_2 into the water was determined. Because of the fact that the brine solution in every experiment was the same and it was 1wt% NaCl, it was assumed that this very low salinity does not decrease the solubility of CO_2 in a significant way and thus the graphs that were used for the determination of the CO_2 solubility refer to water as the solvent. Three different graphs were used to calculate the CO_2 solubility, two of them were found on the literature (Carroll et al., 1991; Dodds et al., 1956) and the third was generated from the HydraFlash software (Figure 15). After calculating the CO_2 solubility from the three plots and for the same pressure and temperature conditions it appeared that values calculated from the HydraFlash plot were extremely close to the average value of the three and thus it was decided to continue with the CO_2 solubility values that were calculated from it.

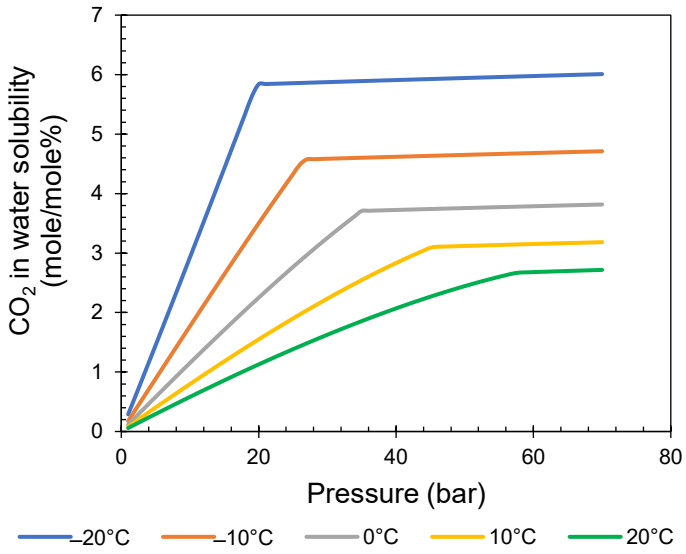

Figure 15: The solubility of CO2 into the water (mole/mole%) versus pressure and at different temperature curves. From this plot the solubility of CO2 was determined at 30 bar pressure and at temperatures that correspond to the temperature steps that were followed during each experiment. Because there are only curves related to -20C, -10C, 0C, 10C, and 20C, the solubility of temperatures in between these temperatures was estimated by using linear interpolation. This plot was generated from HydraFlash software.

Then, with the help of the D. Li et al., (2011), the density of the CO_2-H_2O-NaCl mixture is calculated. The model of this study is applicable for conditions of geological storage of CO_2, with an applicable range of 273 K - 573 K, 0.001-1000 bar, and 0-6 mol/kg NaCl concentration as well as CO_2 concentrations ranging from 0 up to saturation point. So, the following equation is used to calculate the density of the mixture:

$$\rho_{mix} = \left(1000 + 58.4 \cdot M_{NaCl} + 44 \cdot M_{CO_2}\right) / \left(\frac{1000 + 58.4 \cdot M_{NaCl}}{\rho_B} + \frac{18 \cdot (1 + K) \cdot M_{CO_2}}{\rho_w}\right) \quad (17)$$

where, ρ_B and ρ_w [g/cm3] are the densities of aqueous NaCl solution and pure water, respectively and are assumed to be both equal to 1 g/cm3. Also, M_{NaCl} and M_{CO2} [mol/kg] are the molalities of NaCl and CO2 inside the mixture respectively. The coefficient K is calculated in the following equation and finally, ρ_{mix} [g/cm^3] is the density of the mixture.

$$K = \alpha_1 T^2 + \alpha_2 T + \alpha_3 + \alpha_4 T^{-1} + \alpha_5 T^{-2} + (\alpha_6 T^2 + \alpha_7 T + \alpha_8 + \alpha_9 T^{-1} + \alpha_{10} T^{-2}) P \quad (18)$$

where, T [K] and P [bar] indicate the temperature and pressure and α_1 – α_{10} are parameters that are listed below in Table 2 as determined from the D. Li et al., (2011), study:

Table 2: List of parameters a_1 through a_{10} for equation (15) as obtained from (D. Li et al., 2011)

α_1	$0.38384020 \cdot 10^{-3}$
α_2	-0.55953850
α_3	$0.30429268 \cdot 10^{3}$
α_4	$-0.72044305 \cdot 10^{5}$
α_5	$0.63003388 \cdot 10^{7}$
α_6	$-0.57709332 \cdot 10^{-6}$
α_7	$0.82764653 \cdot 10^{-3}$
α_8	-0.43813556
α_9	$0.10144907 \cdot 10^{3}$
α_{10}	$-0.86777045 \cdot 10^{4}$

Since the brine solution in all experiments is 1wt% NaCl, the mass of the NaCl (m_{NaCl} [g]) that is included into the brine solution is given from the following equation:

$$m_{NaCl} = \frac{m_{brine} \cdot 1}{100} \tag{19}$$

where, m_{brine} [g] is the mass of the brine that is injected into the core

Then the mol of NaCl (n_{NaCl} [mol]) would be the division of the NaCl mass (m_{NaCl} [g]) with the molecular weight of NaCl (M_w^{NaCl}= 58.4 g/mol):

$$n_{NaCl} = \frac{m_{NaCl}}{M_w^{NaCl}} \tag{20}$$

The mass of the solvent which is the water (m_w [kg]) would be:

$$m_w = \frac{m_{brine} - m_{NaCl}}{1000} \tag{21}$$

So, the molality of NaCl (M_{Brine} [mol/kg]) can be determined by:

$$M_{brine} = \frac{n_{NaCl}}{m_w} \tag{22}$$

For the molality of CO_2 (mol_{CO2} [mol/kg]) the solubility of CO_2 is required, which is acquired from HydraFlash as explained earlier, in order to determine the amount of CO2 mol (n_{CO_2} [mol]) that are dissolved into the mass of the water which is the solvent:

$$M_{CO_2} = \frac{n_{CO_2}}{m_w} \tag{23}$$

Eventually, by having calculated the molalities of both CO_2 and brine, and the coefficient K, the density of the mixture is then calculated, which in turn is used to calculate the volume of the mixture (V_{mix} [ml]) by assuming at the same time that the mixture has a mass (m_{mix} [g]) equal to:

$$m_{mix} = m_{brine} + m_{CO_2} \tag{24}$$

$$V_{mix} = \frac{m_{mix}}{\rho_{mix}} \tag{25}$$

After the determination of the new volume of the mixture CO_2-H_2O-NaCl the volume expansion caused due to the dissolution of CO_2 into the brine can be estimated by subtracting the initial volume of brine (V_{brine} [ml]) from the volume of the mixture:

$$V_{expansion} = V_{mix} - V_{brine} \tag{26}$$

By calculating the volume expansion, the hydrate properties and more specifically the amount of hydrate saturation and hydrate volume into the core can be corrected even further by excluding this volume increase that is cause due to the dissolved CO_2 into the brine from the calculations that were described earlier. The next chapter is going to include the discussion around the results that came up after the processing and of the available data and the implementation of the aforementioned calculations about the saturation, the permeability, the hydrate properties, and the CO_2 solubility, in order to get a better understanding about the CO_2 hydrate kinetics during the formation and dissociation processes.

Chapter 4: Discussion

4.1 Overview

This chapter presents and analyzes the results that were obtained from the study. The two main objectives of the study are the investigation of the kinetics of the formation and dissociation of CO_2 hydrates inside porous media as well as the effect of the degree of subcooling as the main driving force on the kinetics of these two processes, and thus, various experimental data were obtained through the core-flooding experiments in order to address the research questions and contribute to the overall understanding of the CO_2 hydrate formation and dissociation processes in depleted gas reservoir conditions.

The collected data include the dynamic pressure and temperature data of the core sample give information about the kinetics of hydrates, including the onset of macroscopic hydrate nucleation by noticing a significant pressure drop due to CO_2 encapsulation together with a temperature increase due to the exothermic reaction. In addition, some indication of hydrate dissociation can be identified, for example the onset of the macroscopic hydrate dissociation by a change in slope of the temperature curve during thermal stimulation. It would be noted; the CO_2 is injected constantly into the system during both the formation and the dissociation of the hydrates (dynamic system) to mimic the reservoir condition. Some tests also conducted under the Medical CT scanner to not only monitor the whole process of hydrate formation and dissociation but also use it in calculating important parameters of the hydrates during different stages, such as: hydrate saturation, water to hydrate conversion, and CO_2 consumption/release. During each test gas permeability measurements performed multiple times to gain insight to the hydrate behavior in pore scale. Below, the types of data and the experiments from which they were collected can be seen in Table 3, followed by an overview of the all the experiments' parameters and observations in Table 4:

Table 3: A list of all the data that was collected during the experimental work. Under each experiment, the green boxes indicate what type of data was obtained from it, whereas the red boxes indicate parts that were not focused on.

Data \ Experiment	1st	2nd	3rd	4th	5th	6th
Pressure Data						
Temperature Data						
CT Imaging						
Gas Permeability Tests						
Hydrate Properties Calculations						

Table 4: Summary of experimental parameters and observations: degree of subcooling, formation and dissociation methods, induction time, pressure drop and temperature increase during hydrate formation, and dissociation onset.

Experiment	Subcooling [°C]	Hydrate Formation Method	Induction Time [h]	Onset of Hydrate Nucleation	Hydrate Dissociation Method	Onset of Dissociation [°C]
Experiment 1	6	Direct Cooling	3.5	1.2 bar P drop 1.8 °C T increase	Step Heating 1.5 °C Step Interval	6.3 °C
Experiment 2	4	Direct Cooling	23	3.9 bar P drop 1.8 °C T increase	Step Heating 1.5 °C Step Interval	6.2 °C
Experiment 3	10	Direct Cooling	0.17	0.2 bar P drop 1.6 °C T increase	Step Heating 1.5 °C Step Interval	6.3 °C
Experiment 4	4.5	Step Cooling 3.5 °C Step Interval	-	2 bar P drop 1.2 °C T increase	Step Heating 1.5 °C Step Interval	6.2 °C
Experiment 5 1st Cycle	4.5	Step Cooling 2 °C Step Interval	-	-	Step Heating 1.5 °C Step Interval	-
Experiment 5 2nd Cycle	4.5	Direct Cooling	8.5	3.8 bar P drop 2.1 °C T increase	Step Heating 1.5 °C Step Interval	6.4 °C
Experiment 6 1st Cycle	4.5	Ramp Cooling 0.1 °C/h Cooling Rate	-	2.4 bar P drop 1.4 °C T increase	Ramp Heating 0.1 °C/h Heating Rate	6.3 °C
Experiment 6 2nd Cycle	4.5	Direct Cooling	9.5	2.1 bar P drop 1.4 °C T increase	Ramp Heating 0.1 °C/h Heating Rate	6.3 °C

Before discussing all the individual experiments, it is useful to consider the phase behavior of the CO_2 and water phase diagram. This diagram outlines the thermodynamic conditions under which hydrates can form and dissociate, depending on pressure and temperature. In all conducted experiments the pressure tried to be constant at 30 bar, and temperature was the only parameter that changed throughout the tests aiming for pressure and temperature conditions that would locate the system inside the hydrate stability zone (G-H), and avoid the condense CO_2 area (L_C-H) just above the dashed line as seen in Figure 3.

4.2 Experimental Results

4.2.1 First Experiment

The first experiment involved forming hydrates at 1 °C, using direct cooling method, corresponding to a 6 °C subcooling. Dissociation was induced by step heating in 1.5°C intervals up to 11.5 °C, followed by an instant increase to 20 °C to eliminate residual hydrate structures.

The primary sign of macroscopic hydrate nucleation is characterized by a simultaneous pressure drop because of the CO_2 encapsulation within the hydrate cages and a temperature increase caused by the exothermic reaction of hydrate formation (Figure 16). In this case, the pressure drop was about 1.2 bar and the temperature increased for 1.8 °C with 3.5 h (4.8 PV) induction time considering the CO_2 injection time. After the induction period, pressures increased until they

reached a fairly stable state, corresponding the hydrate growth stage during CO_2 injection. The pressure increase can be attributed to the volume increase of hydrates causing a partial core pores blockage and available porosity reduction, and also to the fact that hydrate cages trap more CO_2 due to the ongoing CO_2 injection resulting in more stable hydrate structures. The permeability that was calculated after the brine saturation process was 2.27 D and was decreased to 0.43 D when the hydrate growth stage was completed.

Then thermal stimulation method was used to dissociate the hydrates. By observing the pressure curve during the dissociation process, an overall upward trend can be seen. It looks that probably a partial blockage remains which causes the pressure rise even while the core is heated, or the backpressure membrane causes the pressure to drift away as gas is released from the system during the dissociation process. The expected behavior would be that the pressure curve would show a downward trend caused by the dissociation of hydrates and return back to the initial level. Only at the final heating step the pressure curve becomes flat with a slight decrease, before starting an increase together with the final temperature increase towards 20 °C. Finally, the temperature profile shows a deviation in its trend during the 4th step of heating, during the transition from 5.5 °C to 7 °C, when compared to the temperature transition between the other heating steps. In fact, during this step the temperature increase happens slower (the ramping slope of the temperature curve is lower) and more gradual whereas in the rest of the steps it appears sharper and faster. Roughly around 6.3 °C the onset of dissociation is seen due to the endothermic reaction of the CO_2 hydrate dissociation.

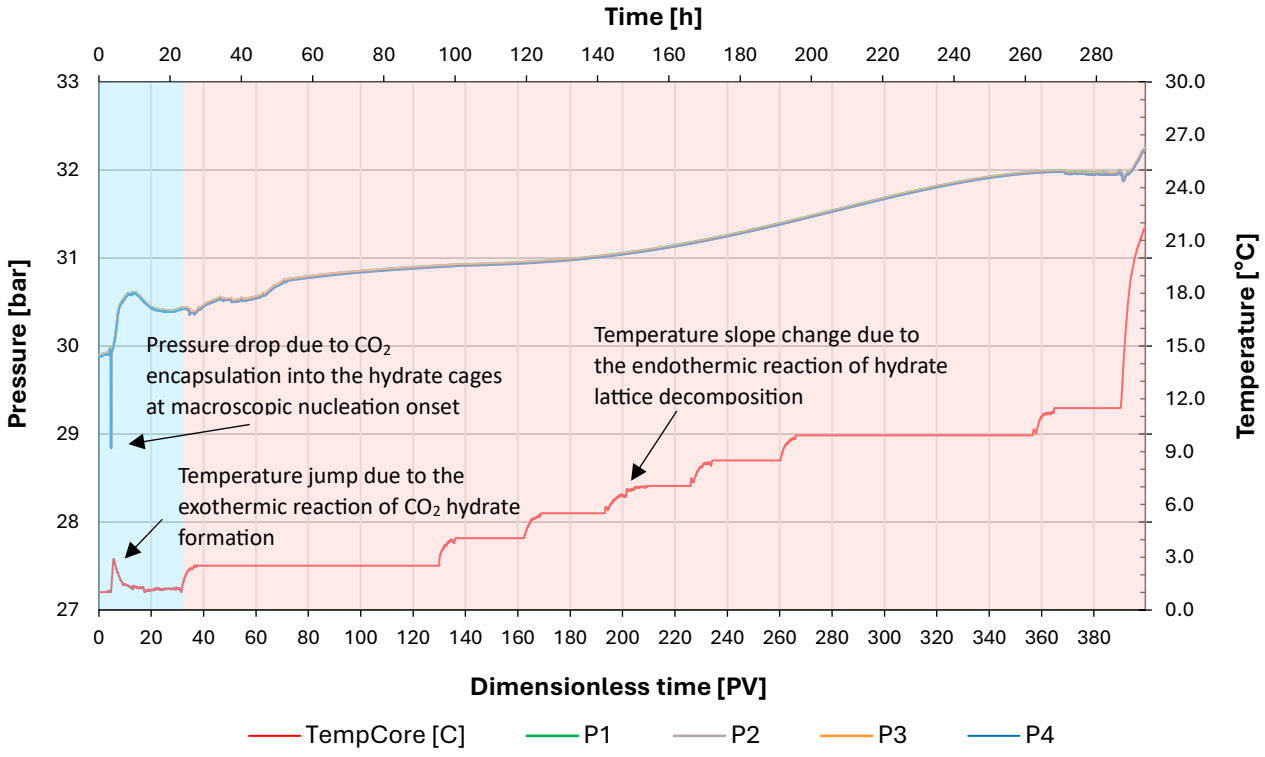

Figure 16: Pressure and Temperature profile during CO_2 hydrate formation and dissociation for S_w=25% of 1 wt% NaCl brine solution. The initial conditions are: 30 bar. The light blue-colored part of the graph shows the hydrate formation stage, whereas the light red-colored part indicates the dissociation phase.

4.2.2 Second Experiment

The second experiment investigated the hydrate formation and dissociation in a 1wt% NaCl solution, evaluating the effect of 4 °C subcooling, starting from 3 °C for hydrate forming. The dissociation process included the step heating method with an interval of 1.5 °C for thermal stimulation. The pressure and temperature data throughout the experiment are presented in Figure 17.

In this case, even though the hydrate forming method was the constant cooling, the hydrate forming temperature was 3 °C, in order to investigate a 4 degree of subcooling lower than in the first experiment. The induction time is observed after 23 h (31.4 PV) from the beginning of CO_2 injection and it is by 19.5 h higher than the first experiment (3.5 h induction time). A pressure drop of 3.9 bar was recorded, and the simultaneous temperature increase accounted for 1.8 °C change inside the core. The calculated permeability was reduced from 1.92 D after the brine saturation phase ended to 0.51 D when the hydrate growth phase was completed.

Thermal stimulation in steps of 1.5 °C is performed until 11.5 °C and afterwards the temperature is set directly to room temperature (20 °C). The pressure curve during the entire dissociation process showed a very similar behavior to the first experiment, namely, an increasing trend throughout the entire dissociation process. From the temperature curve during the 3rd step and by changing the temperature from 6 °C to 7.5 °C a change in slope can be seen and more specifically, when the core is at 6.2 °C, indicating the endothermic reaction of hydrate dissociation. Finally, only after the step heating process is completed and as soon as the temperature starts increasing to 20 °C, the pressure shows a sudden drop of 0.2 bar before starts increasing further.

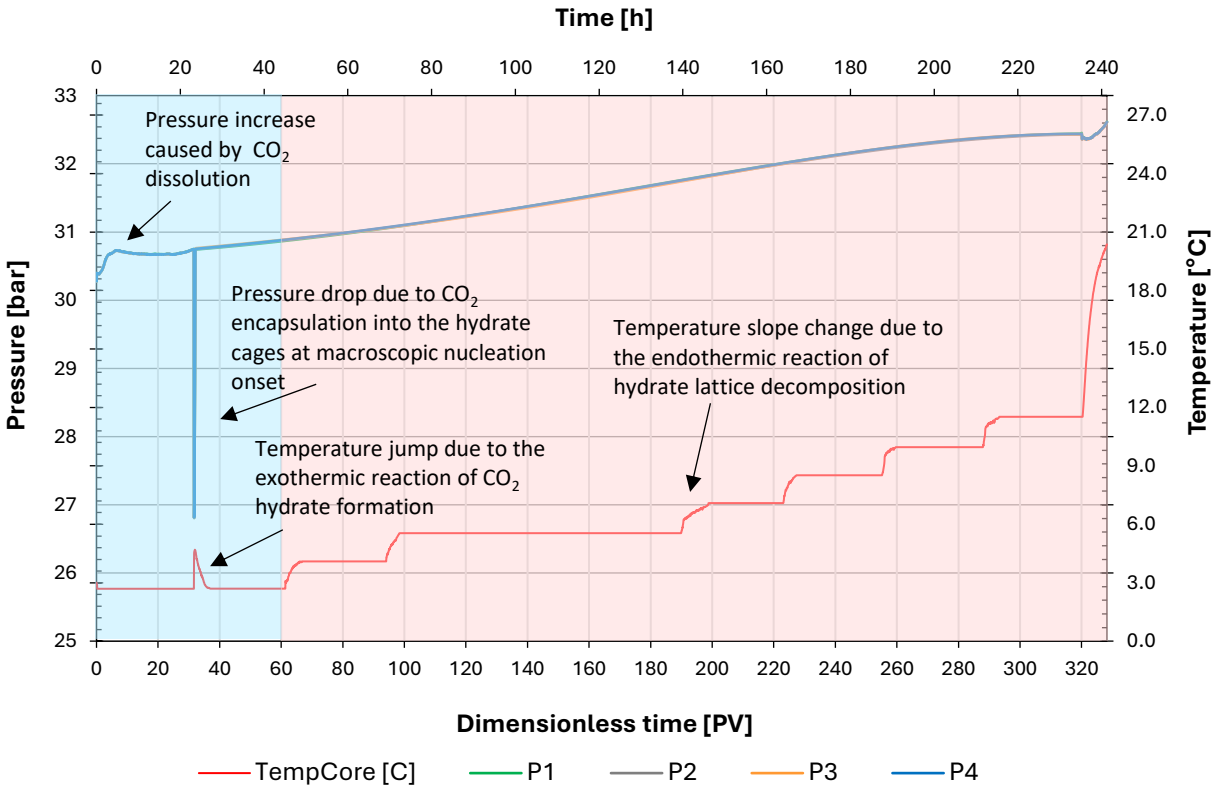

Figure 17: Pressure and temperature profile during CO_2 hydrate formation and dissociation for S_w=25% of 1 wt% NaCl brine solution. The initial conditions are: 30.6 bar and 3 °C. The light blue-colored part of the graph shows the hydrate formation stage, whereas the light red-colored part indicates the dissociation phase.

4.2.3 Third Experiment

The third experiment was conducted under the medical CT scanner to examine the effect of an even higher degree of subcooling (10 °C) by forming hydrates at -3 °C. For the CO_2 hydrate dissociation, the same interval of 1.5 °C per step was followed during the thermal stimulation until 12 °C before increasing the temperature to room temperature. Except from the P-T data recording in Figure 18, the CT images of the core as well as the results of their analysis can be seen in Figure 19 and Figure 20, respectively.

The formation of CO_2 hydrates is achieved with direct cooling to -3 °C. The induction time was witnessed very quickly, and more specifically only 10 min after the CO_2 injection started. The pressure drop caused by the encapsulation of CO_2 into the hydrate cages was 0.2 bar, and the exothermic reaction caused the core's temperature to increase from -3 °C to -1.4 °C meaning that the temperature was increased by 1.6 °C before stabilizing back to its initial value. Afterwards, during the growth period the pressure jumped to 30.3 bar where it remained almost stable until the end of the growth stage. The permeability was calculated to be 2.24 D after the brine saturation was completed, and was decreased to 0.54 D before hydrate dissociation.

The difference in this experiment is that the steps lasted significantly less time than the previous two experiments. The behavior of the pressure curve for one more time shows an increasing trend. It needs to be mentioned that at the end of the first and during the second heating steps, the CO_2 flow had stopped. During step heating a pressure jump can be seen and after that, the pressure kept increasing as if it "followed" the temperature increase during the step heating method. This time the room temperature could not have affected the pressure curve since this setup was located inside a room where its temperature was constantly kept at around 18 °C. After 6 °C was reached, which is the beginning of the 7th heating step (7.5 °C), and during the 8th step (9 °C), the temperature curve showed a deviation in slope caused by the endothermic reaction of CO_2 hydrate dissociation. This deviation is noticed at 6.3 °C approximately.

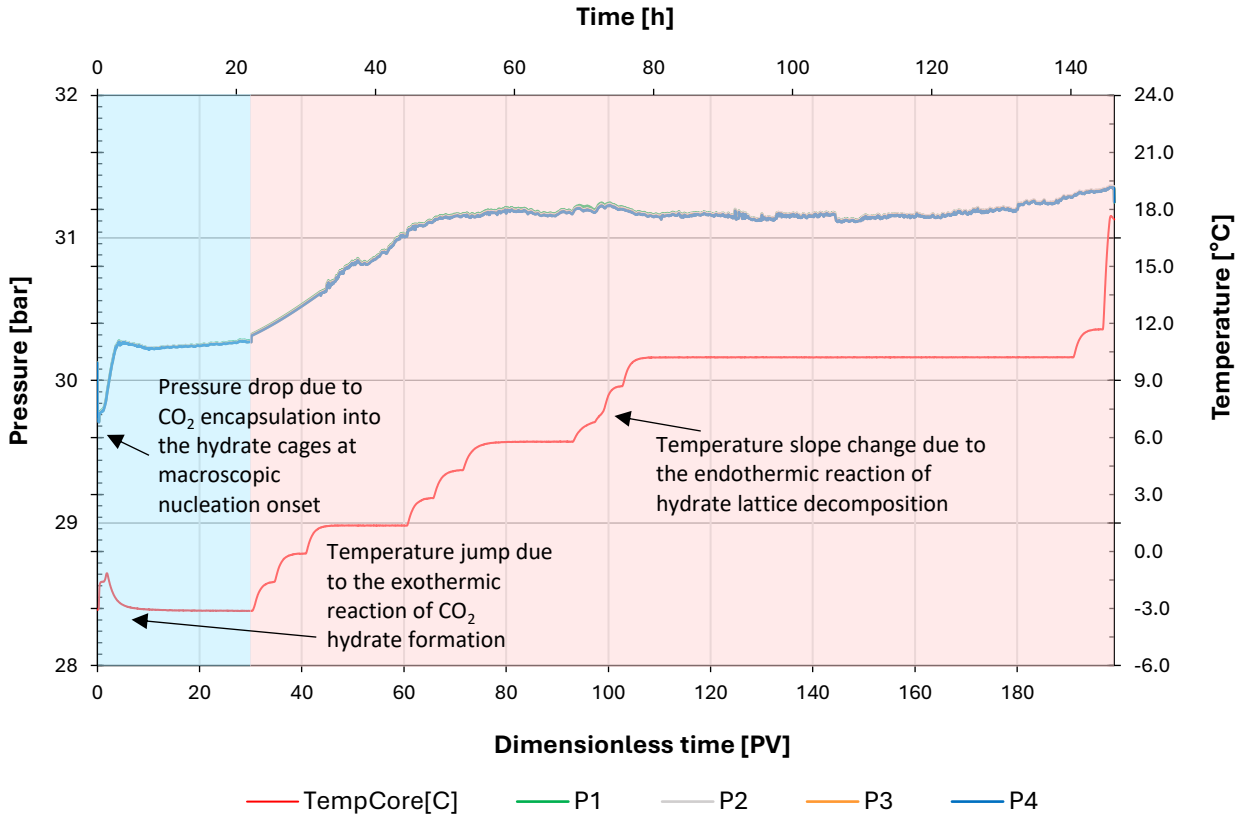

Figure 18: Pressure and temperature profile of the core during CO2 hydrate formation and dissociation for S_w=25% of 1 wt% NaCl brine solution. The initial conditions are: 29.8 bar and -3 °C. The light blue-colored part of the graph shows the hydrate formation stage, whereas the light red-colored part indicates the dissociation phase.

4.2.3.1 CT Imaging Analysis

The data extracted from the CT scans are presented in this section. Figure 19 depicts the dynamic CT images of water/hydrate saturation maps during the brine saturation, the hydrate formation and dissociation process at every step. All these images illustrate the pattern of water plus hydrate saturation in all three stages of the experiment. From these images a vertical high porosity zone (dark blue shadow) can be distinguished a few centimeters away from the middle of the core which is the locations of the thermocouple (T_{core}). From Figure 19, it is also visible that the core sample that was used during this experiment was layered, meaning that it consists of layers with

different porosity and permeability. More specifically, while looking on the images during the brine saturation process it is clear that the brine was not able to spread uniformly into the core but it was situated in a certain area of the core which was high permeability layer. Additionally, it is observed that during the process of hydrate formation, the distribution of hydrates changed as we see that the brine/hydrate saturation increased even at the low permeability zone. This phenomenon can be attributed either to overcoming of the capillary forces of the pore throats or due to the displacement of the immobile brine. Even more, during the dissociation process, even though the average saturation of the core decreased it appears that the brine was distributed more uniformly along the core.

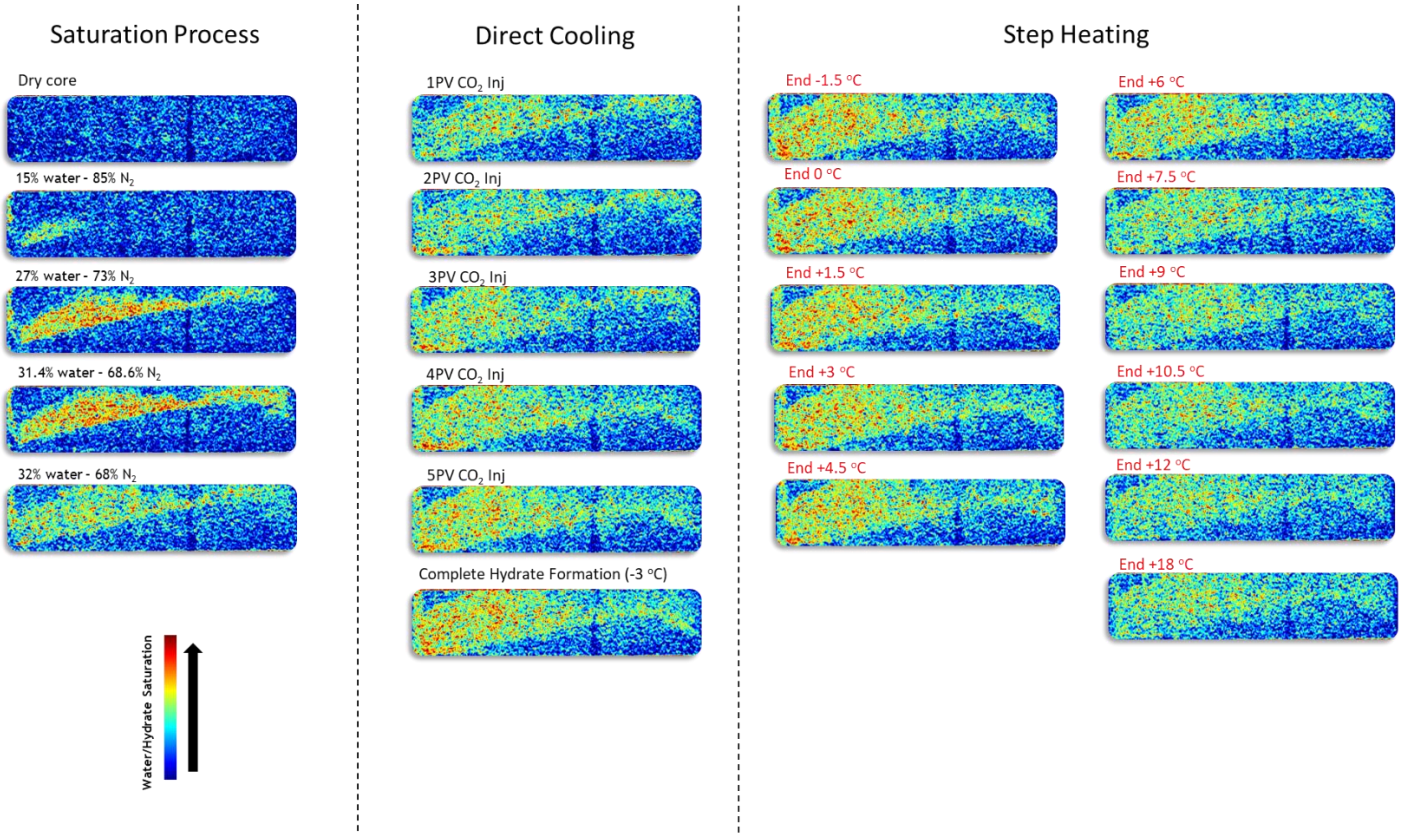

Figure 19: Dynamic CT images of water/hydrate saturation during the brine saturation process of horizontal Bentheimer core (PV = 44 ml) as well as during hydrate formation (Direct Cooling) and dissociation (Step Heating). Flow direction is from left to right. (Colors indicate water + hydrate saturation qualitatively. Red: high water/hydrate saturation; green/yellow: intermediate saturation; blue: low saturation).

Figure 20 quantified any changes that occurred on different stages of the experiment in terms of the change in the average value of the brine/hydrate saturation of the entire core. Starting from 32% saturation at the end of the brine saturation process, the average saturation of the core increased to 41.4% when the hydrate formation process was completed due to the formation of hydrates. Also, it is observed that most of the saturation increase caused by the hydrate formation was achieved until five pore volumes (5PV) of CO_2 were injected, which is equivalent to 3.6 h, reaching a value of 40.6%, less than 1% difference from the last scan of the hydrate formation process. During the dissociation process a slight decrease in the saturation value is observed from the first heating step (-1.5 °C) until the fifth heating step (4.5 °C) which accounts for a 1.7%

decrease. When the core is heated up to 6 °C (sixth step) there is a more significant drop in saturation, but the most significant drop was recorded during the seventh step (7.5 °C) which accounted for a drop of 3.7% indicating more hydrate dissociation. During the temperature change from 6 °C to 7.5 °C two scans were taken in-between, one at 6.3 °C which is approximately during the time that the deviation of the temperature curve was observed, and one at 6.8 °C. There is a significant decrease in saturation between these two scans supporting the claim that the deviation in the temperature curve is caused due to the endothermic reaction of the hydrate dissociation. Later on, the saturation further decreases to 34.1% at 9 °C (eighth heating step), but after that point the decrease is very small until the scan at 12 °C as seen from the figures reaching a value of 33.9%. This value is almost 2% higher than the initial saturation after the brine saturation process and indicates that CO2 hydrates had not completely dissociated up to that temperature. The saturation returned to its initial value only after the temperature was directly increased to the room temperature (18 °C).

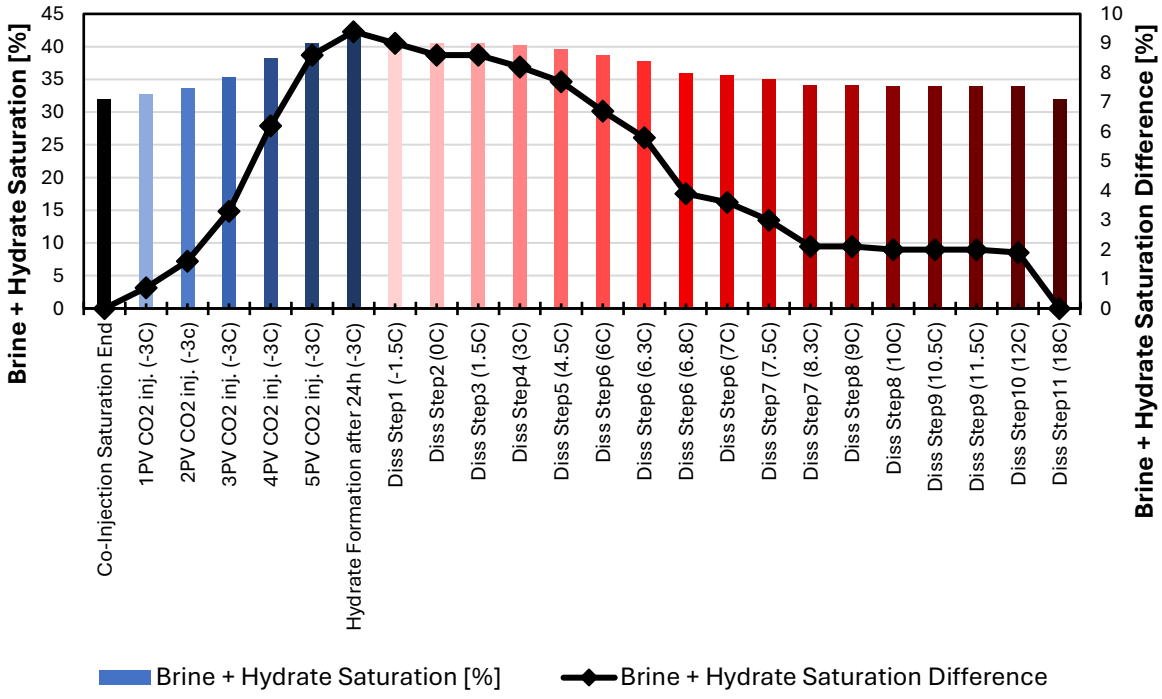

Figure 20: The water plus hydrate saturation is plotted for different stages of the experiment as obtained from the CT images during each of these steps (columns), whereas the water plus hydrate saturation difference from the initial brine saturation at every step is represented with the black curve.

4.2.4 Fourth Experiment

For this experiment a different cooling method is introduced. More specifically, the hydrate forming temperature is 2.5 °C and it is achieved after cooling the system in steps (step cooling) with an interval of 3.5 °C starting from the temperature of 9.5 °C. Despite the difference in the method of forming hydrates, the dissociation method remained the same for this experiment also.

Discussion

During the step heating method, five steps with an interval of 1.5 °C were employed until the temperature reached 10 °C before going directly to 20 °C. Figure 21 shows the pressure and temperature data, while Figure 22 and Figure 23 are related to the results of the CT scans of this experiment. Additionally, during this experiment, together with the CT scans, gas permeability tests were performed as well.

It is observed from Figure 21 that the indication of hydrate nucleation (pressure drop and temperature increase) was observed at approximately 98 PV of injected CO_2, which is 72 h after the injection of CO_2 started. It has to be noted that this time is not the real induction time because the duration of the cooling steps until the hydrate forming temperature is included. But, as induction time could be the amount of time from the beginning of the third cooling step at 2.5 °C until hydrate nucleation was detected, which accounts for approximately 20 h. Even more, the pressure drop that was recorded was roughly 2 bar, and the temperature increase due to the exothermic reaction was 1.2 degrees. By following the pressure curve, it shows an increase after CO_2 injection begun until it becomes relatively stable at 44 h until the pressure drop caused by the hydrate formation. This increase in pressure can be attributed to the CO_2 dissolution and volume expansion of the water, because the CT image results presented in Figure 23 together with the permeability calculations do not indicate significant changes that would show any presence of hydrates that could potentially cause this pressure behavior. The pressure increase started as soon as the CO_2 injection started and at a temperature 2 °C outside of the hydrate stability zone. Later, until the end of the hydrate formation stage the pressure shows a slight increasing trend.

During this thermal stimulation process the overall trend of the pressure curve does not indicate significant changes. Though, it has to be mentioned that the sudden pressure drops and jumps noticed at the end of each temperature step are due to the gas permeability tests that were performed. In the beginning of each step the pressure appears higher than the middle and end of it. Due to the high flow rates of CO2 that were used during each permeability test the pressure appears higher at the beginning of each step, and appears lower and more flat at the middle and end of it indicating a stabilization of the system's pressure after a certain amount of time. The 3rd heating step was aimed to reach 7 °C, exactly at the equilibrium line temperature of the hydrate formation zone, but at a temperature between 6.2 °C and 6.3 °C a deviation in the temperature curve was observed making the slope of the curve less sharp in comparison with the other heating steps, indicating one more time the endothermic reaction of hydrate dissociation.

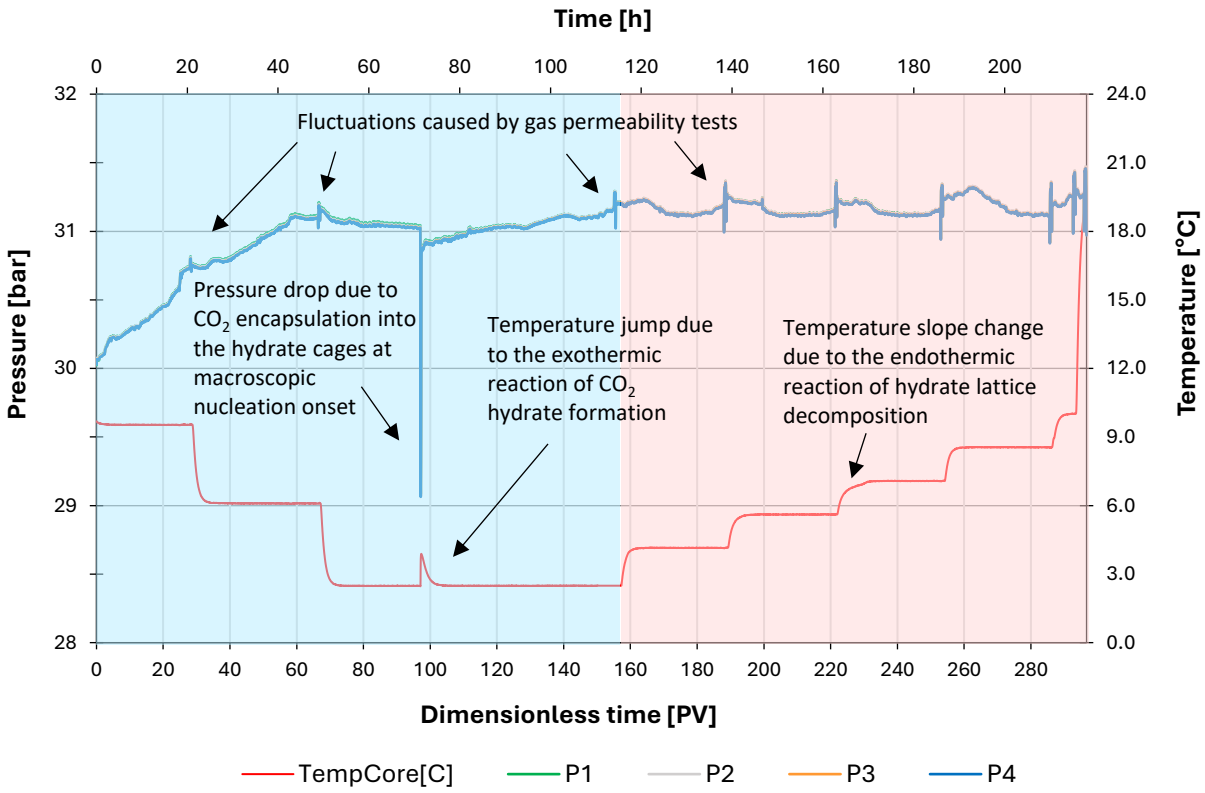

Figure 21: Pressure and temperature profile of the core during CO_2 hydrate formation and dissociation for S_w = 24% of 1 wt% NaCl brine solution. The initial conditions of the experiment are: 30.1 bar and 9.5 °C. The light blue-colored part of the graph shows the hydrate formation stage, whereas the light red-colored part indicates the dissociation phase.

4.2.4.1 CT Imaging Data

Figure 22 depicts the dynamic CT images of water/hydrate saturation maps during the brine saturation, the hydrate formation and dissociation process at every step. It is visible that the core sample that was used during this experiment was not layered in contrast with the previous experiment. Though, the biggest amount of the brine solution was accumulated relatively close to the inlet and more specifically at the first section of the core (left side).

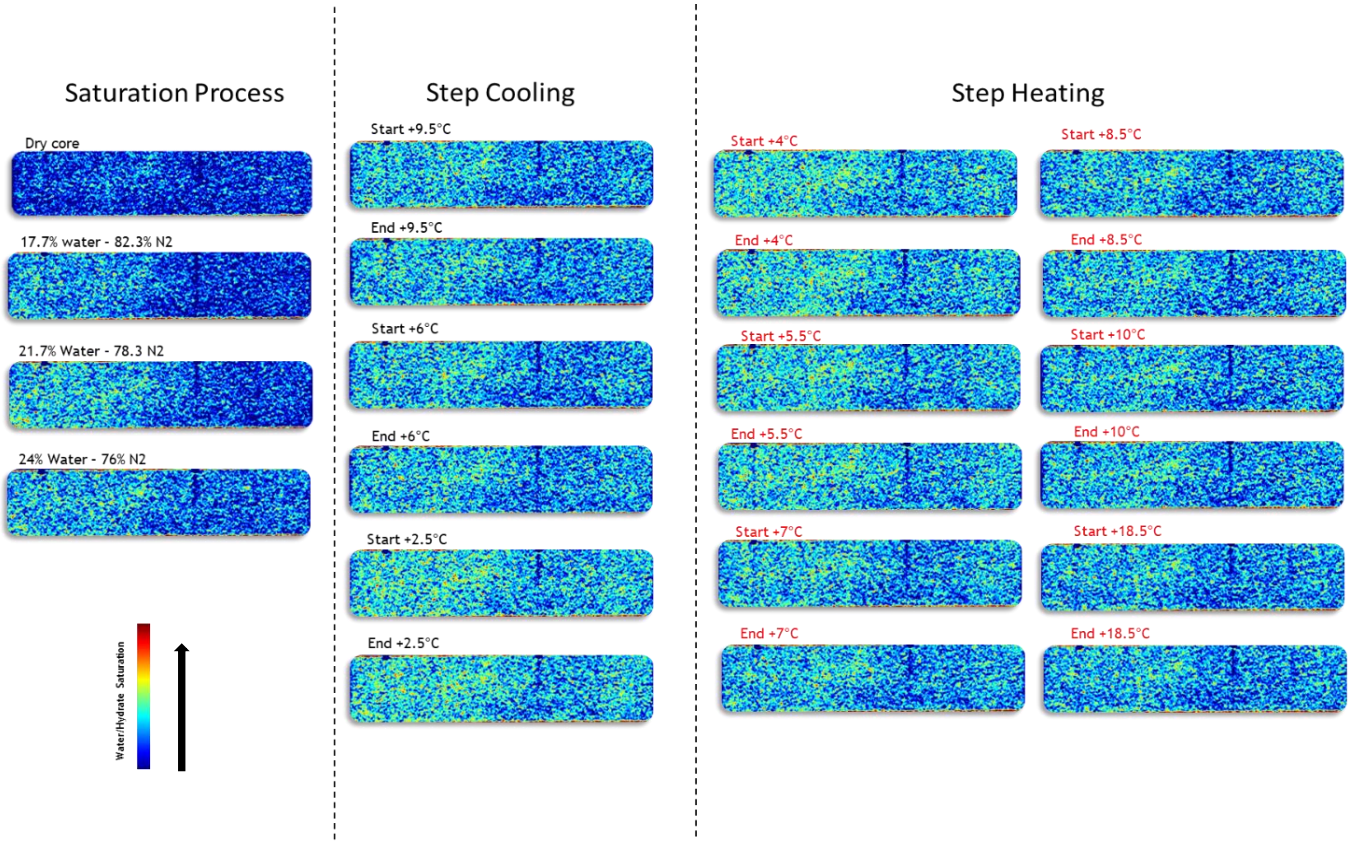

Figure 22: Dynamic CT images of water/hydrate saturation during the brine saturation process of horizontal Bentheimer core as well as during hydrate formation (Step Cooling) and dissociation (Step Heating). Flow direction is from left to right. (Colors indicate water + hydrate saturation qualitatively. Red: high water/hydrate saturation; green/yellow: intermediate saturation; blue: low saturation).

From Figure 23 a sudden increase in the average saturation can be observed at the first cooling step at 9.5 °C, followed then by a lesser increase during the second cooling step at 6.5 °C reaching a total 2.1% increase in saturation since the end of brine saturation process. At the last cooling step (2.5 °C) when the indications of hydrate formation appeared, the average saturation increased to 30.5%, 6.5% higher than the value of saturation after the end of the brine saturation process. During the dissociation process, a decrease of 0.6% is seen during the first heating step (4 °C), and similar one of 0.8% at the next temperature of 5.5 °C. At the third step which was at the temperature of 7 °C the saturation decreased significantly down to 26.3%, meaning that a big number of hydrates dissociated. Later on, during the next heating steps the saturation decrease is relatively small and ranges from 0.1 to 0.4%. The ultimate saturation value is almost the same with the value of the first cooling step but it does not decrease down to the value of the brine saturation process. The reason for that is the fact that the system did not remain enough time at 18.5 °C which led to incomplete dissociation of the existing CO_2 hydrates.

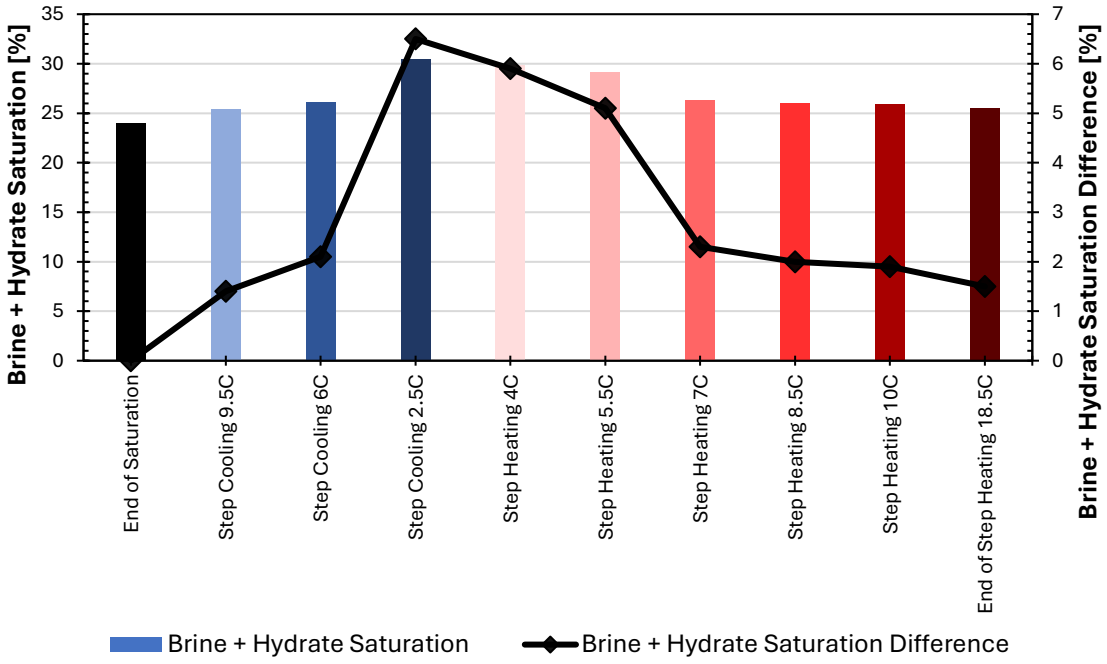

Figure 23: The water plus hydrate saturation is plotted for different stages of the experiment as obtained from the CT images during each of these steps (columns), whereas the water plus hydrate saturation difference from the initial brine saturation at every step is represented with the black curve.

4.2.4.2 Permeability Measurements

From the results of the permeability calculations a behavior that follows the saturation changes can be extracted by looking at Figure 24. More precisely, a slight drop in permeability is observed during the first two steps of cooling until the big drop during the hydrate formation occurrence at the last cooling step. The formation of hydrates resulted to an almost 50% reduction in permeability of the core. During the process of step heating the permeability increases by very little during the first two steps, but increases by half a Darcy during the third heating step (7 ^{o}C). After that, the permeability increases slightly until the value of 2.57 D at the highest temperature (18.5 ^{o}C), which is very close to the permeability value after the brine saturation process ended.

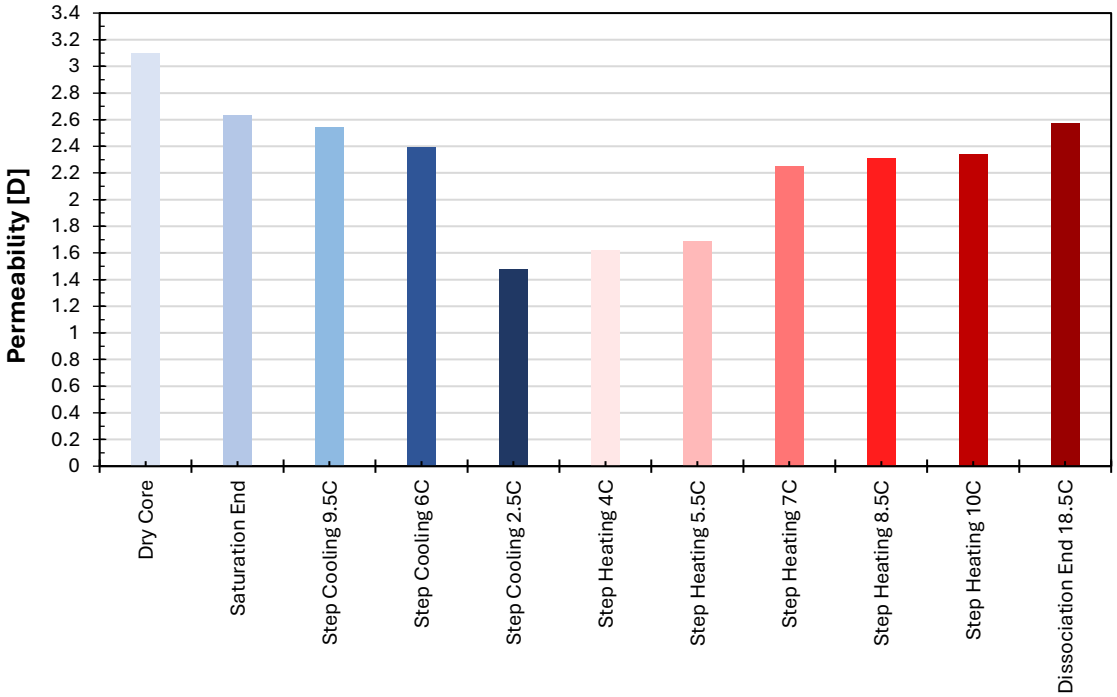

Figure 24: Permeability values of the sand stone core sample during different phases of the experiment as calculated after the implementation of gas permeability tests and Darcy's Law.

4.2.4.3 Hydrate Properties Calculations

Below the results of various hydrate properties are presented and discussed, which were calculated based on the pressure-temperature data, CT image analysis and permeability measurements. The values of the calculated hydrate saturation are corrected based on the Modified Kozeny Carman model since it is the empirical model to which the calculated values are closer to. Then based on these corrections the corrected properties of hydrates can be extracted.

From Figure 25, that follows, the changes in saturation of the existing brine solution inside the core caused by the dissolution of CO_2 can be observed. The values of saturation increase range from 0.79 % at the highest temperature (18.5 °C) to 1.35 % at the lowest temperature (2.5 °C). These calculations are implanted in order to identify how the dissolution of CO_2 into the existing brine can affect its volume so that the unexpected saturation changes during the CT images analysis can be explained better. Especially during the cooling process where some saturation increase is observed even at the first cooling step during which hydrates cannot be formed since the system's temperature is outside of the hydrate stability zone based on the bulk system. It is observed that the small percentage of water to hydrate conversion that is observed at the first cooling step (9.5 °C) is in fact volume increase caused by the dissolution of water. During the next cooling step (6 °C) this percentage increases even further and also it appears that the hydrate saturation percentage exceeds the percentage of volume increase caused by the dissolution of CO_2. Probably indicating that there is a small number of hydrates present after the second cooling step.

From the Figure 25 and Figure 26 one can observe that at the end of the hydrate formation stage a maximum of 16.2% hydrate saturation is achieved. At the same time, 55% percent of the existing water was converted into hydrates and almost 2.5 g of CO_2 contributed into the formation of hydrates. During the dissociation process, the biggest changes are observed during the third heating step (7 °C) after which the hydrate saturation is decreased to 4 %, and the slope of the CO_2 consumption shows the sharpest decrease.

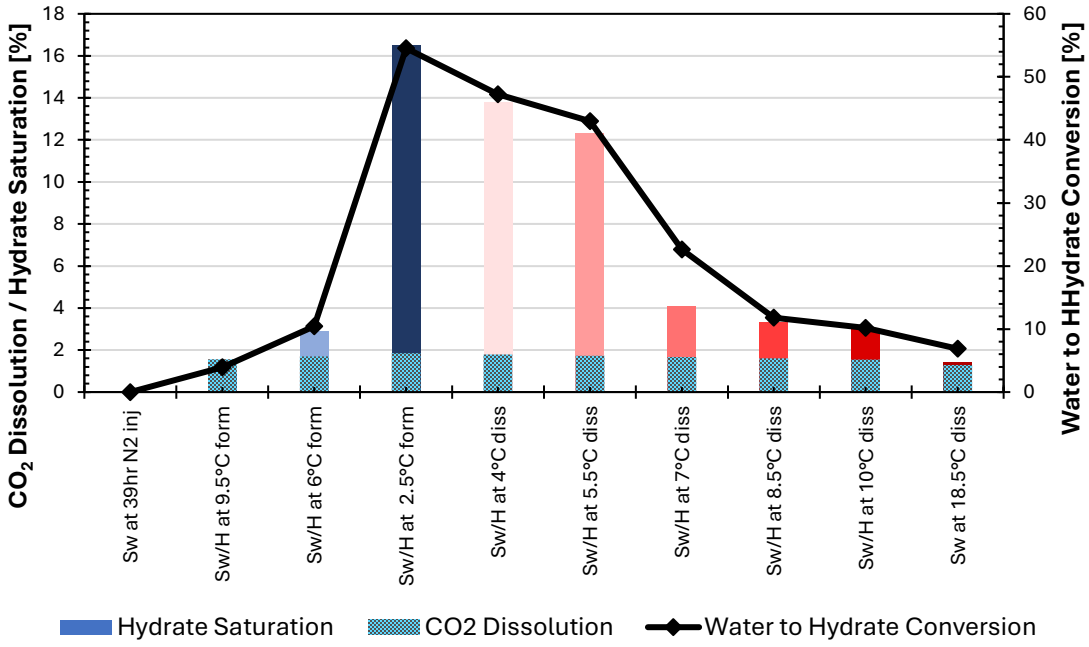

Figure 25: Hydrate saturation, CO_2 solubility-related saturation increase, and water-to-hydrate conversion that were calculated at each temperature step of the fourth experiment. Bars represent the calculated hydrate saturation and the portion attributed to dissolved CO_2, while the line (secondary axis) shows the corresponding water-to-hydrate conversion percentages.

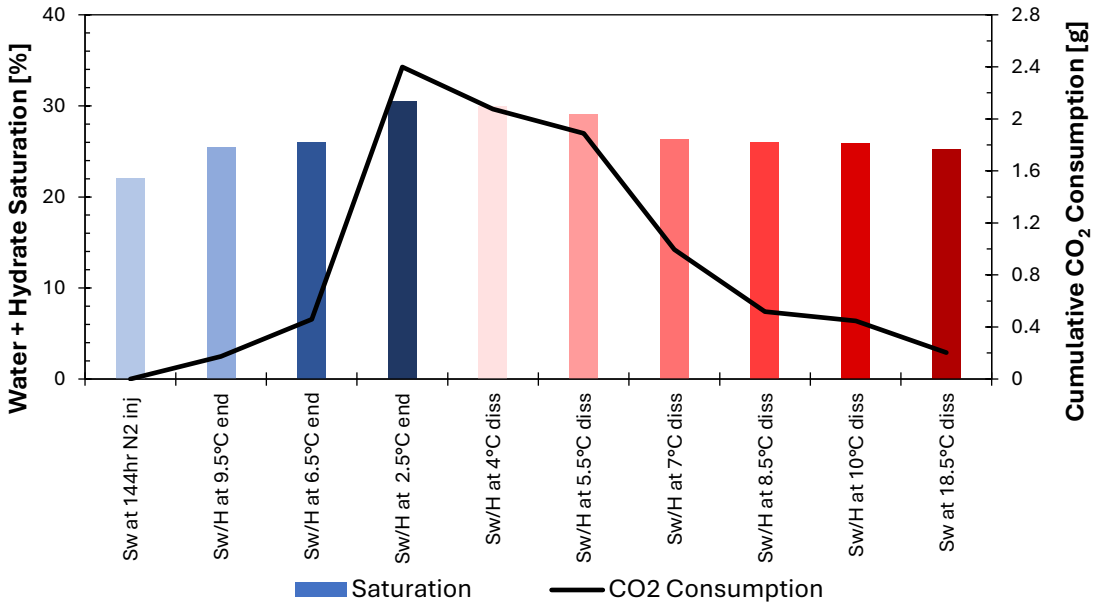

Figure 26: Water + Hydrate saturation [%] in columns, together with the amount of CO2 that was consumed [g] from the hydrate cages (black line) at every stage of the experiment.

4.2.5 Fifth Experiment

This experiment included two hydrate formation and dissociation cycles. During the first cycle, the step cooling method was used during the hydrate formation process. In comparison with the fourth experiment, the step cooling process started at a higher temperature (12.5 °C) and included 6 cooling steps until the desired temperature was reached (2.5 °C). During the second cycle the hydrate forming method was the isothermal one at 2.5 °C. The same dissociation method (step heating) was used for both cycles. The pressure and temperature data of cycles are depicted in Figure 27.

The first cooling step at first cycle initiated at a higher temperature than the previous experiment, 12.5 °C and selected a 2 °C temperature interval until reaching the lowest temperature. During the first cycle no indication of hydrate formation was observed. In contrast with all the previous experiments no pressure-drop and temperature increase were recorded throughout the entire cycle. The pressure curve showed an increase at the beginning of the experiment because of the initiation of CO_2 injection which kept decreasing slowly from the middle of the first cooling step onwards, until reaching a fairly stable state at the end of the first cycle at 20 °C.

For the second cycle the hydrate formed by using the isothermal method (direct cooling) with 2.5 °C being the hydrate forming temperature. The indication of hydrate formation appeared quite fast, namely 8.5 h after reducing the temperature to 2.5 °C. The pressure drop was about 3.8 bar and was followed by a temperature increase of 2.1 °C because of the exothermic reaction of the hydrate formation. The pressure curve after the pressure drop remained 30.2 bar during the hydrate formation phase, 0.3 bar higher in comparison with the pre-hydrate formation stage. During the dissociation, the step heating process was followed with an interval of 1.5 °C until 12.5

°C before directly heating the system to 20 °C. The pressure curve during the dissociation showed a gradual decrease throughout all the heating steps reaching a plateau at 20 °C at around 30 bar. As for the temperature curve a change in slope was observed a little bit before reaching a stable temperature during the second heating step (6.5 °C) and while the temperature was increasing for the third step to 8.5 °C. So, after 6.1 °C the change in slope was recorded due to the endothermic reaction of the dissociation of hydrates.

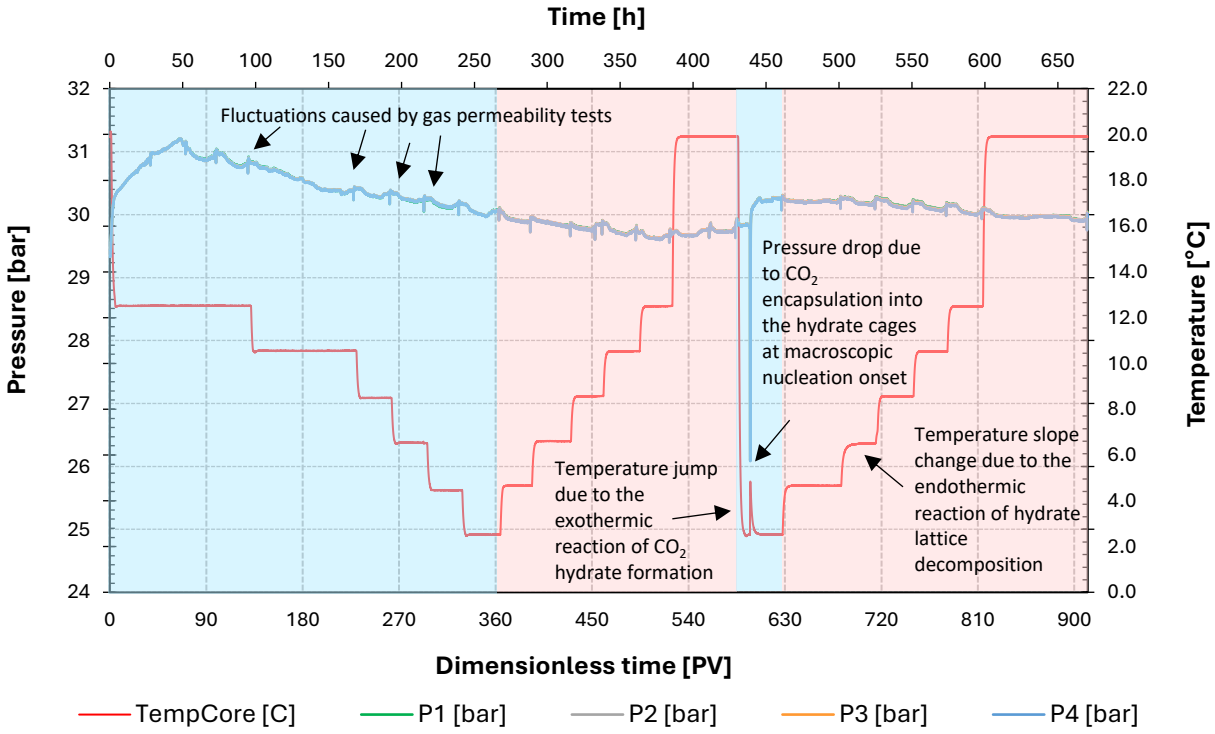

Figure 27: Pressure and temperature profile of the core during CO_2 hydrate formation and dissociation for two cycles of cooling and heating, for S_w = 27.8% of 1 wt% NaCl brine solution. The initial conditions of the experiment are: 29.6 bar and 20 °C. The light blue-colored parts of the graph show the hydrate formation stage of each cycle, whereas the light red-colored parts indicate the dissociation phase of each cycle.

4.2.5.1 CT Imaging Analysis

Figure 28 depicts the dynamic CT images with water/hydrate saturation maps during the brine saturation, the hydrate formation and dissociation process at every step for the first cycle. By looking at the images of all the cooling and heating steps, there are no significant differences that would indicate increased or decreased water/hydrate saturation inside the core sample. What can be observed is some water movement inside the core because of the dynamic nature of the experiment. Conversely, in Figure 29, in which the CT images of the second cycle are presented, a clear increase in saturation inside the core can be observed at the end of the hydrate formation process. During the dissociation, and as the temperature increased at each step, a decrease in the core's saturation is observed, leading to an image, at the end of the experiment, similar to the one after the brine saturation process was completed. In this experiment the brine was distributed more uniformly.

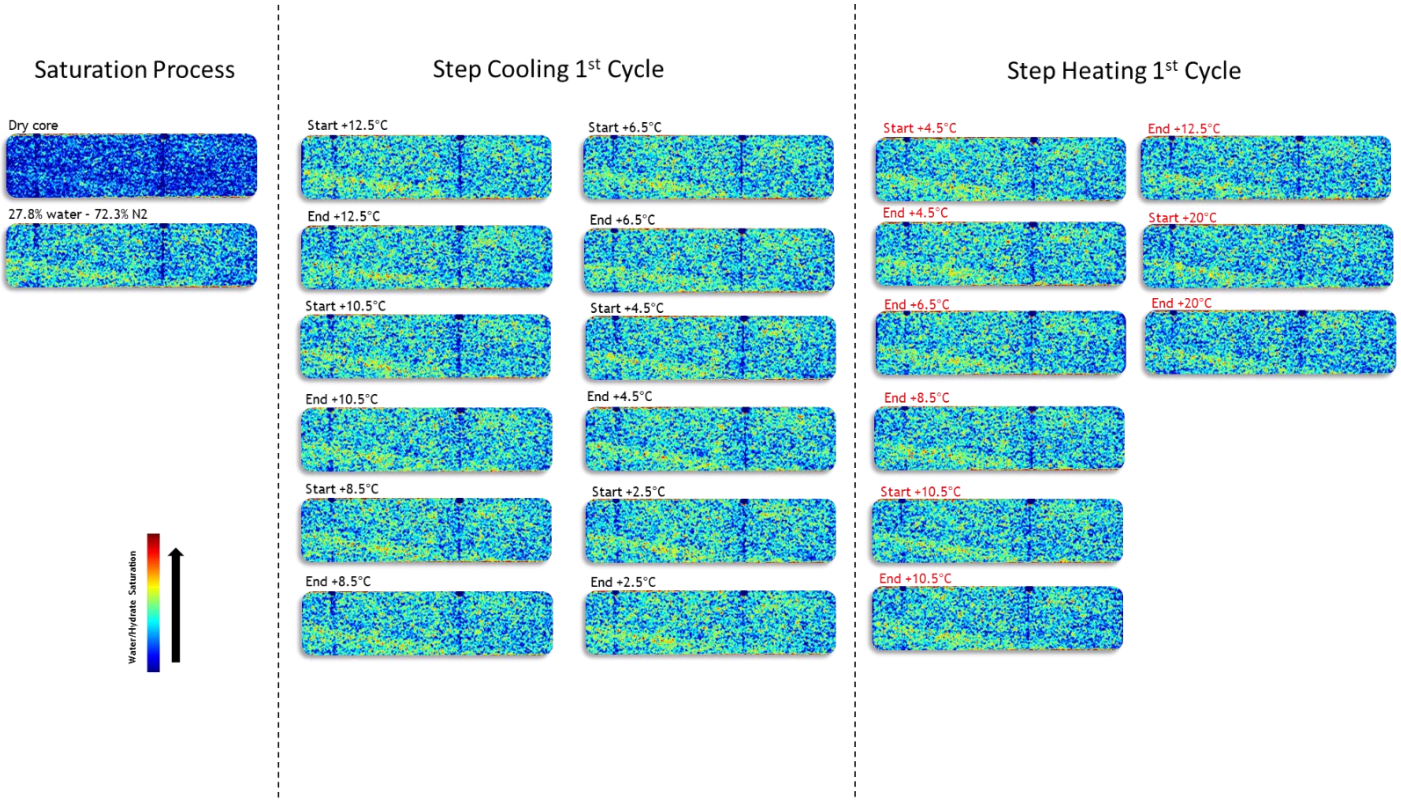

Figure 28: Dynamic CT images of water/hydrate saturation during the brine saturation process of horizontal Bentheimer core as well as during hydrate formation (Step Cooling) and dissociation (Step Heating). Flow direction is from left to right. (Colors indicate water + hydrate saturation qualitatively. Red: high water/hydrate saturation; green/yellow: intermediate saturation; blue: low saturation).

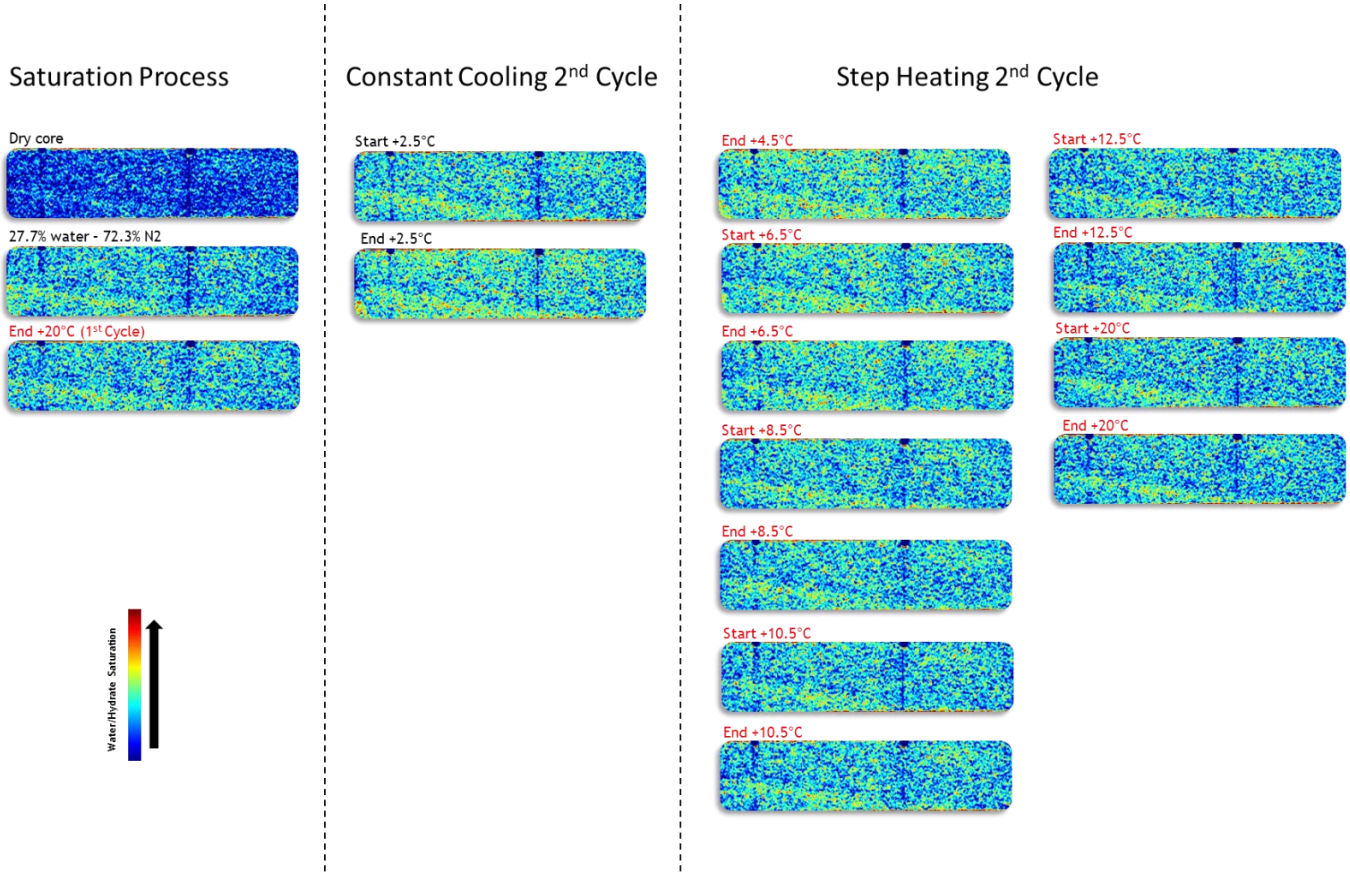

Figure 29: Dynamic CT images of water/hydrate saturation during the brine saturation process of horizontal Bentheimer core as well as during hydrate formation (Step Cooling) and dissociation (Step Heating). Flow direction is from left to right. (Colors indicate water + hydrate saturation qualitatively. Red: high water/hydrate saturation; green/yellow: intermediate saturation; blue: low saturation).

After the analysis of the CT images for the first cycle an unexpected increase in the average saturation of the core can be seen at the first cooling step which is at 12.5 °C this time in Figure 30. As the cooling process progressed the saturation value kept increasing but in a very small rate. The maximum saturation that was recorded was at the last cooling step at 2.5 °C. During the discussion of the pressure and temperature data, no indication of hydrates was observed but, that increase in saturation could be attributed to a gradual nucleation occurrence which could have led to the formation of a small amount of hydrates. During the step heating process there is a very small decrease in saturation after every temperature step which leads to a value similar to the initial one.

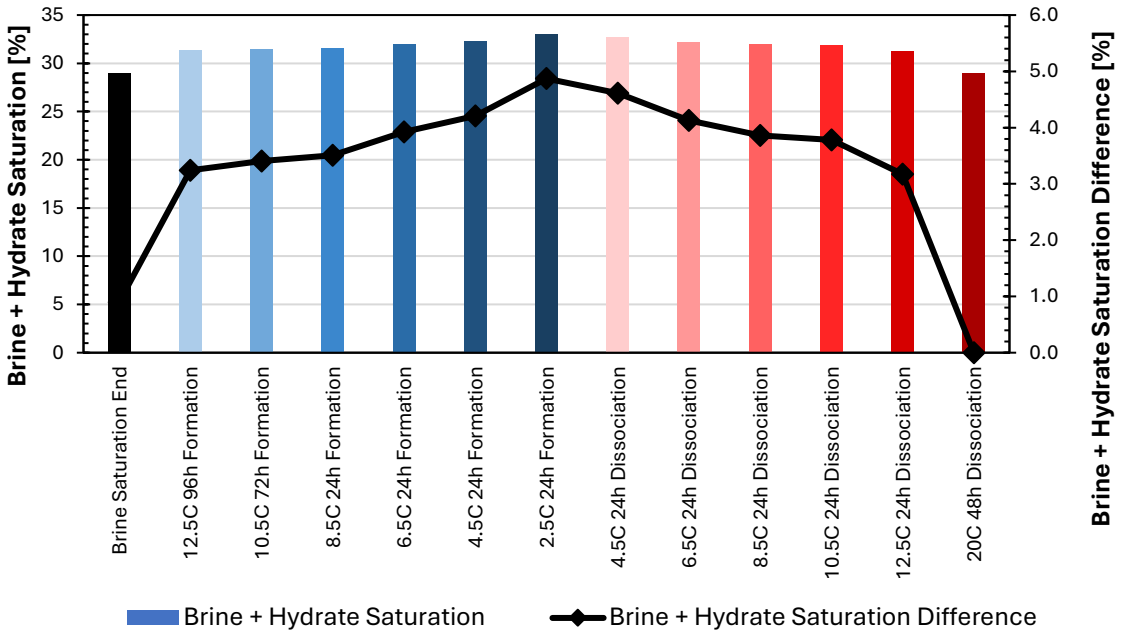

Figure 30: The water plus hydrate saturation is plotted for different stages of the first cycle of the experiment as obtained from the CT images during each of these steps (columns), whereas the water plus hydrate saturation difference from the initial brine saturation at every step is represented with the black curve.

During the second cycle (see Figure 31), even as soon as the temperature of the core was stabilized at 2.5 °C the saturation increased by 3 % reaching a maximum of 8.8 % increase at the end of the hydrate formation phase. During the step heating stage for the dissociation of hydrates at 4.5 °C a small decrease in saturation is recorded, but the major changes occurred at 6.5 °C and 8.5 °C, the second and third heating steps, respectively. These two steps together resulted in a decrease of 6 % in the water plus hydrate saturation since the maximum value after the end of the formation phase. The fourth heating step (10.5 °C) reduced the saturation by roughly 1 % more whereas the next heating step (12.5 °C) reduced the saturation slightly more. Eventually, the saturation returned back to its initial value when the temperature remained at 20 °C for three consecutive days. By comparing the brine + hydrate saturation percentage of the first cycle with the second one, it looks that the maximum saturation recorded at the end of the hydrate formation process was two times higher in the second cycle, which could be attributed to the water hydrate memory.

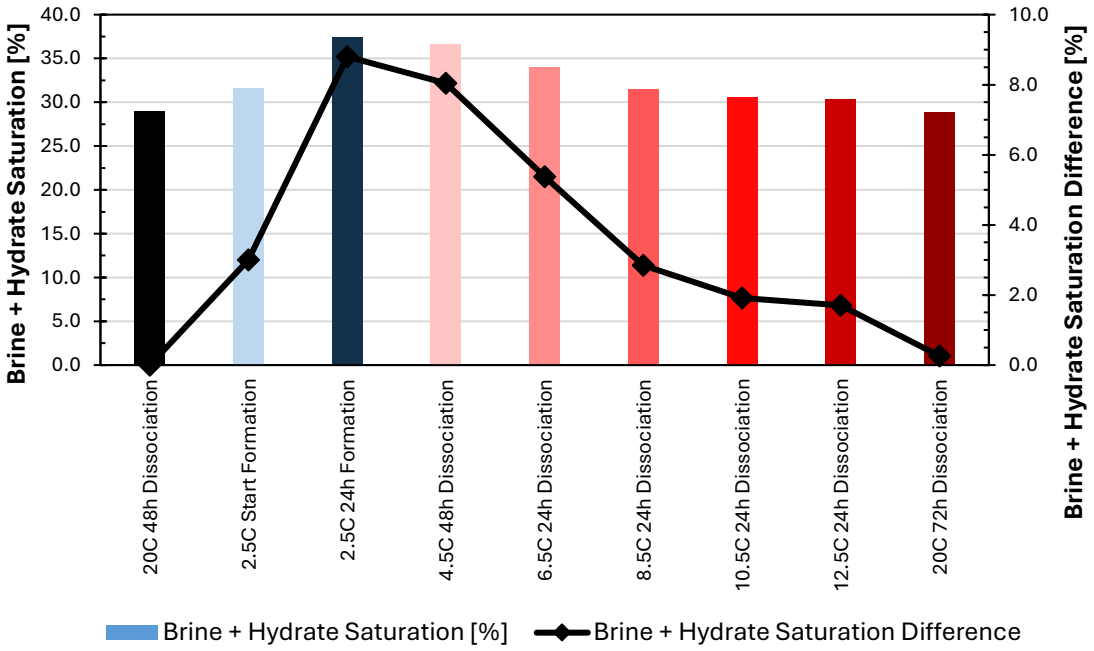

Figure 31: The water plus hydrate saturation is plotted for different stages of the second cycle of the experiment as obtained from the CT images during each of these steps (columns), whereas the water plus hydrate saturation difference from the initial brine saturation at every step is represented with the black curve.

4.2.5.2 Permeability Measurements

The gas permeability measurements for the first cycle of the experiment indicate a very small decrease in permeability during the cooling process. There is a quite significant drop at the first cooling step (12.5 ^{o}C), but the rest three steps do show almost no change. Only the last two steps which are the two lowest temperatures recorded a quite more significant drop in permeability. During the step heating process the permeability increases gradually at every step until it reaches close to the value that was measured after the brine saturation process as can be seen in Figure 32.

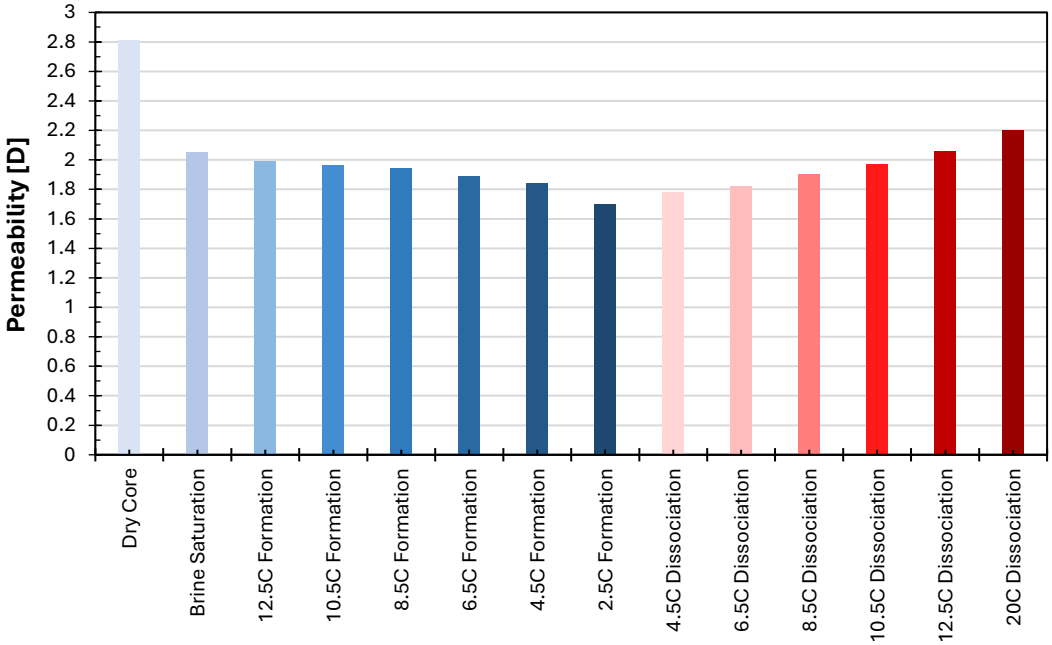

Figure 32: Permeability values of the sand stone core sample during different phases of the experiment's first cycle.

At the second cycle, during which hydrates formed for sure, the permeability was reduced by 1.3 D because of the formation of hydrates (see Figure 33), which accounts for approximately 60 % decrease in permeability. During the dissociation process, the permeability of the core seems to be increasing more during the first three heating steps by reaching the value of 1.69 D at 8.5 °C. The next two steps cause a further increase but not a very significant one, leading to a 0.1 D increase. Finally, there is a relatively big increase during the last heating step at 20 °C to 2.01 D.

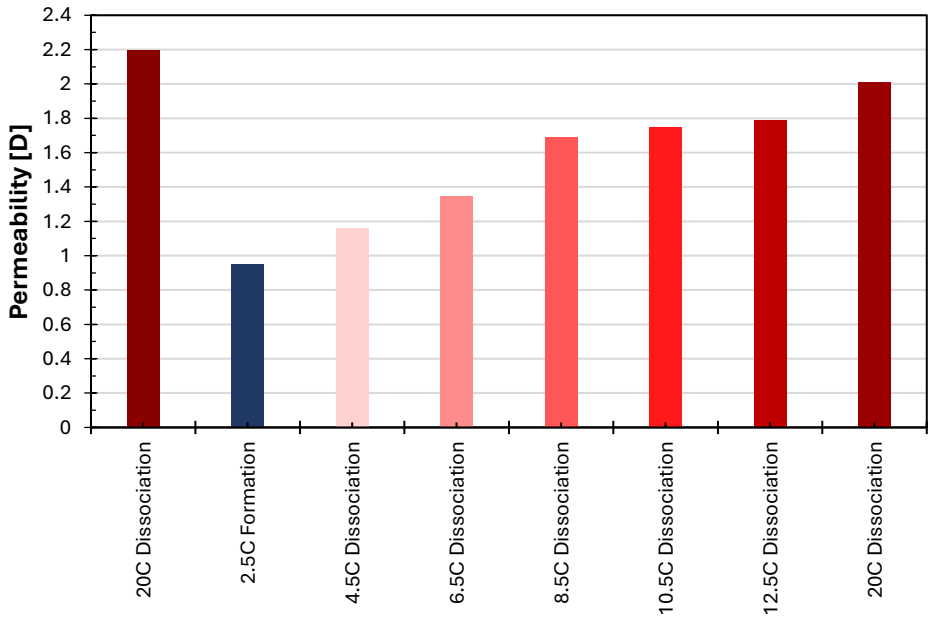

Figure 33: Permeability values of the sand stone core sample during different temperatures of the second cycle of the experiment.

4.2.5.3 Hydrate Properties Calculations

For the first cycle there was no clear indication that hydrates formation according to the pressure-temperature data. Though, some small changes were observed in the water plus hydrate saturation and the permeability measurements. By following the calculation procedure regarding these small changes, a small amount of hydrates appeared to be in the system. The corrected values of the calculated hydrate saturation were obtained based on the Modified Kozeny Carman empirical model.

From Figure 34 it appears that a maximum of roughly 6.6 % of hydrate saturation was achieved at the of the step cooling process, accounting for a total 19 % of water to hydrate conversion. The conversion percentage appears to be non-zero at the first three cooling steps, this happened because of the saturation increase that was caused because of the dissolution of the CO_2 into the water, since it affected both the average saturation of the core and the permeability, and thus affecting the calculations. From the temperature of 6.5 °C the calculated hydrate saturation appears to be higher than the effect of the dissolved CO_2 and until the end of the cooling process, indicating that a small number of hydrates should be present inside the core. As the step heating method follows, the hydrate saturation dropped to almost the one third of its maximum value until the third heating step (8.5 °C). After that point and until the end of the first cycle the hydrate saturation does not appear to be higher than the effect of the CO_2 dissolution. Additionally, Figure 35 shows that approximately 0.77 g of CO_2 were consumed from the hydrate cages, which started increasing sharply from 6.5 °C onwards.

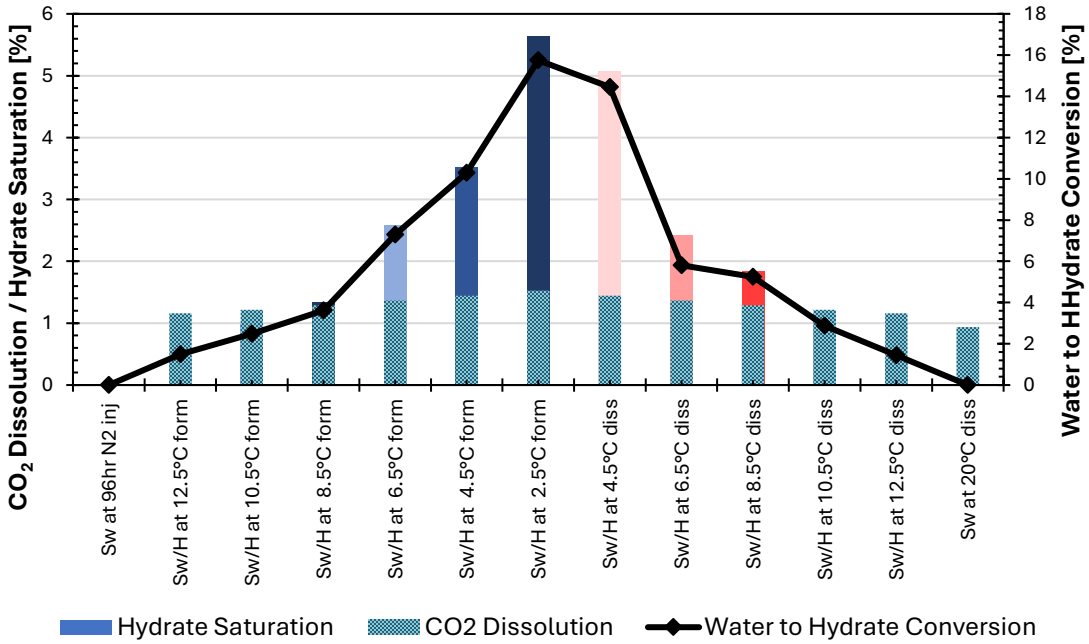

Figure 34: Hydrate saturation, CO_2 solubility-related saturation increase, and water-to-hydrate conversion that were calculated at each temperature step of the fifth experiment's first cycle. Bars represent the calculated hydrate saturation and the portion attributed to dissolved CO_2, while the line (secondary axis) shows the corresponding water-to-hydrate conversion percentages.

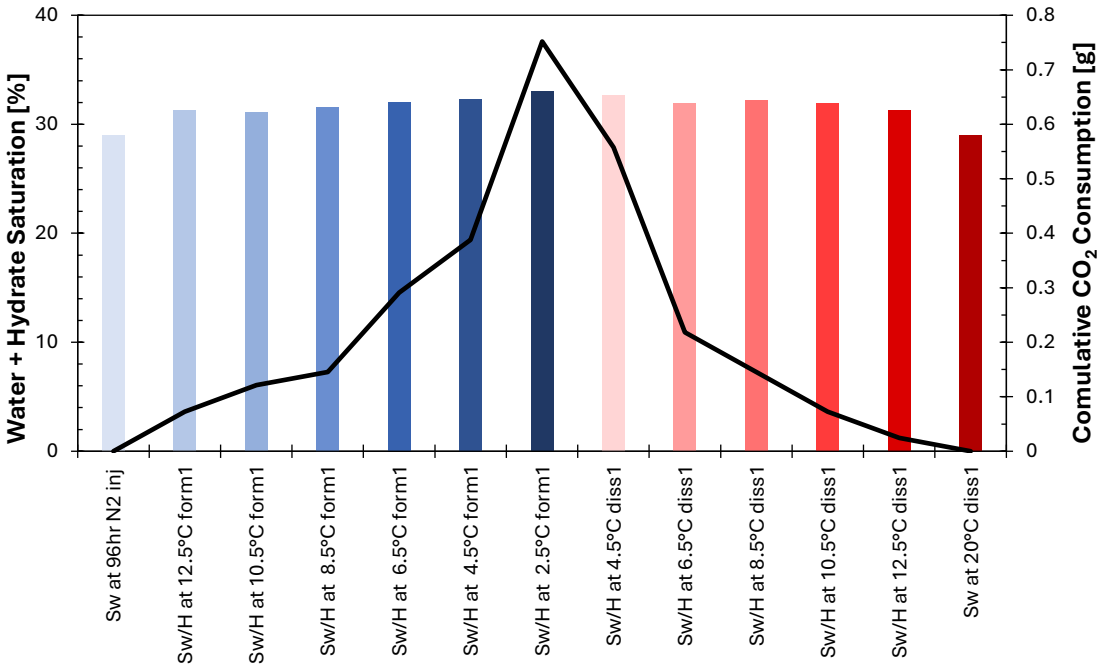

Figure 35: Water + Hydrate saturation [%] in columns, together with the amount of CO2 that was consumed [g] from the hydrate cages (black line) at every stage of the experiment's first cycle.

Regarding the second cycle, the corrected hydrate saturation values were provided the Kozeny Grain (Grain-coating) empirical model. The results of the calculations are presented in Figure 36 and Figure 37, indicated that when the hydrate formation process was finished the saturation of hydrates accounted for 31 %. At the same time 78 % of the existing water inside the core sample was converted into hydrates. Additionally, the amount of CO_2 that was consumed from the hydrate cages was roughly 3.5 g in total. During the dissociation process the saturation of CO_2 hydrates appears to be dropping even from the first heating step (4.5 °C) to 26 %. The percentage drops even more during the second heating step (6.5 °C), but the biggest decrease is seen during the third step (8.5 °C) during which the remaining hydrates accounted for 12 %. Meaning that up until this point roughly the two thirds of the formed hydrates had been dissociated. This can also be observed from Figure 37 in which the CO_2 release curve has a sharp drop during the second and third heating steps. A small number of hydrates remained into the system even until the temperature of 12.5 °C, but they were completely dissociated when the temperature was increased up to 20 °C and remained there for more than 24 h.

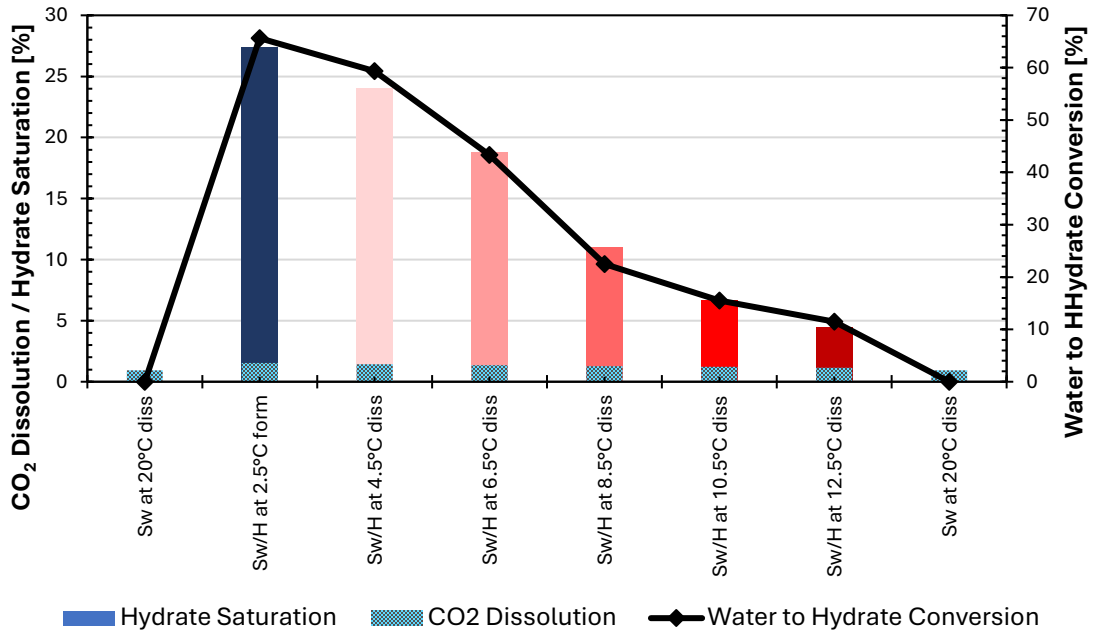

Figure 36: Hydrate saturation, CO_2 solubility-related saturation increase, and water-to-hydrate conversion that were calculated at each temperature step of the fifth experiment's second cycle. Bars represent the calculated hydrate saturation and the portion attributed to dissolved CO_2, while the line (secondary axis) shows the corresponding water-to-hydrate conversion percentages.

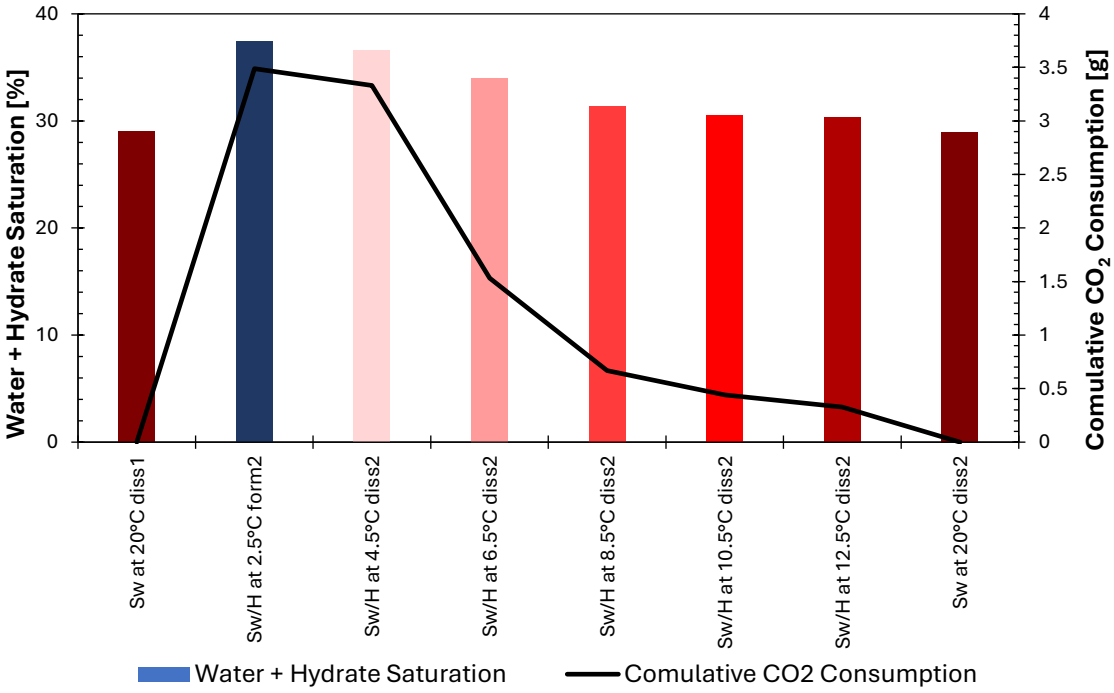

Figure 37: Water + Hydrate saturation [%] in columns, together with the amount of CO2 that was consumed [g] from the hydrate cages (black line) at every stage of the experiment's second cycle.

4.2.6 Sixth Experiment

The sixth and final experiment of this study includes two cycles as well. For the first cycle the hydrate forming method that was utilized was the ramp cooling method during which the temperature was reduced from 12.5 °C to 2.5 °C with a rate of 0.1 °C/h. The second cycle of this experiment include the isothermal method (constant cooling) as the hydrate forming method by directly cooling the system to 2.5 °C. During hydrate dissociation the ramp heating method was employed in both cycles, by increasing the temperature with a rate of 0.1 °C/h. The pressure and temperature data of both cycles are presented in Figure 38, followed by the rest data regarding the CT images (Figure 39, Figure 40, Figure 41 and Figure 42), the permeability measurements (Figure 43 and Figure 44), and the hydrate properties (Figure 45, Figure 46, Figure 47 and Figure 48).

The indication of hydrate formation in the first cycle was detected after 19.5 h since the temperature was stabilized at 2.5 °C. This resulted in a 2.4 bar pressure drop together with a consecutive temperature increase inside the core of 1.4 °C. The pressure curve immediately increased after the initiation of CO_2 injection reaching up to 31.1 bar a few hours after the ramp cooling method started. After that significant increase the pressure remained fairly stable until the system reached close to 6 °C when the pressure started showing an increasing trend until 31.4 bar. A little after the pressure drop due to the hydrate formation was recorded, after which the pressure returned back to 31.5 bar and remained there until the end of the hydrate formation phase. The dissociation process included also the ramping method, during which the temperature was increased to 12.5 °C with 0.1 °C/h before directly going up to 20 °C at the end of the cycle. The pressure curve throughout the entire dissociation stage showed a slight increasing trend. The temperature curve though, started deviating from its linear trend at approximately 6.3 °C, indicating the onset of hydrate dissociation because of the endothermic reaction this process. The deviation lasted for several hours until it got back to its original trend.

In the second cycle hydrates were detected at the induction time that was recorded at 9.5 h. The pressure drop was about 2.1 bar and temperature inside the core was increased by 1.4 °C. The pressure curve even though it returned back to a slightly higher pressure than that before the hydrate formation, it started decreasing even during the first day after hydrates formed. The system remained at the hydrate forming temperature for 4 days and only at the last day the pressure stabilized at 31.2 bar. The dissociation process that was followed was exactly the same as the first cycle with the exact same rate of heating (0.1 °C/h). Again, when the core's temperature went close to 6.3 °C a deviation in the temperature curve appeared, but less gradual which lasted for several hours. The pressure data show a relatively stable condition with some minor fluctuations.

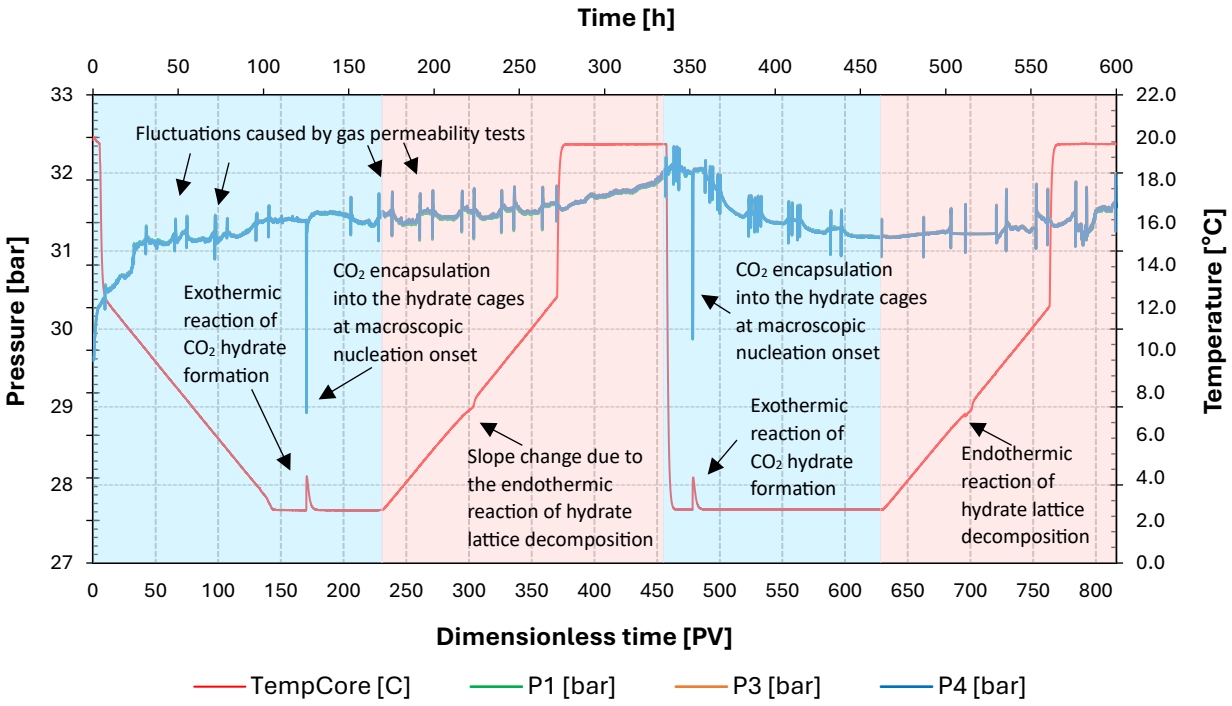

Figure 38: Pressure and temperature profile of the core during CO_2 hydrate formation and dissociation for two cycles of hydrate formation and dissociation for S_w = 28 % of 1 wt% NaCl brine solution. The initial conditions of the experiment are: 29.7 bar and 20 °C. The light blue-colored parts of the graph show the hydrate formation stage of each cycle, whereas the light red-colored parts indicate the dissociation phase of each cycle.

4.2.6.1 CT Imaging Analysis

Figure 39 depicts the dynamic CT images if water/hydrate saturation maps during the brine saturation, the hydrate formation and dissociation process at every step for the first cycle. As the ramp cooling progressed an increase in the average saturation of the core can be identified. Though, the most significant increases are observed close to the inlet of the core (left side) and relatively close to the outlet (right side). After the dissociation of the formed CO_2 hydrates during the first cycle a more uniform distribution of brine can be seen. At Figure 40, again, after the cooling process finished the average saturation of the core appears to have been increased, which decreased gradually as the ramp heating method took place.

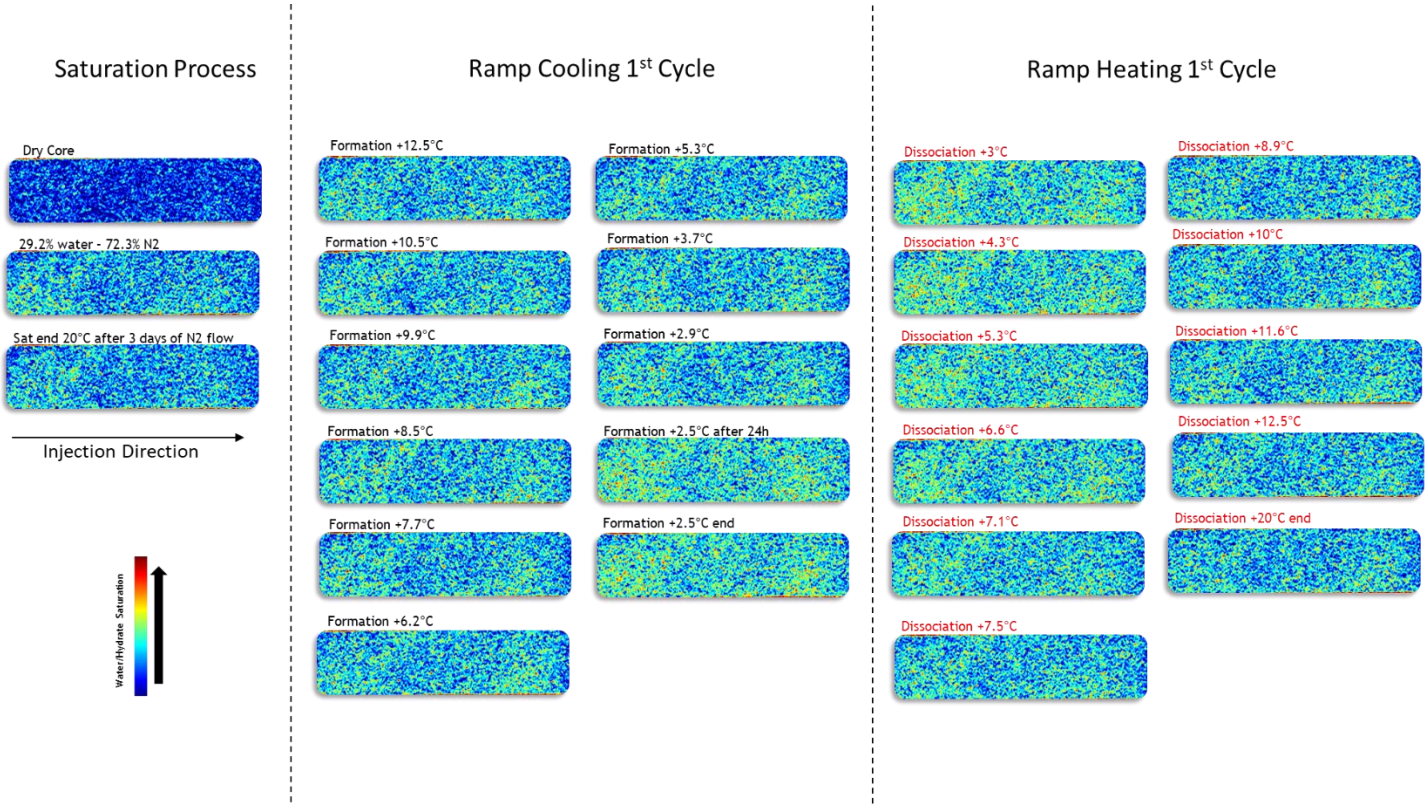

Figure 39: Dynamic CT images of water/hydrate saturation during the brine saturation process of horizontal Bentheimer core as well as during hydrate formation (Ramp Cooling) and dissociation (Ramp Heating). Flow direction is from left to right. (Colors indicate water + hydrate saturation qualitatively. Red: high water/hydrate saturation; green/yellow: intermediate saturation; blue: low saturation).

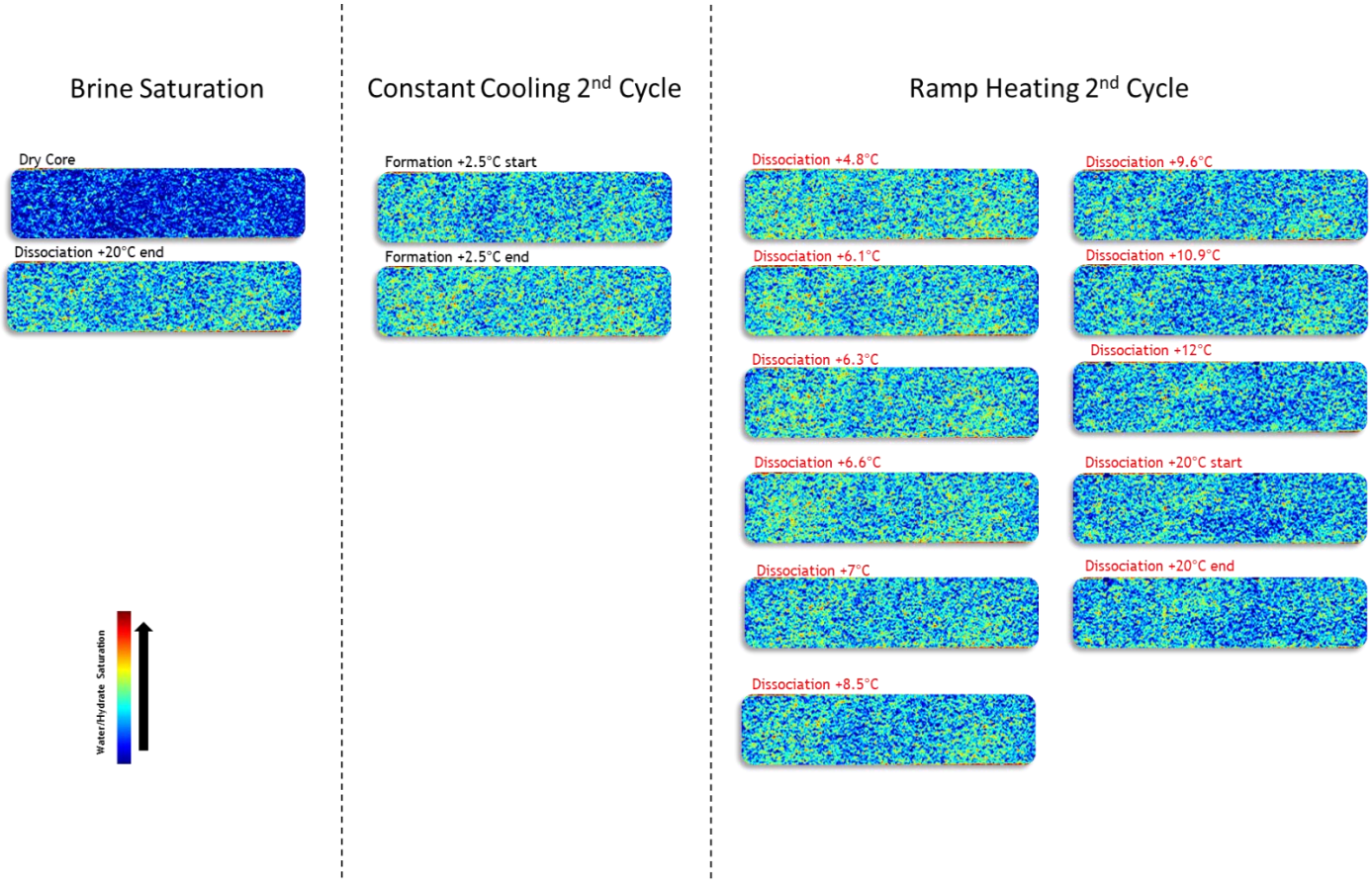

Figure 40: Dynamic CT images of water/hydrate saturation during the brine saturation process of horizontal Bentheimer core as well as during hydrate formation (Ramp Cooling) and dissociation (Ramp Heating). Flow direction is from left to right. (Colors indicate water + hydrate saturation qualitatively. Red: high water/hydrate saturation; green/yellow: intermediate saturation; blue: low saturation).

From the results of the CT images regarding the first cycle (see Figure 41) a small but gradual increase in the average saturation of the core can be observed, leading to a 2 % total increase from the initial saturation at 2.9 °C, just before the hydrate forming temperature of 2.5 °C. The pressure drop that indicated the formation of hydrates appeared when the temperature was at 2.5 °C and as can be seen from the CT image results the average saturation of the core increased sharply to 36.6 % while the core remained for 24 h at that temperature. The core remained at the same temperature for another 24 h which resulted in an increase of only 0.1 % in the saturation of the core. During the phase of ramp heating, the scans taken during the first two temperature show that the overall saturation of the core barely decreased. Only when the temperature was at 5.3 °C and onwards until the scan at the 7.5 °C, the saturation shows a sharp decrease of 4 % total. The rest of the scans until the one taken when the core was at 12.5 °C the saturation decreased by only 0.2 %, indicating that still it was higher by 2.1 % than the initial value. The saturation returned back to its initial value only when the system was heated up to 20 °C for 3 consecutive days.

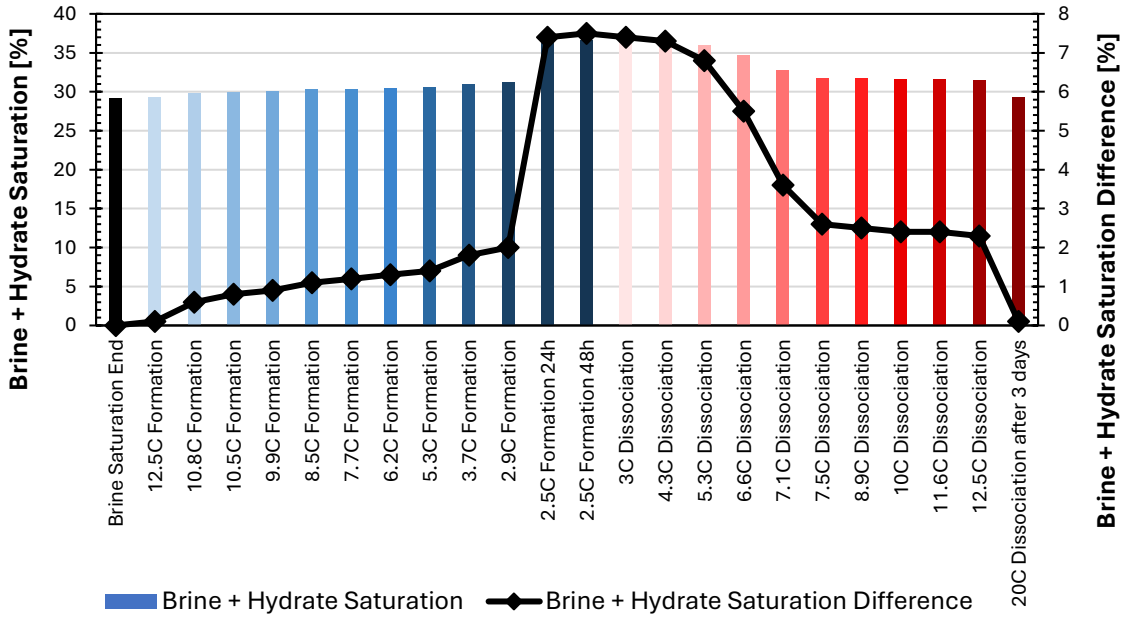

Figure 41: The water plus hydrate saturation is plotted for different stages of the first cycle of the experiment as obtained from the CT images during each of these steps (columns), whereas the water plus hydrate saturation difference from the initial brine saturation at every step is represented with the black curve.

As already mentioned, during the second cycle the CO_2 hydrates were formed by using the constant cooling method to 2.5 °C. From the CT image analysis results in Figure 42 it can be seen that even when the temperature was stabilized at 2.5 °C an increase in the average saturation of the core of more than 2 % is recorded. Then the next scan that was taken a few hours after the pressure drop due to the hydrate formation showed a big increase of 7.3 % in the average saturation of the core from the initial brine saturation value. Afterwards the rest scans that were taken in a four-day period while the system remained at the hydrate forming temperature did not show any significant changes in saturation, apart from some fluctuations around the previously mentioned saturation value. The last scan of the phase of hydrate formation showed a maximum saturation of 37.3 % before starting the ramp heating process. From the CT images during the dissociation phase a quite significant drop can be seen even from the first temperature of 4.8 °C. This decrease in saturation was approximately 1.2 %. The following scan at 6.1 °C (close to the deviation of the temperature curve) showed a similar drop in saturation of 1.3 %. During the deviation of the temperature curve several scans were taken (until 8.5 °C). These scans showed a significant drop in saturation that led to a value of 32.1 %. Then the saturation dropped even further to 30.5 % when the temperature was at 9.6 °C, but after that the decrease was very small until the end of the ramp heating at 12 °C. The remaining 1 % extra that remained disappeared almost entirely while the system was at 20 °C for 12 h and returned back to its initial value after 40 h at that temperature.

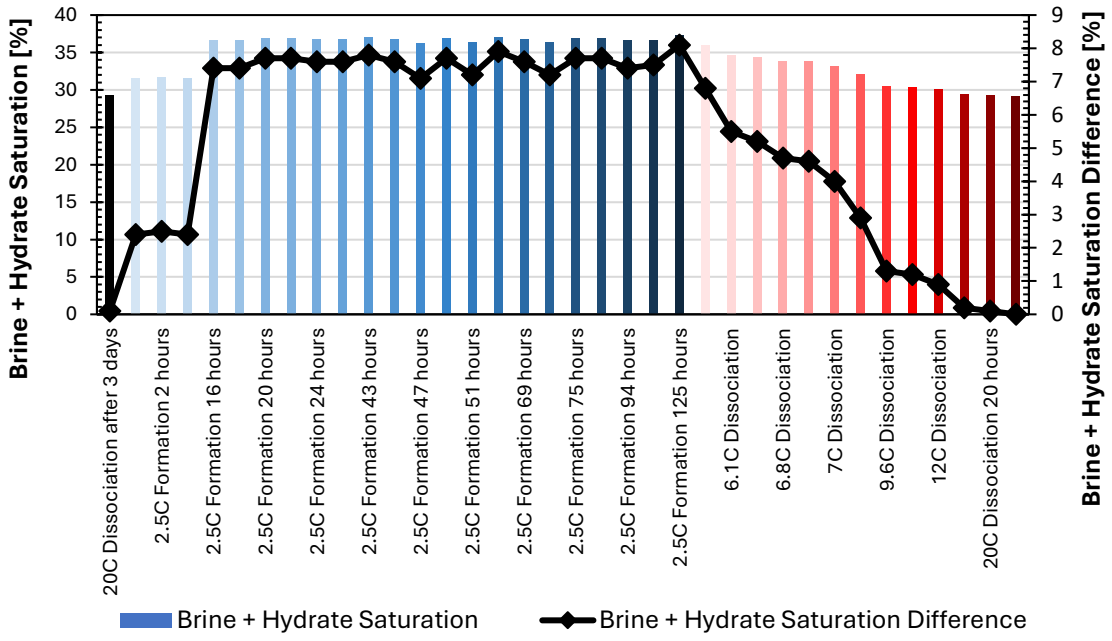

Figure 42: The water plus hydrate saturation is plotted for different stages of the second cycle of the experiment as obtained from the CT images during each of these steps (columns), whereas the water plus hydrate saturation difference from the initial brine saturation at every step is represented with the black curve.

4.2.6.2 Permeability Measurements

The permeability data of the first cycle (Figure 43) show a quite significant decrease in permeability at the beginning of the ramp cooling method at 12.5 °C when compared with the value after the brine saturation process ended. Afterwards as the cooling of the system progressed the reduction in permeability was really small until the temperature of 2.9 °C after which the system reached the hydrate forming temperature and hydrates formed. The first day of hydrate presence inside the core the permeability was measured to be 1.1 D, a number that further decreased to 0.98 D after the second day at 2.5 °C. By having the permeability when only brine was inside the core as a reference point (2.34 D), the permeability was reduced by 58 % because of the formation of hydrates. During ramp heating process the permeability until the temperature of 5.2 °C seems to be increasing slightly. A more significant increase in permeability appears during the temperatures of 6.8 °C and 7.5 °C, by reaching the value of 1.6 D. Later on, the increase continues but in a slower trend as until the end of the ramp heating. After the system is heated up to 20 °C the permeability of the core returns close to the initial value at 2.08 D.

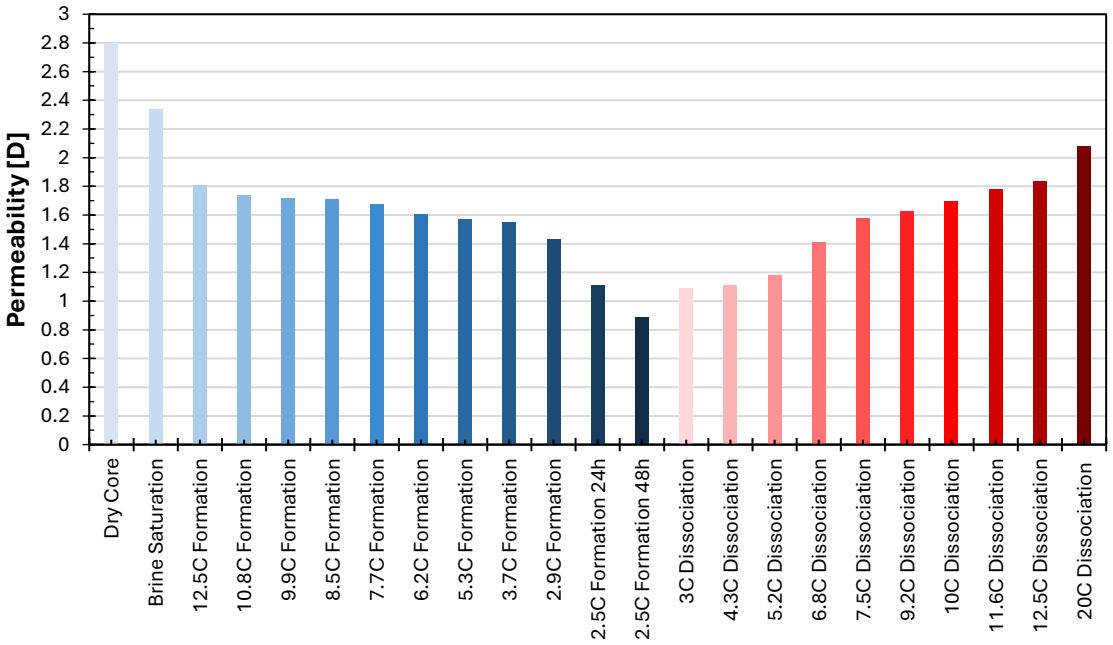

Figure 43: Permeability values of the sand stone core sample during different temperatures of the first cycle of the experiment, as calculated after the implementation of gas permeability tests and Darcy's Law.

The permeability of the core in the second cycle (Figure 44) dropped by 0.4 D after the temperature of the core reached 2.5 °C. At the first measurement after CO_2 hydrates appeared into the core the permeability had been reduced to 1.06 D, almost 50 % lower than the permeability at the end of the first cycle and before the beginning of this cycle. Interestingly, the permeability showed a small increase during the second day at the hydrate forming temperature (2.5 °C) close to 1.2 D, and remained at that value with some fluctuations until the end of the hydrate formation phase of the cycle. The dissociation phase measurements showed that the core's permeability started showing significant increase from the temperature of 6.1 °C until the system was heated up to 9°C. The value of the core's permeability at that temperature accounted for 1.7 D. The next three measurements until the end of the ramp heating method indicated a small increase in permeability to 1.8 D. For one more time the permeability got close to its initial value after the system was at 20 °C for 10 h.

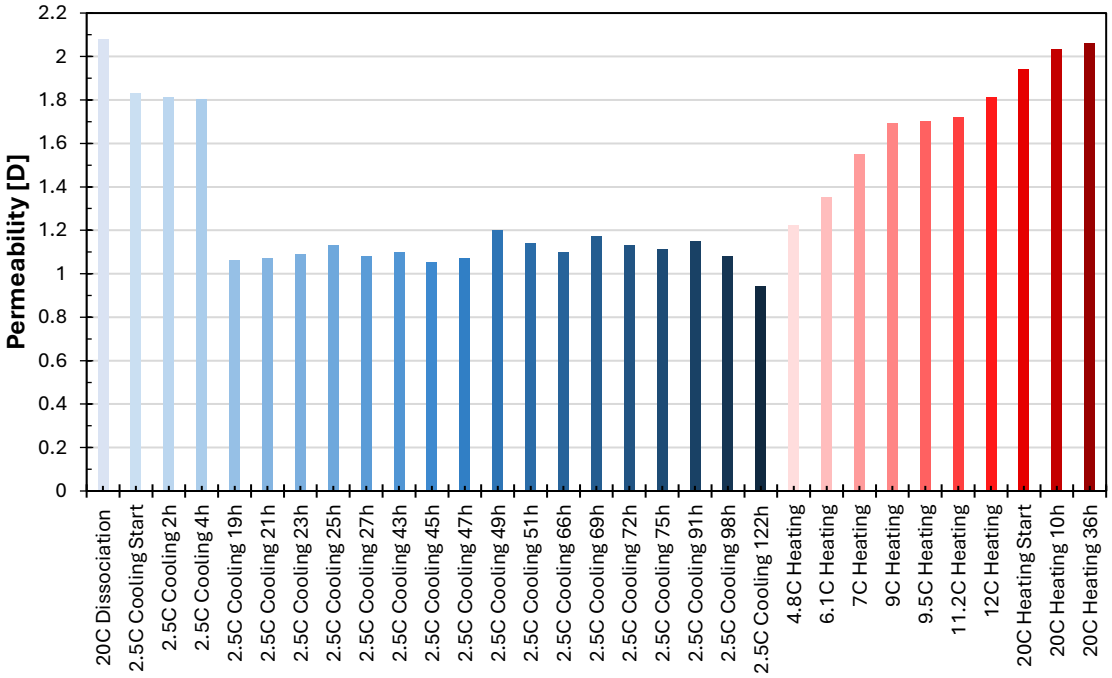

Figure 44: Permeability values of the sand stone core sample during different temperatures of the second cycle of the experiment, as calculated after the implementation of gas permeability tests and Darcy's Law.

4.2.6.3 Hydrate Properties Calculations

For this cycle the gathered data of both the processes of formation and dissociation were closer to the Modified Kozeny Carman empirical model and thus they are fitted on it in order to correct the hydrate saturation values as well as the rest of the calculated parameters that are going to be presented below.

The results of the calculations (see Figure 45) indicated that when the hydrate formation process was finished the saturation of hydrates accounted for 27.7 %. At the same time 80 % of the existing water inside the core sample was converted into hydrates. Additionally, the amount of CO_2 that was consumed from the hydrate cages was roughly 4 g in total. It has to be noted that Figure 46 shows a CO_2 consumption during the cooling process around 0.2 g until the measurement when the temperature was 7.7 ^oC after which the CO_2 consumption increases even further with a different trend. By looking at the saturation increase caused by the dissolution of CO_2 until the aforementioned temperature, we could conclude that this small amount of consumed CO_2 is actually dissolved CO_2. At the next temperatures, specifically from 6.2 ^oC onwards the hydrate saturation appears higher than the saturation increase caused by the CO_2 dissolution, and together with that the water to hydrate conversion starts increasing more significantly as well. An indication that a small number of hydrates exist in the core before reaching the lowest temperature. It has to be noted that from 6.2 ^oC onwards the system has entered the hydrate stability zone.

In fact, the swelling of water that is caused from the CO_2 dissolution into it shows small saturation increase and permeability decrease. These changes in saturation and permeability affect the calculations of hydrate properties. During the dissociation process the saturation of CO_2 hydrates

appears to be dropping even from the first three heating steps (5.2 °C) to almost 22 %. The biggest drop is seen when the temperature reached 6.6 °C and the hydrate saturation decrease continues with a quite steep slope until 10 °C, after which the hydrate saturation decreases slightly until the end of the ramp heating method. The remaining amount of hydrates at the end of the ramp heating accounts for 6.5 %. Complete dissociation is achieved when the temperature was increased up to 20 °C and remained there for 3 days.

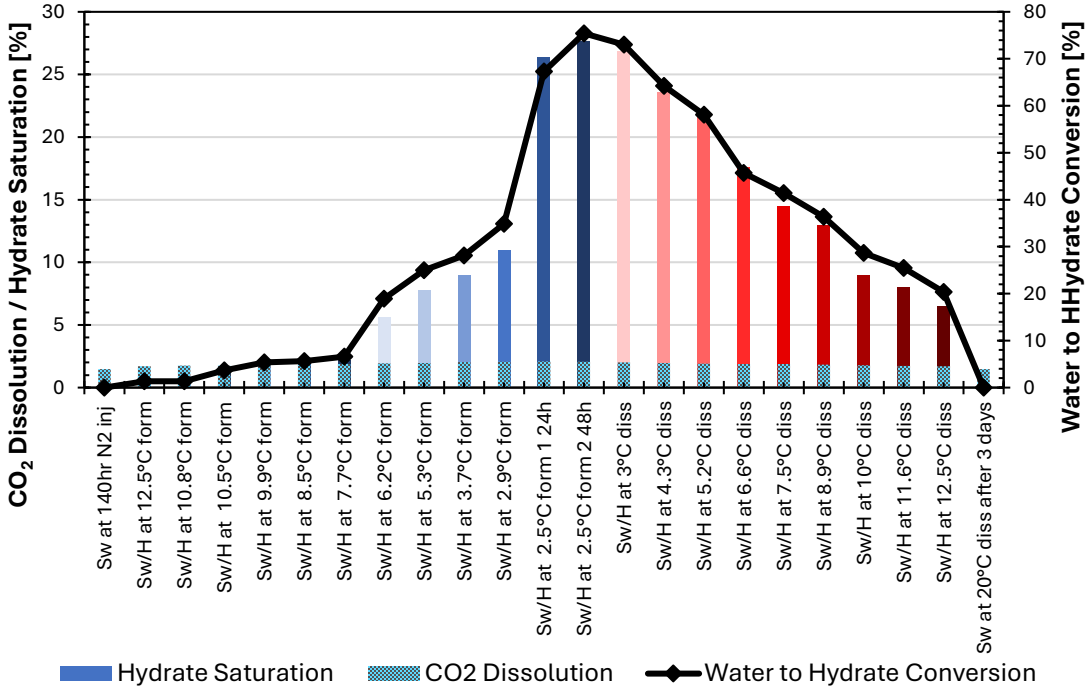

Figure 45: Hydrate saturation, CO_2 solubility-related saturation increase, and water-to-hydrate conversion that were calculated at each temperature step of the sixth experiment's first cycle. Bars represent the calculated hydrate saturation and the portion attributed to dissolved CO_2, while the line (secondary axis) shows the corresponding water-to-hydrate conversion percentages.

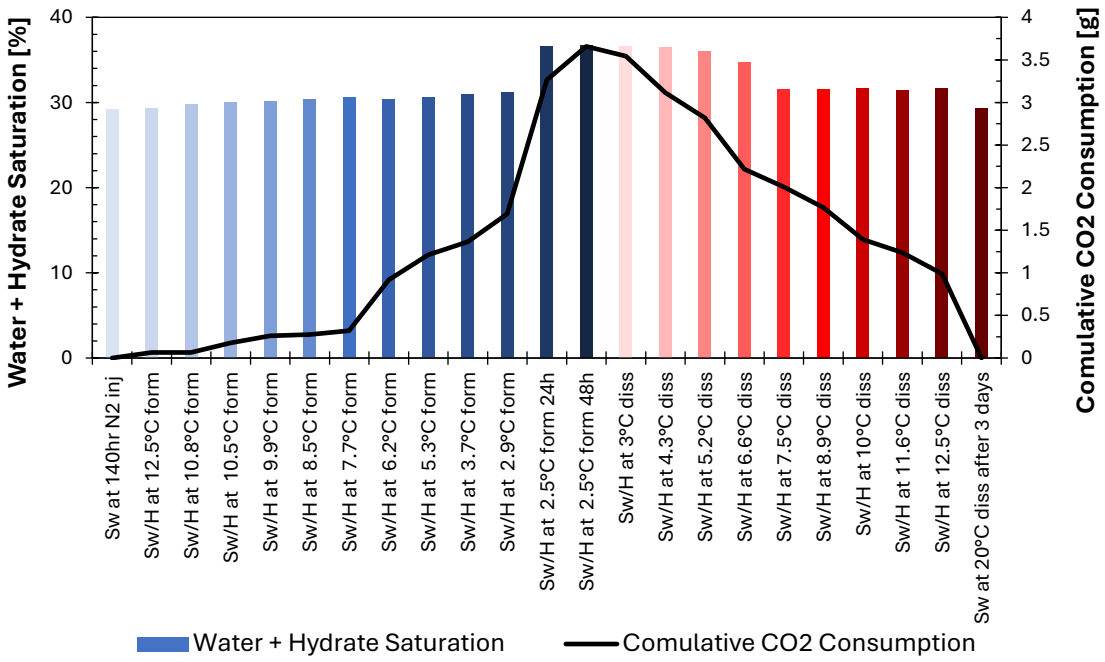

Figure 46: Water + Hydrate saturation [%] in columns, together with the amount of CO2 that was consumed [g] from the hydrate cages (black line) at every temperature change throughout the first cycle of the experiment.

The normalize permeability data versus the hydrate saturation results of the second cycle of this experiment were plotted, and they fit best the Kozeny Grain (Grain-coating) empirical model. Based on that model the hydrate saturation values were corrected and were used to produce the following hydrate properties graphs that are presented below.

The results of the calculations indicated in Figure 47 that when the hydrate formation process was finished the saturation of hydrates accounted for 25.3 %. At the same time 67 % of the existing water inside the core was converted into hydrates. Additionally, the amount of CO_2 that was consumed from the hydrate cages was 3.2 g in total, as observed in Figure 48. It has to be noted that the indication of hydrate formation appeared after 18 h since the core was at 2.5 ^{o}C, and the system remained at that temperature for a total of 125 h (approximately 5 days). When the hydrates first appeared the hydrate saturation value was calculated to be 23 %. During these five days no significant changes were recorded in any of the gathered data apart from some small fluctuations, probably due to some error that is included in the measurements since any changes in the saturation and permeability measurements affect the calculation of the hydrate properties. During the dissociation process the saturation of CO_2 hydrates shows a small drop of 5 % until the measurement that was taken when the temperature was 6.1 ^{o}C, just a few hours before the deviation in the temperature curve was recorded. Afterwards, the biggest drop is seen in the next two measurements at 7 ^{o}C and 8.5 ^{o}C, with the main decrease of 8 % happening during the latter. The following temperatures showed a smaller but quite significant drop ranging from 2 to 3 % until the end of the ramp heating method at 12 ^{o}C, where the saturation of hydrates was roughly 2 %. This remaining amount of hydrates reduced in half after the system was at 20 ^{o}C for 12 h and completely disappeared at the last measurement after 40 h at that temperature.

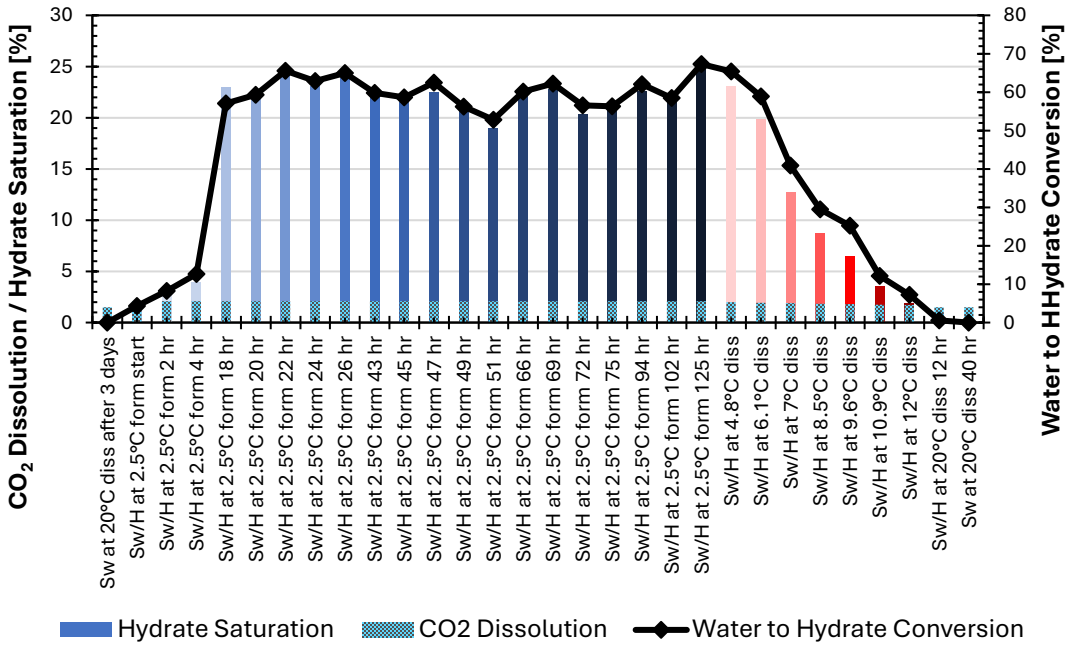

Figure 47: Hydrate saturation, CO_2 solubility-related saturation increase, and water-to-hydrate conversion that were calculated at each temperature step of the sixth experiment's second cycle. Bars represent the calculated hydrate saturation and the portion attributed to dissolved CO_2, while the line (secondary axis) shows the corresponding water-to-hydrate conversion percentages.

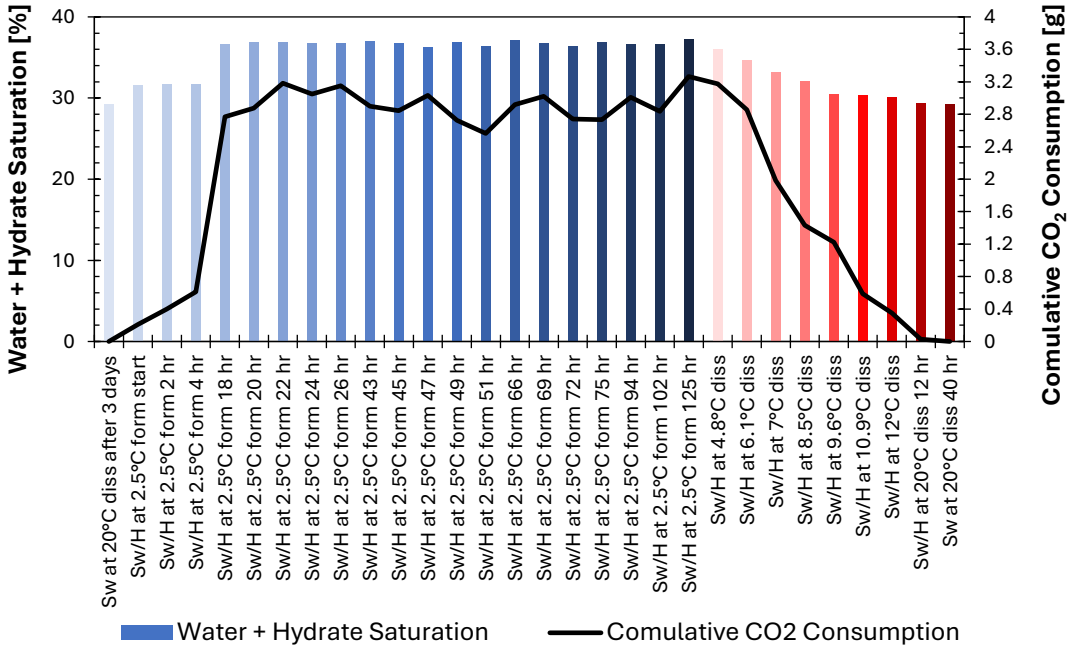

Figure 48: Water + Hydrate saturation [%] in columns, together with the amount of CO_2 that was consumed [g] from the hydrate cages (black line) at every temperature change throughout the second cycle of the experiment.

4.3 Key Observations and Discussion

In this section the key observations are going to be discussed regarding the thermodynamic conditions, kinetics of hydrate, and hydrate properties between all the previously mentioned experimental results. The main aim of this assessment is to identify the impact of subcooling as a driving force and hydrate formation/dissociation methods on the kinetics of hydrate including nucleation and growth.

4.3.1 Thermodynamic conditions

By looking at the pressure and temperature profiles during all processes of hydrate formation and dissociation for all the conducted experiments there is information that can be identified for kinetics evaluation including the induction time, the amount of pressure-drop, and the degrees of temperature increase that were recorded during all the hydrate formation processes. Between experiments in which the same cooling method was used, the induction time occurred sooner the higher the subcooling was. For example, the first three experiments (Experiment 1, 2 and 3) and the second cycles of the last two experiments (Experiment 5 and 6) that used the isothermal method (direct cooling) showed this behavior. Additionally, it appears that the method of forming hydrates affects the inductions time. The smallest induction times appeared during the experiments that used the isothermal method (rate of cooling, 2 °C/h), then came the experiment with the step cooling method (interval ramp of 3.5 °C), and the longest time appeared at the experiment with the ramp cooling (0.1 °C/h) method. It has to be noted though that the step cooling method with smaller temperature interval (more steps) showed a significant effect on induction time for hydrate formation, and apparently it required more time for hydrate nucleation.

Table 5: The induction time, pressure-drop, and temperature increase that were recorded in every experiment/cycle during the hydrate formation phase:

Experiment	Induction Time [h]	Pressure Drop [bar]	Temperature Increase [°C]	Subcooling [°C]
First Experiment	3.5	1.2	1.8	6
Second Experiment	23	3.9	1.8	4
Third Experiment	0.17	0.2	1.6	10
Fourth Experiment	50	2	1.2	4.5
Fifth Experiment First Cycle	-	-	-	4.5
Fifth Experiment Second Cycle	8.5	3.8	2.1	4.5
Sixth Experiment First Cycle	64.5	2.4	1.4	4.5
Sixth Experiment Second Cycle	9.5	2.1	1.4	4.5

Regarding Table 5 the biggest pressure-drop at onset of macroscopic hydrate nucleation corresponded to the lowest degree of subcooling (4 degrees). The second cycles of fifth and sixth experiments (4.5 degrees of subcooling) showed smaller pressure drops with a significant difference between them, but both higher than the first experiment (6 degrees of subcooling). The lowest pressure drop is seen at the third experiment (10 degrees of subcooling). So, the higher

the subcooling the lower the pressure drop is. Finally, as for the temperature increase that was caused by the hydrate formation exothermic reaction, no clear pattern can be identified neither about the effect of the degree of subcooling nor about the effect of method.

Regarding the dissociation of CO_2 hydrates, due to the dynamic nature of all the experiments with constant CO_2 flow inside the core until the end of each experiment, the general trend of the pressure curve cannot be used to extract solid conclusions about this phase. It appears that in almost all of the experiments the pressure curve is affected by the temperature changes due to the heating dissociation processes. Because of the dynamic conditions and the constant flow of CO_2 inside the system, the temperature increase could have caused the CO_2 gas to expand. So, instead of showing a decreasing trend because of the dissociation of hydrates (more free pores inside the core) they appear to generally increase as if they 'follow' the temperature increase. But, apart from that, some interesting observations were made regarding the temperature data curve in every experiment. More specifically, in each cycle a change in the trend of the temperature curve appeared between 6.2 °C and 6.3 °C no matter how hydrates were formed and the degree of subcooling or the method of hydrate dissociation. This change in trend can be attributed to the fact that a big number of hydrates dissociated when the core sample reached that temperature and thus the endothermic reaction causing this 'delay' for the temperature to reach its intended value. Even more, this temperature is lower than the equilibrium line temperature of the hydrate stability zone (7 °C), indicating that the porous medium slightly and depending on the pore size can inhibit hydrate formation.

4.3.2 CT Imaging Data

Since this study aims to investigate the kinetics of CO_2 hydrates dissociation, the CT imaging measurements are going to be discussed in this subsection by having key points of reference: the end of hydrate growth end when the conditions reach a steady state, the macroscopic onset of hydrate dissociation, and the end of the heating (either ramping or stepwise method).

Table 6: Representation of the core's average saturation change at five different stages of each experiment as it was calculated from the available CT scans. Temp [°C], indicates the temperature that the core had at each of the five stages. ΔS [%], shows the saturation difference from the initial brine saturation that was achieved in every experiment. Time [h], is only shown in the four dissociation stages, and shows the number of hours from the end of the hydrate formation phase until the time when each measurement (CT scan) was taken.

Experiment	End of Hydrate Growth		Before Onset of Hydrate Dissociation			After Onset of Hydrate Dissociation			End of Step/Ramp Process			End of Dissociation		
	Temp [°C]	ΔS [%]	Temp [°C]	Time [h]	ΔS [%]	Temp [°C]	Time [h]	ΔS [%]	Temp [°C]	Time [h]	ΔS [%]	Temp [°C]	Time [h]	ΔS [%]
Experiment 1	1	-	-	-	-	-	-	-	-	-	-	-	-	-
Experiment 2	3	-	-	-	-	-	-	-	-	-	-	-	-	-
Experiment 3	-3	9.4	4.5	25	7.7	8.3	45	2.1	12	95	1.9	18.5	105	0
Experiment 4	2.5	6.5	5.5	50	5.1	8.5	85	2	10	100	1.5	20	110	0.9
Experiment 5 1st Cycle	-	-	-	-	-	-	-	-	-	-	-	-	-	-
Experiment 5 2nd Cycle	2.5	8.4	4.5	48	7.6	8.5	105	2.4	12.5	160	1.3	20	230	0
Experiment 6 1st Cycle	2.5	7.5	5.3	28	6.8	8.9	66	2.5	12.5	101	2.3	20	173	0
Experiment 6 2nd Cycle	2.5	8.1	4.8	23	6.7	8.5	62	2.8	12	97	0.8	20	137	0

Since the first two experiments were conducted at the setup that could not be scanned with the CT scanner the first two rows of Table 6 appear empty. However, in the experiments where data was available, Experiment 3 achieved the greatest water + hydrate saturation increase (9.4 % total increase), likely benefiting from the fact that hydrates were formed under the highest degree of subcooling that was examined in this study (10 ^{o}C). Despite the same formation temperature, the method of cooling seems to have influenced the resulted maximum increase in water + hydrate saturation because it looks from the results that the isothermal cooling method achieved higher saturation increase than step and ramp cooling. However, it is important to consider that the differences observed in maximum water + hydrate saturation between cooling methods might be affected more by variations in the initial brine saturation or not completely uniform distribution of brine inside the core samples. For instance, Experiment 4, which showed the lowest increase (6.5 %) appeared to have a layered core sample with a high permeable zone where most of the brine was accumulated. This localized accumulation could have impacted the overall measured saturation.

During the dissociation Figure 49 clearly shows that faster heating rates led to more rapid initial reductions in water + hydrate saturation. In contrast, slower heating rates (step heating) resulted in more gradual decrease in water + hydrate saturation over a longer period. After reaching the onset of hydrate dissociation, most experiments showed a consistent decrease, with Experiment 3 standing out due to its overall faster heating (each temperature step lasted only a few hours before moving to the next one with 1.5 ^{o}C interval) and more rapid decline towards zero water + hydrate saturation difference. The results also indicate that extend temperature holds, such as the plateau observed in Experiment 3 between 50 and 100 h (only one temperature step occurred that lasted for 2 days) resulted in slight additional dissociation, demonstrating that higher heating rates of temperature increase are more effective in achieving more dissociation than prolonged exposure to elevated temperatures. Complete dissociation generally required a final step to approximately 20 ^{o}C, and it can be seen from the results that if the final step was not sustained long enough, full hydrate breakdown was not achieved. Experiment 4 is a clear example, where the water + hydrate saturation did not become equal to the initial water saturation.

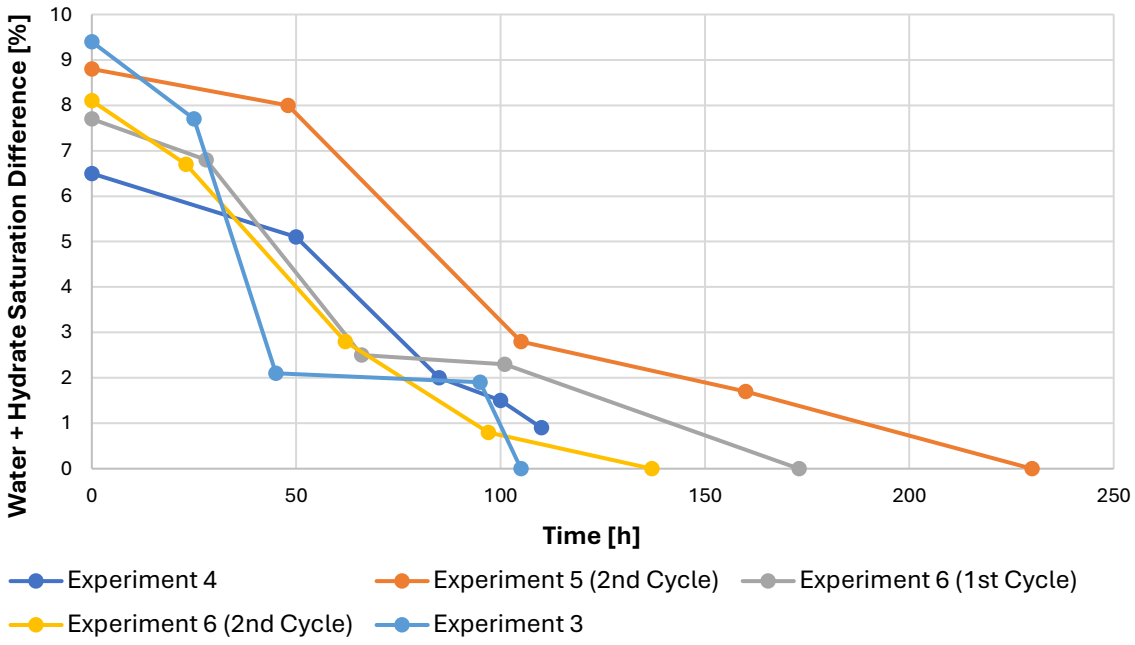

Figure 49: Rate of hydrate dissociation presented as water + hydrate saturation over time as obtained from the analysis of the CT images for five different cycles of hydrate formation and dissociation.

4.3.3 Permeability Data

The permeability measurements that were obtained from the gas permeability tests during the last three experiments are going to be discussed.

Table 7: Representation of the core's permeability change at five different stages of each experiment as it was calculated from gas permeability tests. Temp [°C], indicates the temperature that the core had at each of the five stages. Δk [D], shows the permeability difference of the core after brine saturation phase minus the permeability after hydrate formation was achieved. But for the dissociation Δk [D] is the difference from the value after the end of hydrate formation. Time [h], is only shown in the four dissociation stages, and shows the number of hours from the end of the hydrate formation phase until the time when each measurement (gas permeability test) was performed.

Experiment	End of Hydrate Growth		Before Onset of Hydrate Dissociation			After Onset of Hydrate Dissociation			End of Step/Ramp Process			End of Dissociation		
	Temp [°C]	Δk [D]	Temp [°C]	Time [h]	Δk [D]	Temp [°C]	Time [h]	Δk [D]	Temp [°C]	Time [h]	Δk [D]	Temp [°C]	Time [h]	Δk [D]
Experiment 1	1	1.54	-	-	-	-	-	-	-	-	-	-	-	-
Experiment 2	3	1.31	-	-	-	-	-	-	-	-	-	-	-	-
Experiment 3	-3	1.7	-	-	-	-	-	-	-	-	-	-	-	-
Experiment 4	2.5	1.15	5.5	50	0.26	8.5	85	0.77	10	100	0.86	20	110	1.01
Experiment 5 1st Cycle	-	-	-	-	-	-	-	-	-	-	-	-	-	-
Experiment 5 2nd Cycle	2.5	1.25	4.5	48	0.2	8.5	105	0.84	12.5	160	0.94	20	230	1.16
Experiment 6 1st Cycle	2.5	1.26	5.3	28	0.29	8.9	66	0.74	12.5	101	0.95	20	173	1.19
Experiment 6 2nd Cycle	2.5	1.14	4.8	23	0.28	8.5	62	0.76	12	97	0.91	20	137	1.07

During hydrate formation, a clear relationship emerged where greater subcooling consistently resulted to a more pronounced permeability reduction. Experiment 3, experiencing the highest subcooling (10 ^{o}C) exhibited the largest permeability decrease. This was followed by Experiments 1 and 2 which had 6 ^{o}C and 4 ^{o}C subcooling respectively. In contrast Experiments 4, 5 and 6, all conducted under the same 4.5 ^{o}C degrees of subcooling regardless the cooling method that was used (isothermal, step or ramp), displayed similar permeability reductions. These results indicate that the degree of subcooling, rather than the particular cooling method used, was the predominant factor influencing permeability loss during the hydrate formation stage. However, it is also important considering that differences in observed maximum saturation increase (as discussed previously) and thus permeability reduction might not solely be attributed to the cooling method, but potentially to variations in the initial brine saturation and its distribution along the core samples. Also, Experiment 4, for example, which had the high permeable layer inside the core could have affected in the lowest permeability reduction as observed from the results.

The dynamic permeability recovery during dissociation, visually represented in Figure 50, generally followed similar patterns across experiments. The initial permeability recovery that is observed before the onset of hydrate dissociation ranged between 23 % and 25 % except from Experiment 5 (2nd Cycle) which showed only 15 % recovery, likely due to fewer heating steps during that period. The graph illustrates that faster heating led to faster permeability recovery. After the onset of hydrate dissociation almost all experiments had recovered approximately 70 % of their lost permeability. The exception was Experiment 6 (1st Cycle) which had recovered almost 60 % of the impaired permeability. This observation could probably be attributed to the different method of hydrate formation as in this experiment the ramp cooling method (0.1 ^{o}C/h) was used. At the end of the step/ramping processes the permeability recovery reached between 75 % and 80 %, and even after the end of dissociation at 20 ^{o}C complete permeability was not achieved in any of the experiments. A persistent residual permeability loss of 8 % to 10 % was observed, which could be attributed to factors such as water trapping within the pores, particle migration within the porous medium, or structural changes within the core material induced during the hydrate formation and dissociation cycles.

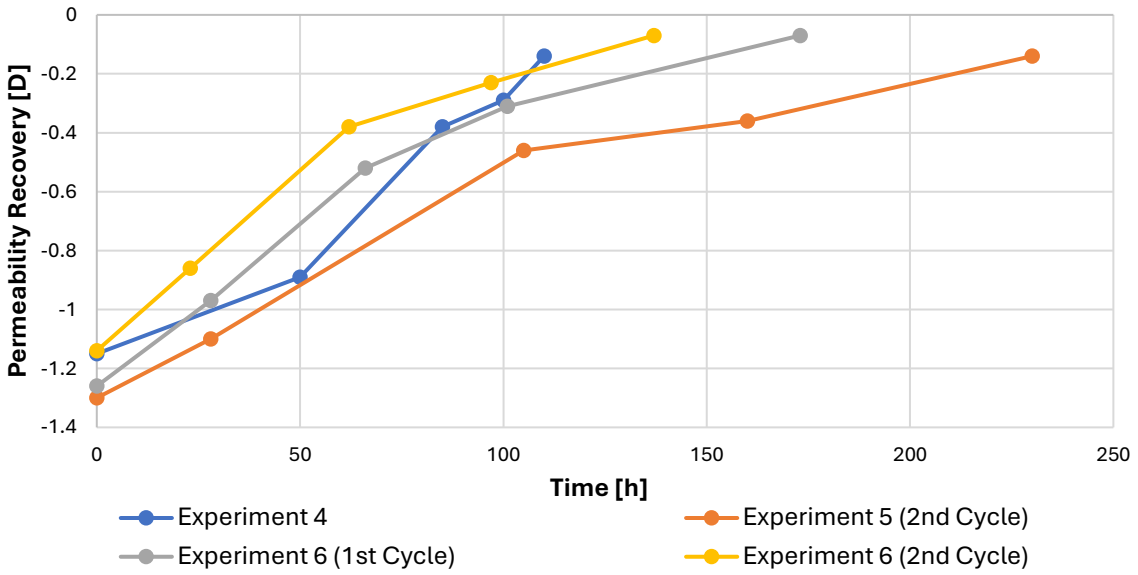

Figure 50: Dynamic permeability recovery during hydrate dissociation.

In the hydrate formation graph (Figure 51) the permeability measurements of the gas permeability tests are presented for the four experiments that had the same hydrate forming temperature (2.5 ^{o}C). It is evident that as hydrate formation progresses permeability decreases. The power-law function describes a process where the dependent variable (permeability) decreases, but the rate of decrease diminishes over rime, which perfectly aligns with the physical phenomenon of hydrate formation. As hydrates begin to form, they rapidly block larger leading to a sharper initial drop in permeability. Experiment 4 stood out with the highest initial permeability and slowest rate of decline. This observation is attributed to the unique properties of the core that was used. This core appeared to be layered (not laminated) and had a high-permeable zone where brine and thus hydrates accumulated (see Figure 19), and for that reason its data points were excluded from the master curve that was obtained from the included cycles in Figure 51. Experiment 6 (2nd cycle) shows a more moderate decrease but with more scatter. This due to the fact that after hydrate formation, which occurred before 20 h, the system was kept at the hydrate forming temperature for four more consecutive days potentially allowing more redistribution, or structural changes that caused this variability. Also, measurement noise is very likely to have caused this scattering from 40 hours onward. The other two experiments show a very similar trend as the previously discussed experiment, indicating that the method of cooling did not affect the permeability impairment due to hydrate formation.

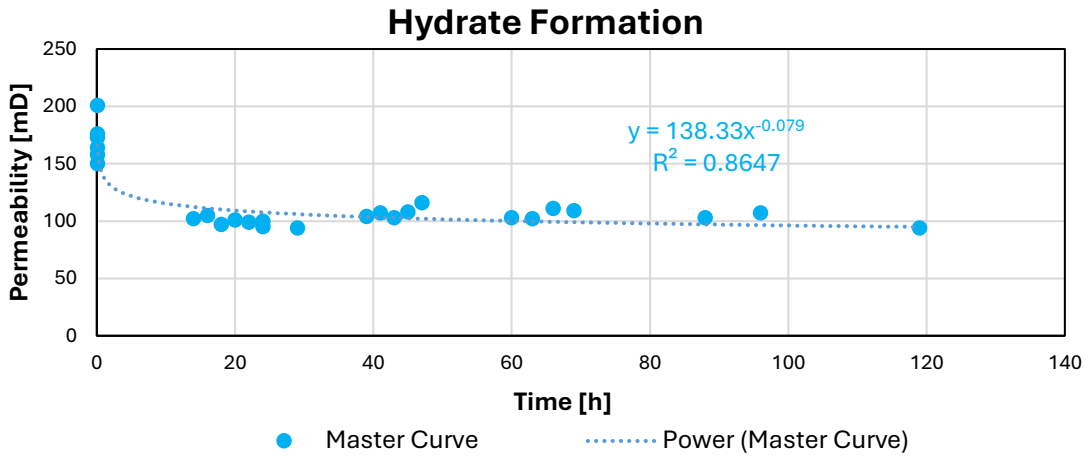

Figure 51: Dynamic permeability reduction during cooling process.

Similarly, in Figure 52 the permeability measurements of the gas permeability tests for the same four experiments during the dissociation process are presented. Again, the trend fits a power-law function, with permeability increasing more rapidly as soon as the temperature of the onset of dissociation is reached. The high R^2 value can confirm the suitability of the power-law function for describing the permeability recovery kinetics, but in comparison with the hydrate formation master curve the value of R^2 is lower. Experiment 4 again stands out from the rest cycles, and its data points are excluded from the master curve determination. Experiment 6 (2nd cycle) also, appears to show a faster permeability recovery than the remaining two experiments as it has the higher exponent between them, despite the fact that during this cycle the system remained at the hydrate forming temperature for significantly more days than the others. The slowest recovery appears during Experiment 6 (1st cycle), probably indicating that the slow and controlled constant cooling rate (0.1 °C/h) resulted in more stable hydrates that are more difficult to dissociate. So, these differences might have affected the dissociation rates and thus the permeability recovery data points are more scattered.

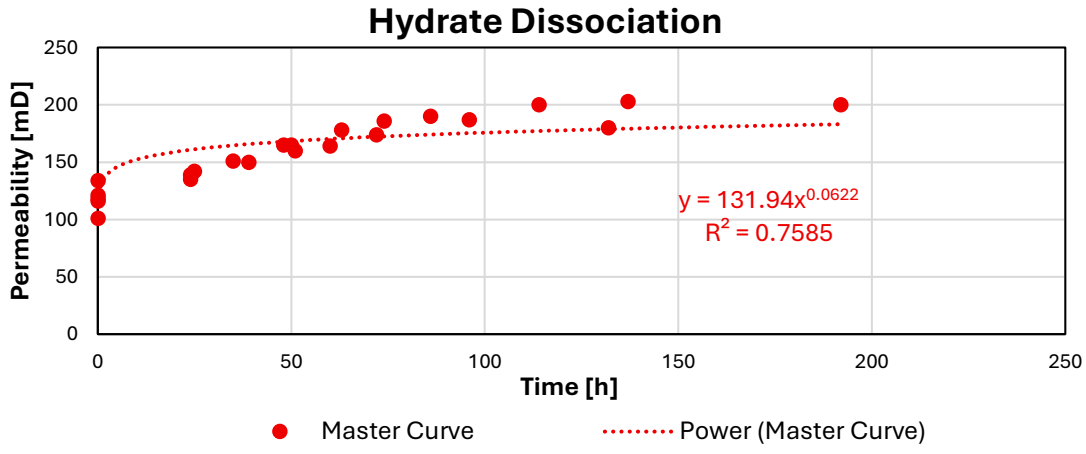

Figure 52: Dynamic permeability recovery during heating process.

4.3.4 Hydrate Saturation

The hydrate saturation results which are going to be discussed, are calculated based on the CT/PT data and gas permeability measurements.

Table 8: Representation of the core's average hydrate saturation change at five different stages of each experiment as it was calculated from the available CT scans and gas permeability tests. Temp [°C], indicates the temperature that the core had at each of the five stages. S_h [%], shows the hydrate saturation value. Time [h], is only shown in the four dissociation stages, and shows the number of hours from the end of the hydrate formation phase until the time when each measurement (CT scan and gas permeability test) was taken.

Experiment	After Hydrate Formation		Before T Curve Deviation			After T Curve Deviation			End of Step/Ramp Heating			End of Dissociation		
	Temp [°C]	Sh [%]	Temp [°C]	Time [h]	Sh [%]	Temp [°C]	Time [h]	Sh [%]	Temp [°C]	Time [h]	Sh [%]	Temp [°C]	Time [h]	Sh [%]
Experiment 1	1	-	-	-	-	-	-	-	-	-	-	-	-	-
Experiment 2	3	-	-	-	-	-	-	-	-	-	-	-	-	-
Experiment 3	-3	34.1	-	-	-	-	-	-	-	-	-	-	-	-
Experiment 4	2.5	16.5	5.5	50	12.3	8.5	85	3.3	10	100	3	20	110	1.1
Experiment 5 1st Cycle	-	-	-	-	-	-	-	-	-	-	-	-	-	-
Experiment 5 2nd Cycle	2.5	27.5	4.5	48	24	8.5	105	11	12.5	160	4.5	20	230	0
Experiment 6 1st Cycle	2.5	27.7	5.3	28	21.7	8.9	66	13	12.5	101	6.5	20	173	0
Experiment 6 2nd Cycle	2.5	25.3	4.8	23	23	8.5	62	8.7	12	97	1.9	20	137	0

The results regarding the formation of hydrates demonstrate a clear relationship between subcooling and hydrate saturation. Greater subcooling leads to higher hydrate saturation, as best explained in Experiment 3 which achieved the highest saturation under the lowest temperature conditions. For the experiments that were conducted under the same hydrate forming temperature at 2.5 °C (Experiment 4, 5, and 6) showed very similar hydrate saturations indicating that the cooling method that was utilized did not affect the amount of hydrate formation. Experiment 4 is an exception again, and showed a considerably lower hydrate saturation, but this can be attributed to the fact that the core used was not laminated.

During dissociation, and as observed in Figure 53, the estimated rates at which hydrates dissociated varied among the experiments. Before the onset of hydrate dissociation, Experiment 6 (1st Cycle) shows a steeper hydrate saturation decrease than the rest of the experiments which could be attributed the method used for hydrate formation (ramp cooling 0.1 °C). Its trend remained almost the same until the end of the ramp heating process, indicating that the constant thermal increase even at a slow rate resulted in almost the same dissociation rate throughout the ramp heating. Conversely, at Experiment 6 (2nd Cycle) even though the dissociation rate was not as steep at the beginning, from the onset of hydrate dissociation until the end of the ramp heating process the hydrate dissociation rate was very steep leading very few remaining hydrates. Probably another indication that hydrate forming method (isothermal in the last cycle) played a role in this observation. Experiment 5 (2nd Cycle) which had the slowest temperature increase (Step heating) needed significantly more time to achieve complete dissociation, because it was observed that most of the hydrate dissociation appeared during the transition from one temperature step to another rather than maintaining the temperature of each step for a long time.

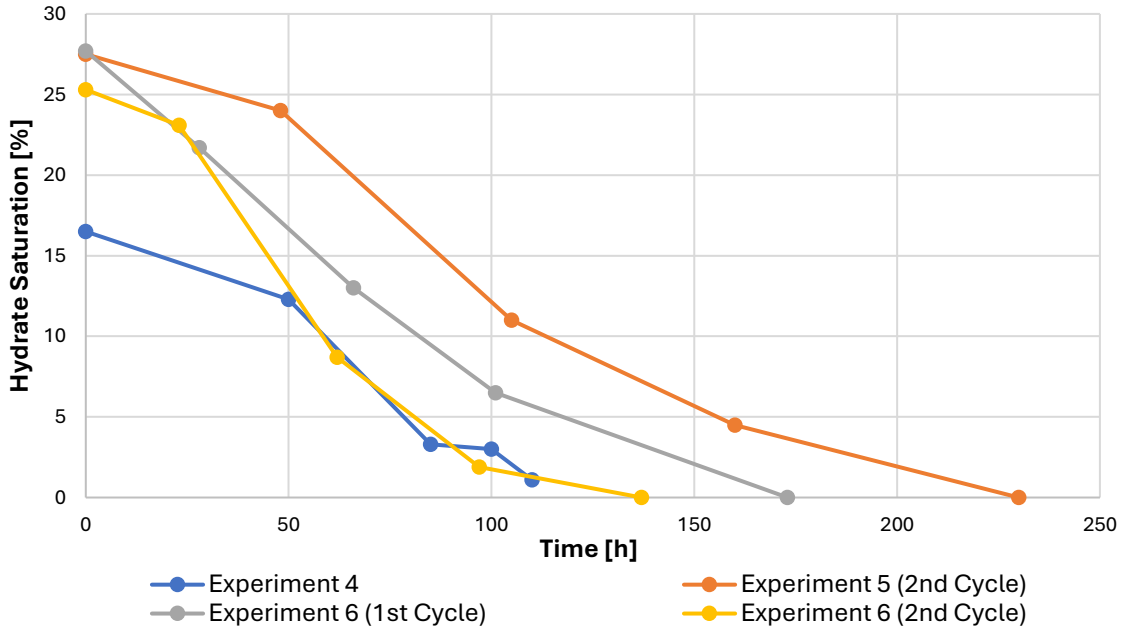

Figure 53: Estimation of the rate of hydrate saturation based on the dynamic permeability change.

Below in Figure 54 the original permeability data are presented in the form of the normalized permeability (k/k_0) versus the hydrate saturation (S_h), whereas in Figure 55 the corrected values of hydrate saturation are plot versus the same normalized permeability data. This correction was achieved by fitting the permeability data into the empirical model's equation that they fitted best. It is observed that the curve of the experiments that utilized the direct cooling and ramp cooling methods for hydrate (Experiment 5 2nd Cycle and Experiment both Cycles) formation fitted better to the Kozeny Grain (Grain-Coating). The experiments that used the step cooling method (Experiment 4 and Experiment 5 1st Cycle) fitted better to the Modified Kozeny Carman model. Also, the dissociation curve in all experiments seemed to follow the same curve as the formation of the same cycle. Probably the hydrate forming method plays a role in the context of how fast or slow the hydrate forming temperature is reached. The Kozeny Grain (Grain-Coating) model fitted better the experiments where the hydrate forming temperature was reached with a constant rate of cooling either big (direct cooling) or slower (constant cooling), whereas the Modified Kozeny Carman model fitted better the experiments where the hydrate forming temperature was reached slower and in steps.

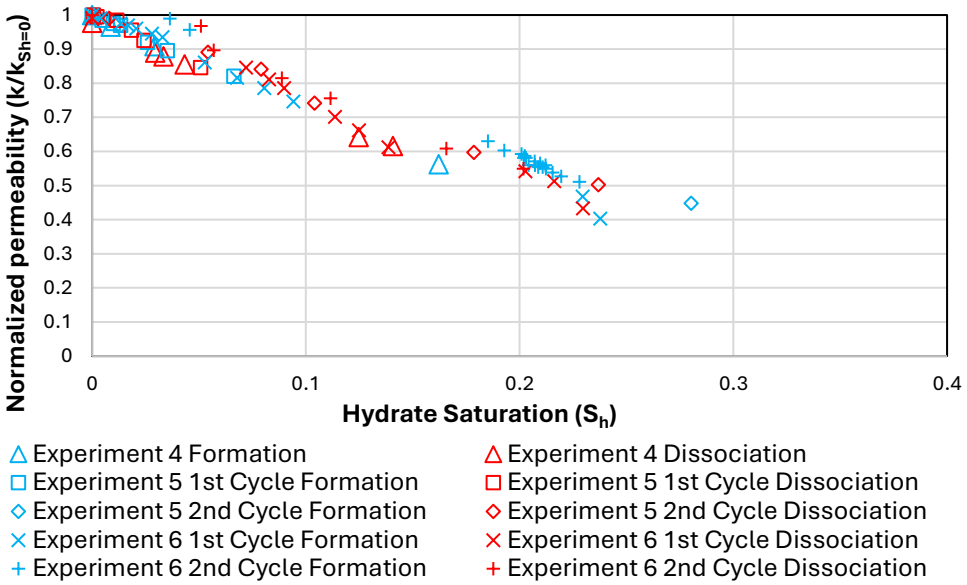

Figure 54: Original data of the Normalized permeability (k/k_0) vs Hydrate saturation (S_h).

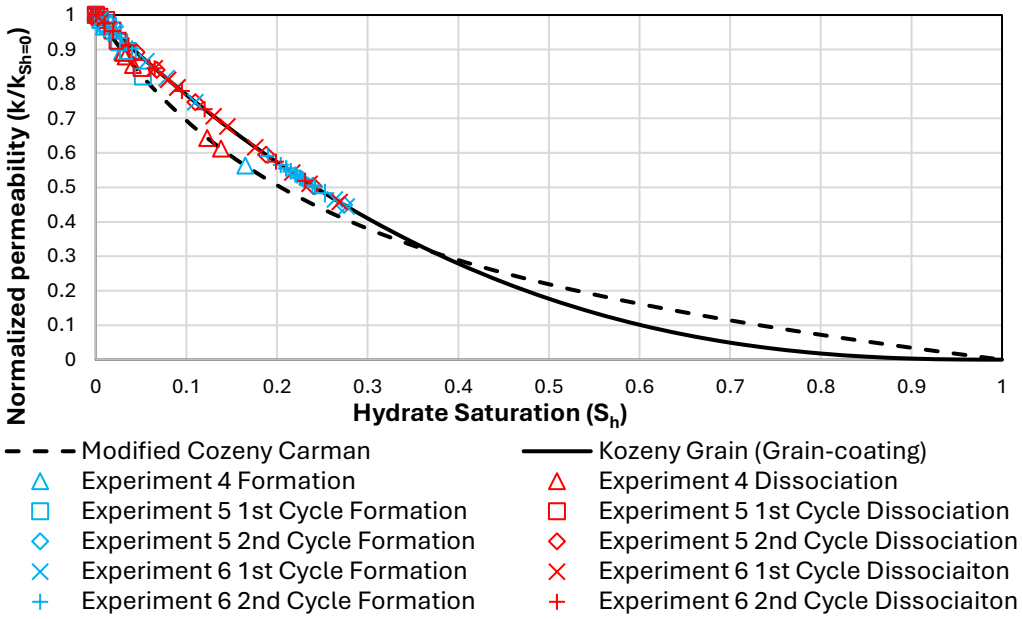

Figure 55: Original data of the Normalized permeability (k/k_0) vs the Corrected Hydrate saturation (S_h).

4.3.5 Kinetic Analysis of Hydrate Formation and Dissociation

To assess the applicability of the kinetic models discussed in the literature review chapter to the current experimental data, plots were generated linking the hydrate growth and dissociation rates to relevant parameters.

In Figure 56 the induction time versus the fugacity ration is presented in order to assess the kinetic sensitivity of hydrate nucleation. Higher fugacity ratios indicate stronger supersaturation,

promoting faster nucleation. A power-law function fits the data very well showing how induction time sharply increases when the fugacity ratio becomes really small. In Figure 57 the logarithmic scale is applied in both axes in order to find the linear relationship between these two parameters and be able to estimate them.

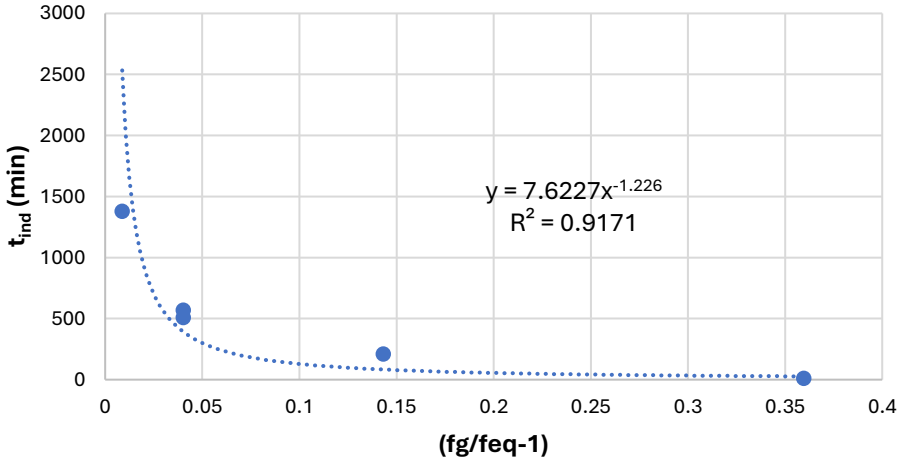

Figure 56: Induction time of conducted experiments versus fugacity ratio.

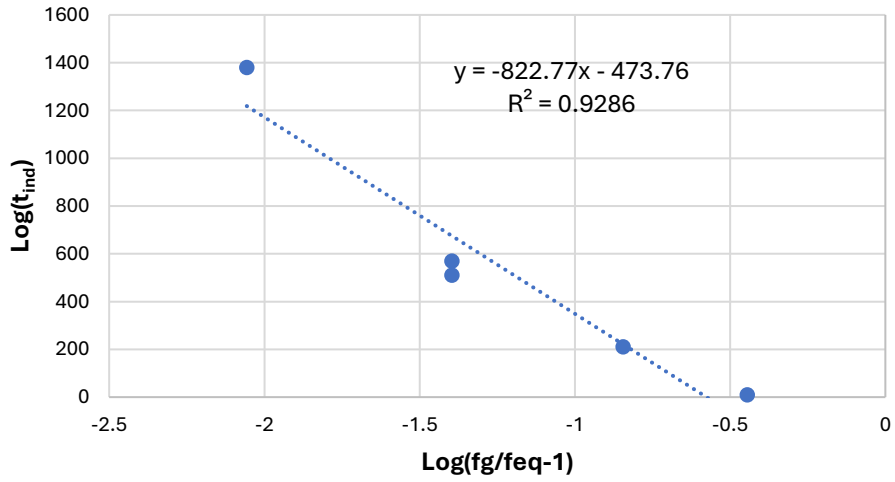

Figure 57: Determination of the parameters m and k.

In a similar way in Figure 58 the induction time over the degrees of subcooling of every experiment is presented in order to further examine the factors influencing hydrate nucleation. Subcooling represents the thermal driving force for hydrate formation, where higher temperature difference typically enhances nucleation potential. The analysis showed a decreasing induction time with increasing subcooling, indicating that higher subcooling leads to quicker onset of hydrate formation. In Figure 59, again the linear relationship between induction time and subcooling is represented.

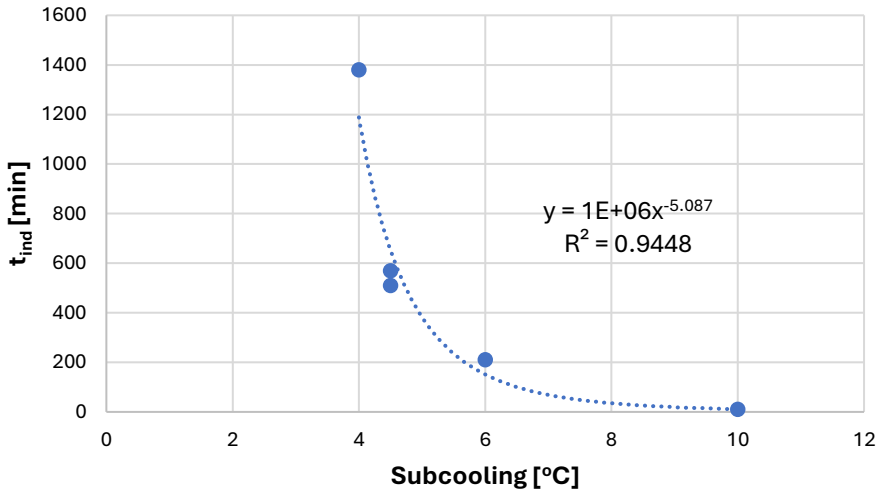

Figure 58: Induction time versus subcooling for the conducted experiments.

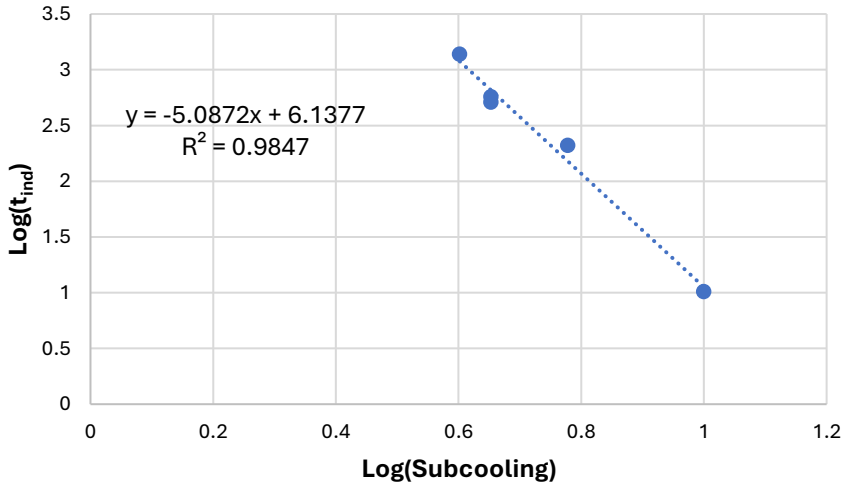

Figure 59: Determination of the parameters m and with subcooling as the driving force.

When compared to the induction time versus the fugacity ratio plot, both subcooling and fugacity ratio demonstrate an inverse relationship with induction time, suggesting that both thermal and pressure-dependent driving forces contribute significantly to the kinetics of nucleation. Regarding hydrate growth kinetics of CO_2 hydrates the hydrate saturation rate increase was plotted against the fugacity difference, which represents the driving force for hydrate formation, following the proportional relationship which was shown in the literature review chapter. In Figure 60 the trendlines of all included experimental cycles followed a power-law function and given the fact that in all these cycles the hydrate forming temperature is the same (2.5 °C) a master curve can be fitted in order to obtain a general equation regarding the growth kinetics of CO_2 hydrates. Experiment 4 data points are again excluded from the master curve determination.

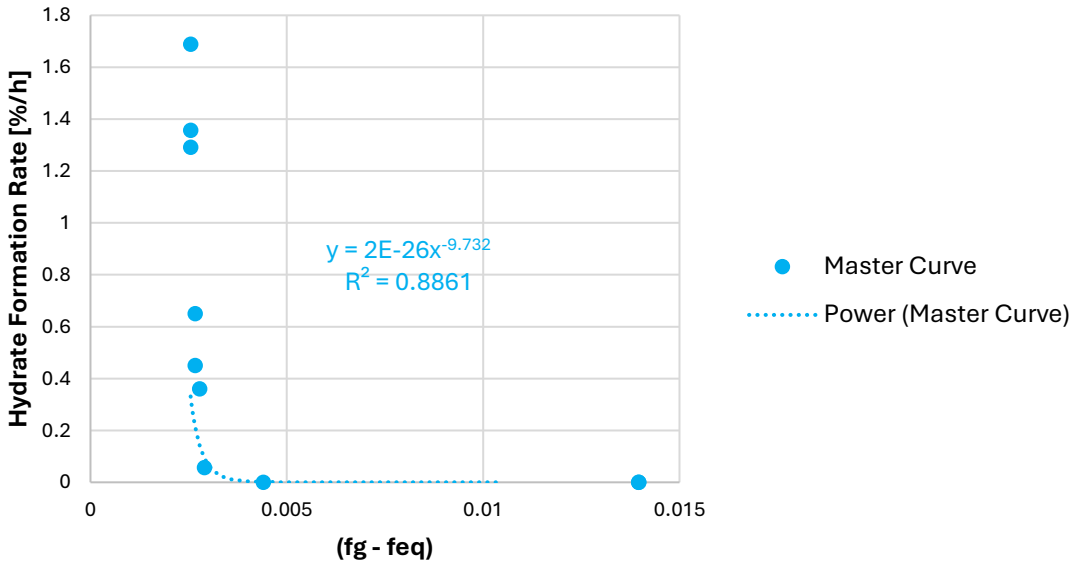

Figure 60: Hydrate formation rate (hydrate saturation difference over time) versus the fugacity difference for all experimental cycles combined.

As the kinetic equation regarding the dissociation of CO_2 hydrates is the same as the growth one, again the rate of hydrate dissociation (hydrate saturation difference over time) is plotted against the fugacity difference. All experimental data followed the power-law function and similarly to the growth kinetics, a master curve is fitted in an attempt to try and generate an equation that would describe the dissociation kinetics of the conducted experiments (see Figure 61). It has to noted that Experiment 4 was excluded from the construction of the master curve both in the growth data and the dissociation data because of its peculiar core.

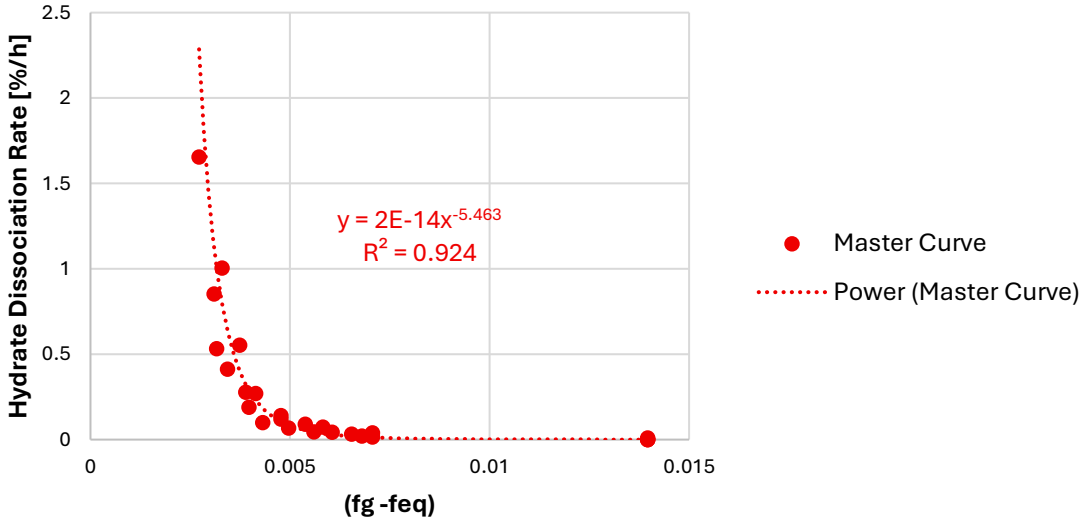

Figure 61: Hydrate dissociation rate (hydrate saturation difference over time) versus the fugacity difference for all experimental cycles combined.

Furthermore, in Figure 62 the logarithmic scale of the dissociation rate against the inverse of temperature is plotted in order to examine if the relationship between the two data is linear and thus investigate if the experimental data follow an Arrhenius type equation. From Figure 62 is seen that indeed the data follow the linear relationship, but Experiment 4 indicated a not so good fit, and the trends slop differed significantly in comparison with the rest three experimental cycles.

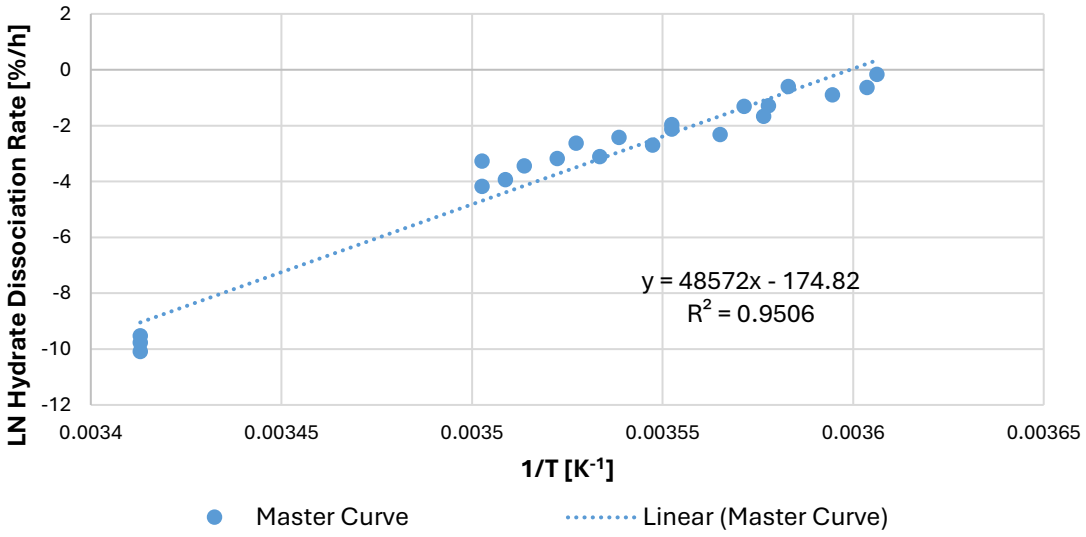

Figure 62: Hydrate dissociation rate (hydrate saturation difference over time) in logarithmic scale versus the inverse of temperature.

Conclusively, despite the fact that the surface area (Ap) was not explicitly measure during the experiments, the kinetic analyses assumed it to be incorporated into the overall rate constant (k). This simplification was followed due to difficulties in accurate estimation of the surface area. Nonetheless, when examining the experimental trends regarding the dependency of induction time on fugacity ratio and subcooling, as well as the hydrate formation and dissociation rates with the fugacity difference, with the kinetic equations mentioned in the literature, an empirical simplified kinetic expression in which the surface area is incorporated into the effective hydrate saturation over time ($\Delta S_h/\Delta t$) can reasonably describe the experimental results:

$$\frac{\Delta S_h}{\Delta t} = k \cdot \left(f_{exp} - f_{eq}\right)$$

where k represents an empirical parameter capturing both the intrinsic kinetics and the effective surface area of hydrate phase, and the fugacity difference between the experimental and the equilibrium conditions is the driving force. This equation provides good agreement with the observed hydrate growth and dissociation trends across the experiments indicating its usefulness in characterizing hydrate kinetics under the tested conditions. Furthermore, the temperature dependance of the dissociation rate indicated a linear trend when plotted in logarithmic form against inverse temperature, and it is consistent with an Arrhenius type relationship:

$$ln\left(\frac{\Delta S_h}{\Delta t}\right) = -\frac{E_a}{R} \cdot \frac{1}{T} + ln(A)$$

Suggesting that the dissociation kinetics follow a thermally activated process, in agreement with commonly cited hydrate dissociation models in the literature. The proposed model captures the key dependencies of hydrate formation and dissociation kinetics under the studied conditions.

Chapter 5: Conclusions and Recommendations for Future Work

In this section the key findings of the previous discussion are presented regarding the effect of subcooling and cooling/heating methods on the kinetics of CO_2 hydrate during formation and dissociation inside the core samples.

5.1 Conclusions

- Since subcooling is one of the main a driving forces for hydrate formation. The higher the degree of subcooling is the smaller the induction time.
- The faster the hydrate forming temperature is reached (rate of cooling), the smaller the induction time was. For instance, in the isothermal method that utilized a really fast rate of cooling (2 ^{o}C/h) the onset of hydrate formation appeared significantly sooner in comparison with the ramp cooling method, which utilized a smaller rate to reach the hydrate forming temperature (0.1 ^{o}C/h).
- In all experimental cycles, the onset of hydrate dissociation consistently occurred at a distinct temperature threshold a few degrees below the equilibrium line temperature of the hydrate stability zone. This behavior is attributed to the porous medium that was used (Bentheimer sandstone), which appears to inhibit hydrate formation and promote hydrate dissociation.
- Higher degrees of subcooling led to higher hydrate saturation and simultaneous larger permeability decrease.
- Higher heating rates caused faster hydrate dissociation and permeability recovery.
- Hydrates formed under a relatively slow and controlled constant cooling rate appeared more stable as the hydrate formation is a crystallization process and gas had sufficient time to be entrapped inside the hydrate cavities. Increasing the gas encapsulation can increase the stability of hydrate structure.
- Hydrates that were formed under a constant rate of cooling either fast or slow appeared to follow the Kozeny Grain (Grain-Coating) permeability model, whereas hydrates that formed under a non-constant cooling method appeared to follow a different permeability model, namely the Modified Kozeny Carman.

5.2 Recommendations

- Improve repeatability and validation: In order to enhance the reliability of results, it is recommended for experiments to be repeated under identical conditions to confirm findings and improve statistical confidence.
- Explore a wider range of sub cooling degrees: Additional experiments at different degrees of subcooling (either higher or lower) could provide more detailed insights into its effect as a driving force in hydrate kinetics in both formation and dissociation.

- Test alternative cooling and heating profiles: Vary cooling/heating rates during ramp methods to examine their effect in both formation and dissociation. Also, experiment with various temperature intervals during both cooling and heating processes.
- Coupled method experiments: Combining different cooling and heating strategies (e.g. step cooling with ramp heating, or ramp cooling with step heating) could provide a wider understanding of how thermal stimulation influences hydrate behavior.
- Saturation control and distribution: Achieving a target water saturation was challenging, and sometimes resulted in uneven brine distribution along the core sample. Improved core preparation is recommended to ensure more uniform saturation profiles.
- Advanced imaging techniques: For more precise calculation of hydrate saturation and water to hydrate conversion, utilizing micro CT-scanner or NMR can be very beneficial since the distinction of water and hydrate phases is possible.
- Investigation of different core samples: Exploring porous media with different mineral compositions and petrophysical characteristics to examine whether the kinetics of hydrates during formation and dissociation differ.
- Utilizing coding or software: To model the conducted experiments and apply history matching in constructing a model capable of simulating CO_2 hydrate behavior inside porous media.

References

Aghajanloo, M., Reza Ehsani, M., Taheri, Z., Jafari Behbahani, T., Mohammadi, A. H., & Mohammad Taheri, M. (2022). Kinetics of methane + hydrogen sulfide clathrate hydrate formation in the presence/absence of poly N-vinyl pyrrolidone (PVP) and L-tyrosine: Experimental study and modeling of the induction time. *Chemical Engineering Science*, *250*, 117384. https://doi.org/10.1016/j.ces.2021.117384

Aghajanloo, M., Yan, L., Berg, S., Voskov, D., & Farajzadeh, R. (2024). Impact of CO2 hydrates on injectivity during CO2 storage in depleted gas fields: A literature review. *Gas Science and Engineering*, *123*, 205250. https://doi.org/10.1016/j.jgsce.2024.205250

Anderson, G. K. (2003). Enthalpy of dissociation and hydration number of carbon dioxide hydrate from the Clapeyron equation. *The Journal of Chemical Thermodynamics*, *35*(7), 1171–1183. https://doi.org/10.1016/S0021-9614(03)00093-4

Askarova, A., Mukhametdinova, A., Markovic, S., Khayrullina, G., Afanasev, P., Popov, E., & Mukhina, E. (2023). An Overview of Geological CO2 Sequestration in Oil and Gas Reservoirs. *Energies*, *16*(6), Article 6. https://doi.org/10.3390/en16062821

Bachu, S., & Shaw, J. (2003). Evaluation of the CO2 Sequestration Capacity in Alberta's Oil and Gas Reservoirs at Depletion and the Effect of Underlying Aquifers. *Journal of Canadian Petroleum Technology*, *42*(09). https://doi.org/10.2118/03-09-02

Bai, D., Chen, G., Zhang, X., Sum, A. K., & Wang, W. (2015). How Properties of Solid Surfaces Modulate the Nucleation of Gas Hydrate. *Scientific Reports*, *5*(1), 12747. https://doi.org/10.1038/srep12747

Bashir, A., Ali, M., Patil, S., Aljawad, M. S., Mahmoud, M., Al-Shehri, D., Hoteit, H., & Kamal, M. S. (2024). Comprehensive review of CO2 geological storage: Exploring principles, mechanisms, and prospects. *Earth-Science Reviews*, *249*, 104672. https://doi.org/10.1016/j.earscirev.2023.104672

Benmesbah, F. D., Clain, P., Fandino, O., Osswald, V., Fournaison, L., Dicharry, C., Ruffine, L., & Delahaye, A. (2022). Calorimetric study of carbon dioxide (CO2) hydrate formation and dissociation processes in porous media. *Chemical Engineering Science*, *264*, 118108. https://doi.org/10.1016/j.ces.2022.118108

Boreham, C., Underschultz, J., Stalker, L., Kirste, D., Freifeld, B., Jenkins, C., & Ennis-King, J. (2011). Monitoring of CO2 storage in a depleted natural gas reservoir: Gas geochemistry from the CO2CRC Otway Project, Australia. *International Journal of Greenhouse Gas Control*, *5*(4), 1039–1054. https://doi.org/10.1016/j.ijggc.2011.03.011

Bui, M., S. Adjiman, C., Bardow, A., J. Anthony, E., Boston, A., Brown, S., S. Fennell, P., Fuss, S., Galindo, A., A. Hackett, L., P. Hallett, J., J. Herzog, H., Jackson, G., Kemper, J., Krevor, S., C. Maitland, G., Matuszewski, M., S. Metcalfe, I., Petit, C., … Dowell, N. M. (2018). Carbon capture and storage (CCS): The way forward. *Energy & Environmental Science*, *11*(5), 1062–1176. https://doi.org/10.1039/C7EE02342A

Cao, X., Yang, K., Xia, W., Tang, G., & Bian, J. (2021). Dissociation experiment and dissociation rate model of CO2 hydrate. *Natural Gas Industry B*, *8*(6), 607–614. https://doi.org/10.1016/j.ngib.2021.11.008

Carroll, J. J., Slupsky, J. D., & Mather, A. E. (1991). The Solubility of Carbon Dioxide in Water at Low Pressure. *Journal of Physical and Chemical Reference Data*, *20*(6), 1201–1209. https://doi.org/10.1063/1.555900

References

Chesnokov, C., Farajzadeh, R., Prempeh, K. O. K., Kahrobaei, S., Snippe, J., & Bedrikovetsky, P. (2024). Joule-Thomson cooling of CO2 injected into aquifer under heat exchange with adjacent formations by Newtons law- 1D exact solution. *Advances in Water Resources*, *190*, 104758. https://doi.org/10.1016/j.advwatres.2024.104758

Clennell, M. B., Hovland, M., Booth, J. S., Henry, P., & Winters, W. J. (1999). Formation of natural gas hydrates in marine sediments: 1. Conceptual model of gas hydrate growth conditioned by host sediment properties. *Journal of Geophysical Research: Solid Earth*, *104*(B10), 22985–23003. https://doi.org/10.1029/1999JB900175

de Kok, J. (2024, June 26). *Monitoring Injectivity for CO2 Injection in Depleted Gas Reservoirs*. SPE Europe Energy Conference and Exhibition. https://doi.org/10.2118/220119-MS

Dhamu, V., Qureshi, M. F., Barckholtz, T. A., Mhadeshwar, A. B., & Linga, P. (2023). Evaluating liquid CO2 hydrate formation kinetics, morphology, and stability in oceanic sediments on a lab scale using top injection. *Chemical Engineering Journal*, *478*, 147200. https://doi.org/10.1016/j.cej.2023.147200

Dodds, W. S., Stutzman, L. F., & Sollami, B. J. (1956). Carbon Dioxide Solubility in Water. *Industrial & Engineering Chemistry Chemical & Engineering Data Series*, *1*(1), 92–95. https://doi.org/10.1021/i460001a018

Feyzi, V., & Mohebbi, V. (2020). Experimental study and modeling of the kinetics of carbon-dioxide hydrate formation and dissociation: A mass transfer limited kinetic approach. *Journal of Natural Gas Science and Engineering*, *77*, 103273. https://doi.org/10.1016/j.jngse.2020.103273

Gambelli, A. M., & Rossi, F. (2022). Experimental characterization of the difference in induction period between CH4 and CO2 hydrates: Motivations and possible consequences on the replacement process. *Journal of Natural Gas Science and Engineering*, *108*, 104848. https://doi.org/10.1016/j.jngse.2022.104848

Gauteplass, J., Almenningen, S., Ersland, G., Barth, T., Yang, J., & Chapoy, A. (2020). Multiscale investigation of CO2 hydrate self-sealing potential for carbon geo-sequestration. *Chemical Engineering Journal*, *381*, 122646. https://doi.org/10.1016/j.cej.2019.122646

Geng, L., Cai, J., Lu, C., Qin, X., Qi, R., Meng, F., Xie, Y., Sha, Z., Wang, X., & Sun, C. (2021). Phase Equilibria of Natural Gas Hydrates in Bulk Brine and Marine Sediments from the South China Sea. *Journal of Chemical & Engineering Data*, *66*(11), 4064–4074. https://doi.org/10.1021/acs.jced.1c00307

Goldman, L. W. (2007). Principles of CT and CT Technology. *Journal of Nuclear Medicine Technology*, *35*(3), 115–128. https://doi.org/10.2967/jnmt.107.042978

Heidarabad, R. G., & Shin, K. (2024). Carbon Capture and Storage in Depleted Oil and Gas Reservoirs: The Viewpoint of Wellbore Injectivity. *Energies*, *17*(5), Article 5. https://doi.org/10.3390/en17051201

Hosseini Zadeh, A., Kim, I., & Kim, S. (2023). Characteristics of CO2 hydrate formation and dissociation at different CO2-water ratios in a porous medium. *International Journal of Greenhouse Gas Control*, *125*, 103883. https://doi.org/10.1016/j.ijggc.2023.103883

Hoteit, H., Fahs, M., & Soltanian, M. R. (2019). Assessment of CO2 Injectivity During Sequestration in Depleted Gas Reservoirs. *Geosciences*, *9*(5), Article 5. https://doi.org/10.3390/geosciences9050199

Hu, Q., & Xiao, X. (2023). Formation methods and applications of carbon dioxide hydrate: An overview. *Carbon Capture Science & Technology*, *7*, 100113. https://doi.org/10.1016/j.ccst.2023.100113

Indina, V., Fernandes, B. R. B., Delshad, M., Farajzadeh, R., & Sepehrnoori, K. (2024). On the Significance of Hydrate Formation/Dissociation during CO2 Injection in Depleted Gas Reservoirs. *SPE Journal*, *29*(12), 7194–7213. https://doi.org/10.2118/218550-PA

Iwai, H., Konishi, Y., Saimyou, K., Kimoto, S., & Oka, F. (2018). Rate effect on the stress-strain relations of synthetic carbon dioxide hydrate-bearing sand and dissociation tests by thermal stimulation. *Soils and Foundations*, *58*(5), 1113–1132. https://doi.org/10.1016/j.sandf.2018.05.007

Jadhawar, P. S., Mohammadi, A. H., Yang, J., & Tohidi Kalorazi, B. (2006). Subsurface carbon dioxide storage through clathrate hydrate formation. In *In: Lombardi, S., et al., eds., Advances in the geological storage of carbon dioxide :international approaches to reduce anthropogenic greenhouse gas emissions. Dordrecht: Springer* (pp. 111–126).

Jr, E. D. S., Koh, C. A., & Koh, C. A. (2007). *Clathrate Hydrates of Natural Gases* (3rd ed.). CRC Press. https://doi.org/10.1201/9781420008494

Kang, S.-P., Lee, J.-W., & Ryu, H.-J. (2008). Phase behavior of methane and carbon dioxide hydrates in meso- and macro-sized porous media. *Fluid Phase Equilibria*, *274*(1), 68–72. https://doi.org/10.1016/j.fluid.2008.09.003

Ke, W., Svartaas, T. M., & Chen, D. (2019). A review of gas hydrate nucleation theories and growth models. *Journal of Natural Gas Science and Engineering*, *61*, 169–196. https://doi.org/10.1016/j.jngse.2018.10.021

Kocs, E. A. (2017). The global carbon nation: Status of CO2 capture, storage and utilization. *EPJ Web of Conferences*, *148*, 00002. https://doi.org/10.1051/epjconf/201714800002

Komai, T., Kawamura, Y. K. T., & Yoon, J.-H. (2003, May 25). *Extraction of Gas Hydrates Using CO2 Sequestration*. The Thirteenth International Offshore and Polar Engineering Conference. https://dx.doi.org/

Kou, X., Li, X.-S., Wang, Y., Liu, J.-W., & Chen, Z.-Y. (2021). Effects of gas occurrence pattern on distribution and morphology characteristics of gas hydrates in porous media. *Energy*, *226*, 120401. https://doi.org/10.1016/j.energy.2021.120401

Kumar, A., Sakpal, T., Linga, P., & Kumar, R. (2015). Enhanced carbon dioxide hydrate formation kinetics in a fixed bed reactor filled with metallic packing. *Chemical Engineering Science*, *122*, 78–85. https://doi.org/10.1016/j.ces.2014.09.019

Lage, J. L. (1998). THE FUNDAMENTAL THEORY OF FLOW THROUGH PERMEABLE MEDIA FROM DARCY TO TURBULENCE†. In D. B. Ingham & I. Pop (Eds.), *Transport Phenomena in Porous Media* (pp. 1–30). Pergamon. https://doi.org/10.1016/B978-008042843-7/50001-5

Li, D., Graupner, B. J., & Bauer, S. (2011). A method for calculating the liquid density for the CO2–H2O–NaCl system under CO2 storage condition. *Energy Procedia*, *4*, 3817–3824. https://doi.org/10.1016/j.egypro.2011.02.317

Li, Z., Gan, B., Li, Z., Zhang, H., Wang, D., Zhang, Y., & Wang, Y. (2023). Kinetic mechanisms of methane hydrate replacement and carbon dioxide hydrate reorganization. *Chemical Engineering Journal*, *477*, 146973. https://doi.org/10.1016/j.cej.2023.146973

Liu, F.-P., Li, A.-R., Qing, S.-L., Luo, Z.-D., & Ma, Y.-L. (2022). Formation kinetics, mechanism of CO2 hydrate and its applications. *Renewable and Sustainable Energy Reviews*, *159*, 112221. https://doi.org/10.1016/j.rser.2022.112221

Mali, G. A., Chapoy, A., & Tohidi, B. (2018). Investigation into the effect of subcooling on the kinetics of hydrate formation. *The Journal of Chemical Thermodynamics*, *117*, 91–96. https://doi.org/10.1016/j.jct.2017.08.014

Mekala, P., Busch, M., Mech, D., Patel, R. S., & Sangwai, J. S. (2014). Effect of silica sand size on the formation kinetics of CO2 hydrate in porous media in the presence of pure water and

seawater relevant for CO2 sequestration. *Journal of Petroleum Science and Engineering*, *122*, 1–9. https://doi.org/10.1016/j.petrol.2014.08.017

Mu, L., & Cui, Q. (2019). Experimental Study on the Dissociation Equilibrium of (CH4 + CO2 + N2) Hydrates in the Mixed Sediments. *Journal of Chemical & Engineering Data*, *64*(12), 5806–5813. https://doi.org/10.1021/acs.jced.9b00760

Nair, V. C., Ramesh, S., Ramadass, G. A., & Sangwai, J. S. (2016). Influence of thermal stimulation on the methane hydrate dissociation in porous media under confined reservoir. *Journal of Petroleum Science and Engineering*, *147*, 547–559. https://doi.org/10.1016/j.petrol.2016.09.017

Natarajan, V., Bishnoi, P. R., & Kalogerakis, N. (1994). Induction phenomena in gas hydrate nucleation. *Chemical Engineering Science*, *49*(13), 2075–2087. https://doi.org/10.1016/0009-2509(94)E0026-M

Oya, S., Aifaa, M., & Ohmura, R. (2017). Formation, growth and sintering of CO2 hydrate crystals in liquid water with continuous CO2 supply: Implication for subsurface CO2 sequestration. *International Journal of Greenhouse Gas Control*, *63*, 386–391. https://doi.org/10.1016/j.ijggc.2017.06.007

Palodkar, A. V., Mandal, S., & Jana, A. K. (2016). Modeling Growth Kinetics of Gas Hydrate in Porous Media: Experimental Validation. *Energy & Fuels*, *30*(9), 7656–7665. https://doi.org/10.1021/acs.energyfuels.6b01397

Peksa, A. E., Wolf, K.-H. A. A., & Zitha, P. L. J. (2015). Bentheimer sandstone revisited for experimental purposes. *Marine and Petroleum Geology*, *67*, 701–719. https://doi.org/10.1016/j.marpetgeo.2015.06.001

Perez-Perez, A., Mujica, M., Pujol, G., Jellema, R., & Agenet, N. (2023). *Hydrate risk assessment during CO2 injection on legacy wells in a highly depleted gas field*. *2023*(1), 1–5. https://doi.org/10.3997/2214-4609.202310955

Peysson, Y., André, L., & Azaroual, M. (2014). Well injectivity during CO2 storage operations in deep saline aquifers—Part 1: Experimental investigation of drying effects, salt precipitation and capillary forces. *International Journal of Greenhouse Gas Control*, *22*, 291–300. https://doi.org/10.1016/j.ijggc.2013.10.031

Prasad, P. S. R., & Kiran, B. S. (2020). Guest molecular exchange and stability of carbon dioxide hydrates under the influence of methane gas. *Journal of Natural Gas Science and Engineering*, *84*, 103689. https://doi.org/10.1016/j.jngse.2020.103689

Raza, A., Gholami, R., Rezaee, R., Bing, C. H., Nagarajan, R., & Hamid, M. A. (2017). Preliminary assessment of CO2 injectivity in carbonate storage sites. *Petroleum*, *3*(1), 144–154. https://doi.org/10.1016/j.petlm.2016.11.008

Raza, A., Gholami, R., Rezaee, R., Rasouli, V., & Rabiei, M. (2019). Significant aspects of carbon capture and storage – A review. *Petroleum*, *5*(4), 335–340. https://doi.org/10.1016/j.petlm.2018.12.007

Raza, A., Rezaee, R., Gholami, R., Bing, C. H., Nagarajan, R., & Hamid, M. A. (2016). A screening criterion for selection of suitable CO2 storage sites. *Journal of Natural Gas Science and Engineering*, *28*, 317–327. https://doi.org/10.1016/j.jngse.2015.11.053

Rehman, A. N., Bavoh, C. B., Pendyala, R., Kassim, Z., Sabil, K. M., Bt Othman, N. A., & Lal, B. (2022). Kinetic insight on CO2 hydrate formation and dissociation in quartz sand in presence of brine. *International Journal of Greenhouse Gas Control*, *114*, 103582. https://doi.org/10.1016/j.ijggc.2022.103582

Rossi, F., Li, Y., & Gambelli, A. M. (2021). Thermodynamic and Kinetic Description of the Main Effects Related to the Memory Effect during Carbon Dioxide Hydrates Formation in a

Confined Environment. *Sustainability*, *13*(24), Article 24. https://doi.org/10.3390/su132413797

S, M. (2024). Carbonate and Sandstone Reservoirs in CO2 Sequestration: Assessing Porosity and Permeability for Enhanced Storage Potential. *Petroleum & Petrochemical Engineering Journal*, *8*(4), 1–12. https://doi.org/10.23880/ppej-16000398

Saeedi, A., & Rezaee, R. (2012). Effect of residual natural gas saturation on multiphase flow behaviour during CO2 geo-sequestration in depleted natural gas reservoirs. *Journal of Petroleum Science and Engineering*, *82–83*, 17–26. https://doi.org/10.1016/j.petrol.2011.12.012

Sahu, C., Sircar, A., Sangwai, J. S., & Kumar, R. (2022). Effect of Methylamine, Amylamine, and Decylamine on the Formation and Dissociation Kinetics of CO2 Hydrate Relevant for Carbon Dioxide Sequestration. *Industrial & Engineering Chemistry Research*, *61*(7), 2672–2684. https://doi.org/10.1021/acs.iecr.1c04074

Sander, R., Pan, Z., & Connell, L. D. (2017). Laboratory measurement of low permeability unconventional gas reservoir rocks: A review of experimental methods. *Journal of Natural Gas Science and Engineering*, *37*, 248–279. https://doi.org/10.1016/j.jngse.2016.11.041

Sloan, E. D. (2003). Fundamental principles and applications of natural gas hydrates. *Nature*, *426*(6964), 353–359. https://doi.org/10.1038/nature02135

Sloan Jr, E. D., & Fleyfel, F. (1991). A molecular mechanism for gas hydrate nucleation from ice. *AIChE Journal*, *37*(9), 1281–1292. https://doi.org/10.1002/aic.690370902

Smith, D. H., Wilder, J. W., & Seshadri, K. (2002). Methane hydrate equilibria in silica gels with broad pore-size distributions. *AIChE Journal*, *48*(2), 393–400. https://doi.org/10.1002/aic.690480222

Sun, Q., & Kang, Y. T. (2016). Review on CO2 hydrate formation/dissociation and its cold energy application. *Renewable and Sustainable Energy Reviews*, *62*, 478–494. https://doi.org/10.1016/j.rser.2016.04.062

Sun, S., Li, Y., Gu, L., Yang, Z., & Zhao, J. (2022). Experimental study on carbon dioxide hydrate formation in the presence of static magnetic field. *The Journal of Chemical Thermodynamics*, *170*, 106764. https://doi.org/10.1016/j.jct.2022.106764

Talaghat, M. R., & Khodaverdilo, A. R. (2019). Study of different models of prediction of the simple gas hydrates formation induction time and effect of different equations of state on them. *Heat and Mass Transfer*, *55*(5), 1245–1255. https://doi.org/10.1007/s00231-018-2508-y

Tariq, M., Soromenho, M. R. C., Rebelo, L. P. N., & Esperança, J. M. S. S. (2022). Insights into CO2 hydrates formation and dissociation at isochoric conditions using a rocking cell apparatus. *Chemical Engineering Science*, *249*, 117319. https://doi.org/10.1016/j.ces.2021.117319

Uchida, T. (1998). Physical property measurements on CO2 clathrate hydrates. Review of crystallography, hydration number, and mechanical properties. *Waste Management*, *17*(5), 343–352. https://doi.org/10.1016/S0956-053X(97)10047-2

Uchida, T., Ebinuma, T., Takeya, S., Nagao, J., & Narita, H. (2002). Effects of Pore Sizes on Dissociation Temperatures and Pressures of Methane, Carbon Dioxide, and Propane Hydrates in Porous Media. *The Journal of Physical Chemistry B*, *106*(4), 820–826. https://doi.org/10.1021/jp012823w

Vishal, V., & Singh, T. N. (Eds.). (2016). *Geologic Carbon Sequestration*. Springer International Publishing. https://doi.org/10.1007/978-3-319-27019-7

References

Wang, P., Zhou, H., Yang, M., Jiang, L., & Li, Y. (2019). *Review of Co2 Storage as Hydrate in Depleted Reservoirs* (SSRN Scholarly Paper No. 3365640). Social Science Research Network. https://doi.org/10.2139/ssrn.3365640

Wang, X.-H., Xu, X.-J., Cai, J., Wu, Y.-W., Chen, Y.-X., Pang, W.-X., Sun, C.-Y., & Chen, G.-J. (2023). Experimental study on the intrinsic dissociation rate of methane hydrate. *Chemical Engineering Science*, *282*, 119278. https://doi.org/10.1016/j.ces.2023.119278

Wen, Z., Yao, Y., Luo, W., & Lei, X. (2021). Memory effect of CO2-hydrate formation in porous media. *Fuel*, *299*, 120922. https://doi.org/10.1016/j.fuel.2021.120922

Wu, G., Tian, L., Ha, L., Feng, F., Yang, Z., Feng, J.-C., Coulon, F., Jiang, Y., & Zhang, R. (2022). Influence of pipeline steel surface on the thermal stability of methane hydrate. *Journal of Molecular Liquids*, *367*, 120486. https://doi.org/10.1016/j.molliq.2022.120486

Yang, M., Song, Y., Liu, W., Zhao, J., Ruan, X., Jiang, L., & Li, Q. (2013). Effects of additive mixtures (THF/SDS) on carbon dioxide hydrate formation and dissociation in porous media. *Chemical Engineering Science*, *90*, 69–76. https://doi.org/10.1016/j.ces.2012.11.026

Yang, M., Song, Y., Liu, Y., Chen, Y., & Li, Q. (2010). Influence of Pore Size, Salinity and Gas Composition upon the Hydrate Formation Conditions. *Chinese Journal of Chemical Engineering*, *18*(2), 292–296. https://doi.org/10.1016/S1004-9541(08)60355-9

Yin, Z., Khurana, M., Tan, H. K., & Linga, P. (2018). A review of gas hydrate growth kinetic models. *Chemical Engineering Journal*, *342*, 9–29. https://doi.org/10.1016/j.cej.2018.01.120

Zatsepina, O. Y., & Buffett, B. A. (2002). Nucleation of CO2-hydrate in a porous medium. *Fluid Phase Equilibria*, *200*(2), 263–275. https://doi.org/10.1016/S0378-3812(02)00032-8

Zhao, Y., Lei, X., Zheng, J., Li, M., Johns, M. L., Huang, M., & Song, Y. (2021). High resolution MRI studies of CO2 hydrate formation and dissociation near the gas-water interface. *Chemical Engineering Journal*, *425*, 131426. https://doi.org/10.1016/j.cej.2021.131426

Zhao, Y., & Zhang, Z. (2024). Molecular Insights into the Influence of Major Marine Ions on Carbon Dioxide Hydrate Growth. *Crystal Growth & Design*, *24*(3), 1380–1388. https://doi.org/10.1021/acs.cgd.3c01354

Zheng, J., Chong, Z. R., Qureshi, M. F., & Linga, P. (2020). Carbon Dioxide Sequestration via Gas Hydrates: A Potential Pathway toward Decarbonization. *Energy & Fuels*, *34*(9), 10529–10546. https://doi.org/10.1021/acs.energyfuels.0c02309